UNIVERSITÀ DEGLI STUDI DI SASSARI

SCUOLA DI DOTTORATO DI RICERCA
Scienze e Biotecnologie
dei Sistemi Agrari e Forestali
e delle Produzioni Alimentari

Agrometeorologia ed ecofisiologia dei sistemi agrari e forestali

Ciclo XXV

A modelling approach to estimate carbon dioxide exchange at regional scale

Dr. Marcello Casula

Direttore della	Prof. Alba Pusino
Scuola	
Referente di	Prof. Donatella Spano
Indirizzo	
Docenti Guida	Prof. Donatella Spano
	Dr. Serena Marras

Anno accademico 2011- 2012

INDEX

Abstract

At the moment, it is hard to find studies dealing with carbon flux estimates at regional scale in Mediterranean climate areas. In this study, it is presented a modeling framework to obtain 3 Km resolution carbon exchange maps for the Mediterranean island of Sardinia.

The multilayer SVAT model Advanced-Canopy-Atmosphere-Soil-Algorithm (ACASA) was coupled "on-line" to the mesoscale meteorological model Weather-Research-and-Forecasting (WRF). The WRF-ACASA model was initialized with the ERA-Interim meteorological reanalysis data at a resolution of 0.7° (77 Km), while the European Environment Agency Corine land use map was exploited to acquire the land use data.

Results were validated in for vineyard ecosystems using Eddy Covariance (EC) observations. A linear regression of model versus observed data with an $R^2 = 0.91$ indicates that the model was able to explain more than 90% of the total observed variation in carbon dioxide flux. A further analysis was performed comparing model results with other studies involving the three most diffused vegetation categories of the island covering about 60% of the island: *Mediterranean forest*, *Mediterranean maquis,* and C*ropland and pastures*. This analysis confirmed the robustness of the modeling framework for the above land use type. The methodology tested in this work proved as the WRF-ACASA model represents a flexible instrument to provide a cogent simulation of the spatial and temporal evolution variability of CO_2 flux at regional scale.

1 Introduction

The electromagnetic energy from the Sun is what permits life on the Earth. In the history of our planet, solar radiation has not always been constant, allowing for different climates. Climate diversity is due both to the different amounts of solar radiation reaching the planet and to the different composition of the atmosphere, which plays an important role in the mechanisms of re-radiation of the energy reaching the surface. While the atmosphere is almost transparent to radiation in the solar spectrum, it absorbs the main part of the energy radiated in the Earth's surface emission spectrum. Therefore, much of the energy emitted by the Earth is absorbed and re-radiated by the atmosphere itself, both toward space and back to the surface. With respect to the case of total transparency of the atmosphere to the Earth's surface emission, a higher temperature of the surface-atmosphere system is required in order to disperse the same amount of energy that our planet receives. The phenomenon, described with more details in the next section, is known as the greenhouse effect and is due mainly to six gases diffused in the atmosphere: water vapor, carbon dioxide (CO_2), ozone, nitrogen dioxide, methane and chlorofluorocarbon (CFC) compounds (Wallace and Hobbs, 2005).

There has been an increase in both atmospheric greenhouse gas concentration and the average temperature on Earth during the last century. Following independent methodologies, estimates of the *National Oceanic and Atmospheric Administration* (NOAA) (http://www.ncdc.noaa.gov /sotc/global/), *Met Office* (http://www.metoffice.gov.uk/hadobs/hadcrut4/HadCRUT4_accepted.pdf) and the National *Aeronautics and Space Administration* (NASA)

(http://www.nasa.gov/topics/earth/features/upsDownsGlobalWarming.html) agree in finding that 14 of the 15 warmest years since 1880 have occurred in the lasts 15 years (1997-2011). The general increase of the average Earth's surface-atmosphere temperature is known as *global warming*. As it is clear from the last official *Intergovernmental Panel on Climate Change* report (IPCC 2007) (http://www.ipcc.ch/publications_and_data/ar4/syr/en/contents.html), a higher average temperature means more available energy for atmospheric dynamical process, thus extreme events, such as floods and hurricanes, have been growing in frequency and strength. This extra energy has very important consequences on climatic equilibrium of the entire planet; causing modifications of the general atmospheric circulation it implies changes in precipitation patterns. On average an increase in precipitation at latitudes higher than 30° has been observed, and a decrease is evident in tropical regions. It is worth pointing out that precipitation change patterns are more spatially and seasonally variable than temperature changes: for example a substantial drier climate has been observed in the Mediterranean even though it is located northern 30° N. Droughts have become more common, especially in the tropics and subtropics, since the 1970s. Political consequences of this last feature should be taken into account in order to prevent unsustainable immigrant pressure in the direction of regions of major water availability.

For a long time opinions of skeptics and supporters of a direct relationship between global warming and augmented greenhouse gas have been voiced in the scientific community. At the present time doubts that global warming is real and caused by human activities seem to be only pretext fashioned to hide problems that could have a very radical solution. The overall scientific consensus is that climate change and global warming are occurring now and only the increase in the atmospheric greenhouse gas concentration can explain the last 50 years of temperature increases (Pasini et al., 2012). Past climate had been warmer than what we can expect for the future, also for the most pessimistic scenarios, but changes had always happened in a geological lapse of time, allowing for environmental adaptation strategies (Kuypers et al., 1999).

The main contribution to the increased greenhouse effect came from carbon dioxide, which is

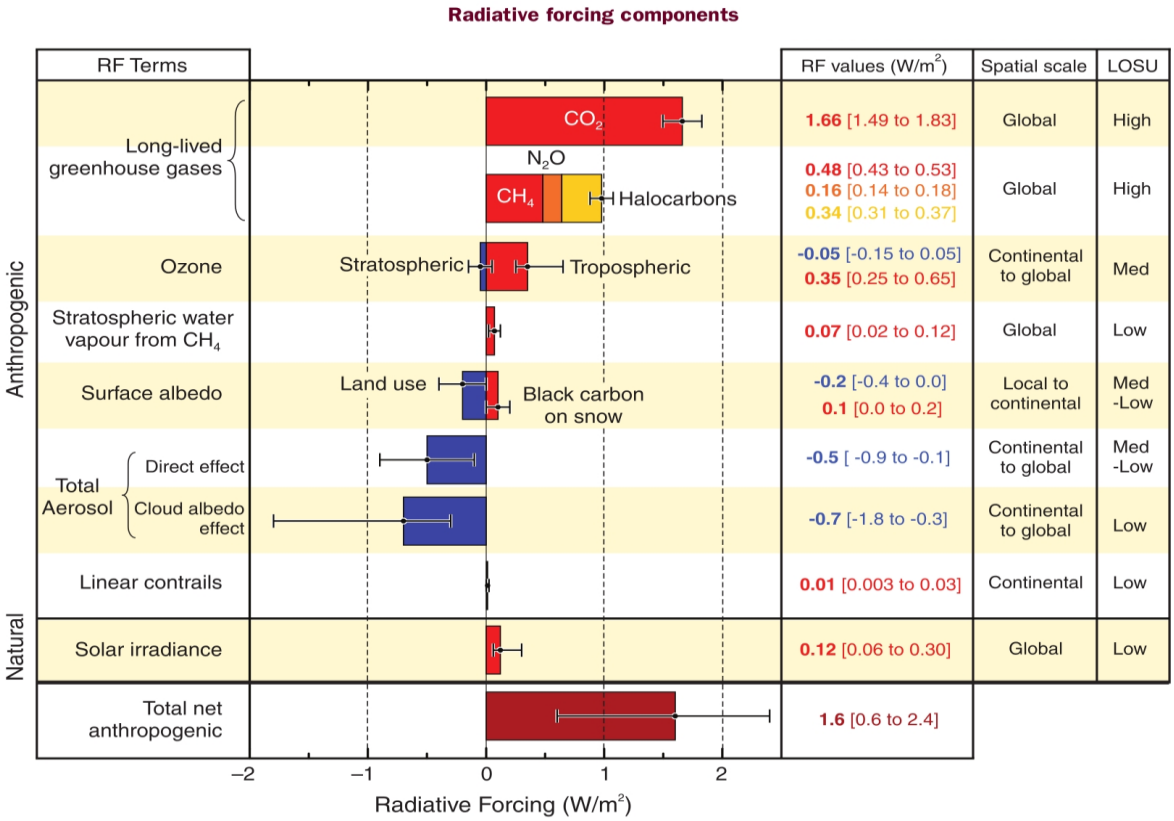

responsible for 65% of the radiative forcing (Fig. 1.1).

Fig.1.1. Radiative forcing distribution components (from IPCC-2007)

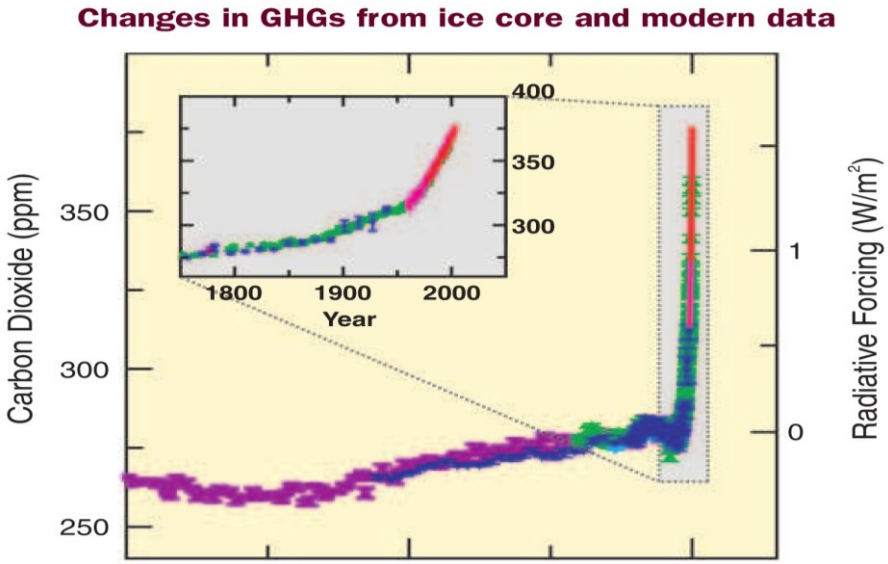

Fig. 1.1.2. . Carbon dioxide concentration trend of the last 4000 years (main frame), and carbon dioxide concentration trend of last two centuries (little frame). Data comes from air bubble trapped in the Antarctic and Greenland ice core (from IPCC-2007).

The average global carbon dioxide concentration over the last two centuries has increased from 280 ppm of the preindustrial age to nearly 400 ppm of today, but the main change has been occurred in the last thirty years. In Fig. 1.1.2 CO_2 concentration measurement data relative to the last two centuries and the last 4000 years are shown.

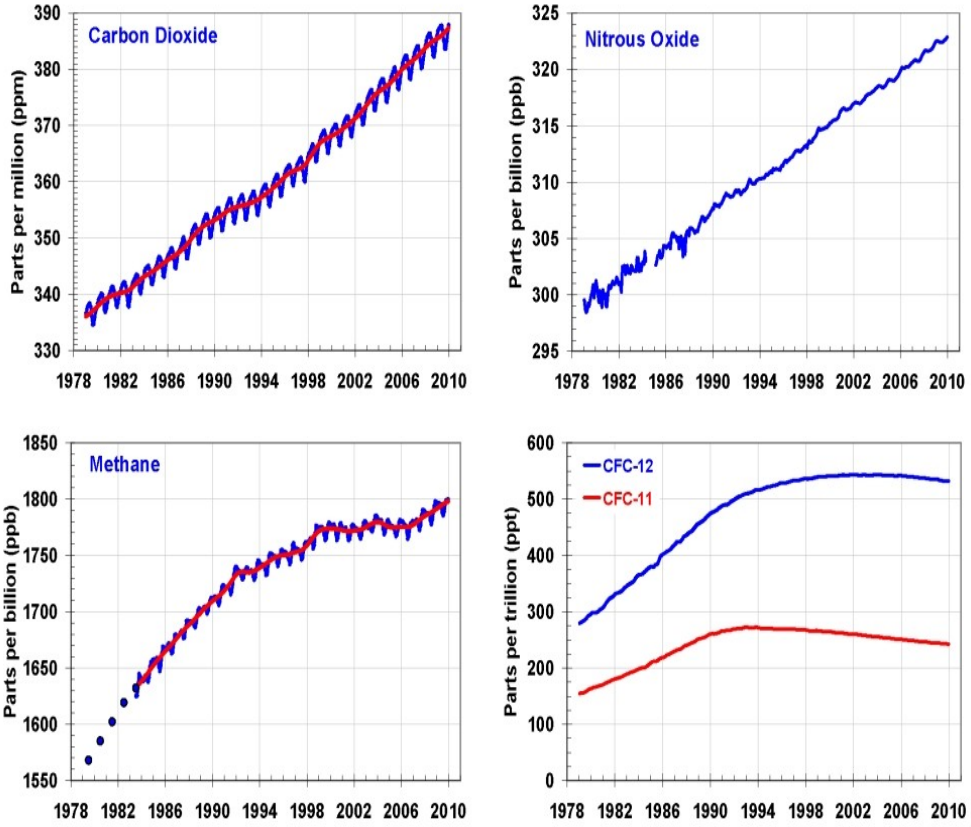

Fig.1.1.3. Trends of the most important greenhouse gas concentration for the last 30 years (from NOAA, http://www.esrl.noaa.gov/gmd/aggi/*)*

In Fig. 1.1.3 the concentration trend of the four most important radiative forcing greenhouse gases (GHG) is illustrated for the last thirty years. The positive trend of the most important GHG, carbon dioxide, can be observed, while the methane trend is near neutral. It is important to note that in the last ten years the chlorofluorocarbon (CFC) compound's concentrations are decreasing: CFCs play a little part in the greenhouse effect but they are responsible for the stratospheric ozone layer depletion (Wuebbles, 1982). The decrease of CFC compounds in the atmosphere is a consequence of the Montreal protocol, ratified by 197 states and the European Union in 1987: it represents a

success of science and of the international commitment able to forbid the use of CFC compounds. The international community has been following the same approach for limiting the CO_2 emissions. The Kyoto Protocol was adopted in Kyoto, Japan, on 11 December 1997 and entered into force on 16 February 2005. It is an international agreement that commits 37 industrialized countries and the European Community for reducing greenhouse gas emissions of an average of five per cent against 1990 levels over the five-year period 2008-2012. However for carbon dioxide the problem is more complicated than for CFC's. The reason lies in the relationship between carbon dioxide emissions and fossil fuel burning for energy supplies. A definitive solution implies the abandoning of fossil fuels for the renewable or atomic energy. At the moment this radical solution seems to be hard to realize because alternative energies are still more expensive of the ones based on fossil fuel.

To have a clear description of a problem is the first step to solving it. Therefore, in order to plan carbon dioxide emission reduction strategies, monitoring the atmospheric emission of the most important GHGs is required. Designing urban development, dictating the land management practices in agriculture and in general governing ecosystem management can allow for substantial benefits in combating climate change. The aim of the present work is to supply an instrument to monitor the environmental emissions of carbon dioxide. A simulation strategy to obtain high resolution carbon exchange maps at regional scale has been developed. It has been achieved improving the coupling of Advanced-Canopy-Atmosphere-Simulation-Algorithm (ACASA) model (Pyles et al., 2000a) to the Weather Research and Forecast (WRF) model (http://www.wrf-model.org/index.php). The former is one of the most elaborated multilayer Soil-Vegetation-Atmosphere-Transfer (SVAT) model of the last generation, able to simulate turbulent fluxes and meteorological variables within and above the canopy. The latter is one of the most accurate Numerical Atmospheric Model (NAM) at mesoscale assembled by National Center of Atmospheric Research (NCAR) and National Oceanic and Atmospheric Administration (NOAA). Running this coupled model at 3 Km resolution a monthly map of carbon dioxide exchange of the entire Mediterranean island of Sardinia was made. During this study a method that can be useful to assess

carbon exchange at regional scale has been validated.

1.1 Greenhouse effect

To truly understand the greenhouse effect it is important to present a general framework of the radiative processes occurring in the atmosphere. What is generally called electromagnetic energy flux is a beam of particles, photons, moving with the speed of light. They are emitted by the Sun where, because of very high temperatures and pressure, a huge number of hydrogen atoms are continuously fused into helium atoms. In helium atoms, electrons and protons are in a lower energy state. In order to maintain the energy equilibrium balance an enormous number of photons are isotropically emitted by the Sun. From a microscopic point of view their motion can be described by a statistical wave. This wave is the solution of the basic equation of the quantum mechanics, the Schrödinger equation. Each single photon brings an energy $E=h\nu$ and a momentum $P=h/\lambda$, where $h=6.626068 \times 10^{-34} m^2 kg\ s^{-1}$ is the Planck constant, ν the frequency and λ the wave length (Dirac, 1981).

When a photon beam reaches the Earth's atmosphere a first fraction of photons is scattered back to space, a second fraction is absorbed by atmosphere molecules and a third fraction is transmitted to a lower layer. So if we consider an air parcel in the middle of the atmosphere, the radiation received from the Sun is filtered by the upper level layer, which retains a part of the initial incident energy. As stated by the Beer's law, the amount of the retained energy is proportional to the thickness of upper layer, to the air temperature, pressure, density and moisture (Wallace and Hobbs, 1977). The mean temperature of the atmosphere is roughly constant over the time period needed to achieve equilibrium by the photon exchange; so all the energy absorbed should be re-emitted. Thermal

emission physics dominate the atmosphere-surface electromagnetic radiation, while solar hydrogen fusion and related emission processes dominate those from the Sun: this difference causes different "kinds" of electromagnetic radiant energy. So in the two cases considered above photons are characterized by different frequencies. The Heisenberg uncertainty principle (Dirac, 1981) states that the photon emission frequency is not fixed, but rather follows a statistical distribution. If a body completely absorbs the incident radiation and it has the maximum emission in all directions and for all the wave lengths it is called a *black body*. For a black body the statistical distribution of the emitted energy in the unit of time and of surface area E_λ (Wm^{-2}) at a certain wave length λ (m) is a function of temperature T (K) and is described by the Planck's law:

$$E_\lambda = \frac{8\pi\nu^5}{c^3} \cdot \frac{1}{e^{\frac{h\nu}{kT}} - 1} \tag{1.1}$$

where c (ms^{-1}) is the speed of light, and the Boltzmann constant k is equal to $1.3806503 \times 10^{-23}$ m^2 kg s^{-2} K^{-1} (Gasiorowicz, 2003).

From a radiative point of view the Sun and the Earth can be both considered black bodies. Integrating the Planck's law over the entire spectrum to account for the total energy radiated by a black body, we obtain the Stefan-Boltzmann equation:

$$E = \sigma T^4 \tag{1.2}$$

where E (Wm^{-2}) indicates the total energy emitted, T (K) is the temperature of the body and σ is the Stefan-Boltzmann constant: $5.67\ 10^{-8}$ $J\ m^{-2}\ s^{-1}\ K^{-4}$. It states that the energy emitted by a black body is proportional to the fourth power of its temperature.

It must be pointed out as black body radiation represents the upper limit to the amount of radiation that a real substance may emit at a given temperature. A body which has an emission rate lower than

a black body is called *gray body*. In contrast to the Sun and the Earth, the atmosphere enveloping our planet should be considered a gray body. In fact the energy radiated by the atmosphere is only a fraction of the energy radiated by a black body at the same temperature. The proportionality factor between the energy emitted by a black body and a gray body depends on the radiation wave length, thus for different frequencies different fractions of energy are radiated. Naturally the radiated energy must be equal to the absorbed one, (otherwise, from the principle of energy conservation, there should be a net storage of energy in the medium). Thus the absorbed energy depends on the wave length. This is the fundamental key principle needed to understand the greenhouse effect.

The radiation from the Sun has a peak around $0.50\ \mu m$ and spread over $0.35\ \mu m < \lambda < 3\ \mu m$ due to the radiation temperature of *5780 K*, the radiation from the Earth is centered around $15\ \mu m$ and spread over $5\ \mu m < \lambda < 100\ \mu m$ due to the radiation temperature of *288 K*. While the atmosphere is almost completely transparent to the solar radiation, it absorbs the main part of the energy emitted by the Earth's surface. This absorbed energy is isotropically re-radiated: roughly the half part leaves into space and the rest is emitted back to the Earth's surface. Therefore, because of the presence of the atmosphere, the re- radiation process of solar energy is strongly inhibited. According to the Stefan-Boltzmann law, the radiative equilibrium occurs for higher temperatures with respect to an atmosphere completely transparent for all the frequencies. This mechanism is also able to limit the thermal excursion between night and day, allowing for an energy flux (the long wave radiation) also when the surface does not receive the Sun rays. The greenhouse effect guarantees an acceptable living temperature on Earth: it can be easily calculated that the average temperature on surface without the greenhouse effect would be *255 K* (Wallace and Hobbs, 1977).

1.2 Carbon Dioxide balance

The carbon dioxide role in the global warming process has been previously clarified. So a description of the carbon cycle is important to have a general frame of the phenomenon.

From a general point of view, the carbon dioxide flux from the surface to the atmosphere is considered positive, conversely if the surface uptake CO_2 from the atmosphere to the flux is considered negative. An ecosystem that globally releases carbon dioxide is often called a "*source"* while if allow for a net capture CO_2 is often referred to as "*sink"*. Processes capturing CO_2 are essentially related to autotrophic organisms, known also as *Primary Producers*. They fix the inorganic carbon into organic compounds using the electromagnetic energy from the Sun. In terrestrial ecosystems the work is done mainly by plants while in the aquatic life it is done by algae, plants and phytoplankton. The rate of atmospheric CO_2 uptake per unit of surface area and time is called *Gross Primary Production* (GPP). It does not take into account the carbon dioxide emitted by plant during respiration, so the *Net Primary Production* (NPP) (Woodwell and Whittaker 1968) can be defined as the difference between GPP and the rate of released CO_2 per unit of surface area and time due to autotrophic organism respiration.

In the complex chain of ecosystem processes, it is possible to recognize another path followed by a part of this organic carbon: the heterotrophic organisms (omnivores and herbivores) use part of the organic carbon synthesized by autotrophic organisms as energy source. They release carbon dioxide during respiration. Littering the soil (such as their body mass at the end of their life) they furnish matter that can be transformed by organisms able to recycle the deceased: during the decomposition process another portion of carbon dioxide is released. The same process happens for autotrophic organisms when they finish their life cycle. During decomposition a part of the carbon sink in the soil and another is released in the atmosphere. A general scheme of the global carbon cycle is represented in Fig. 1.2.1.

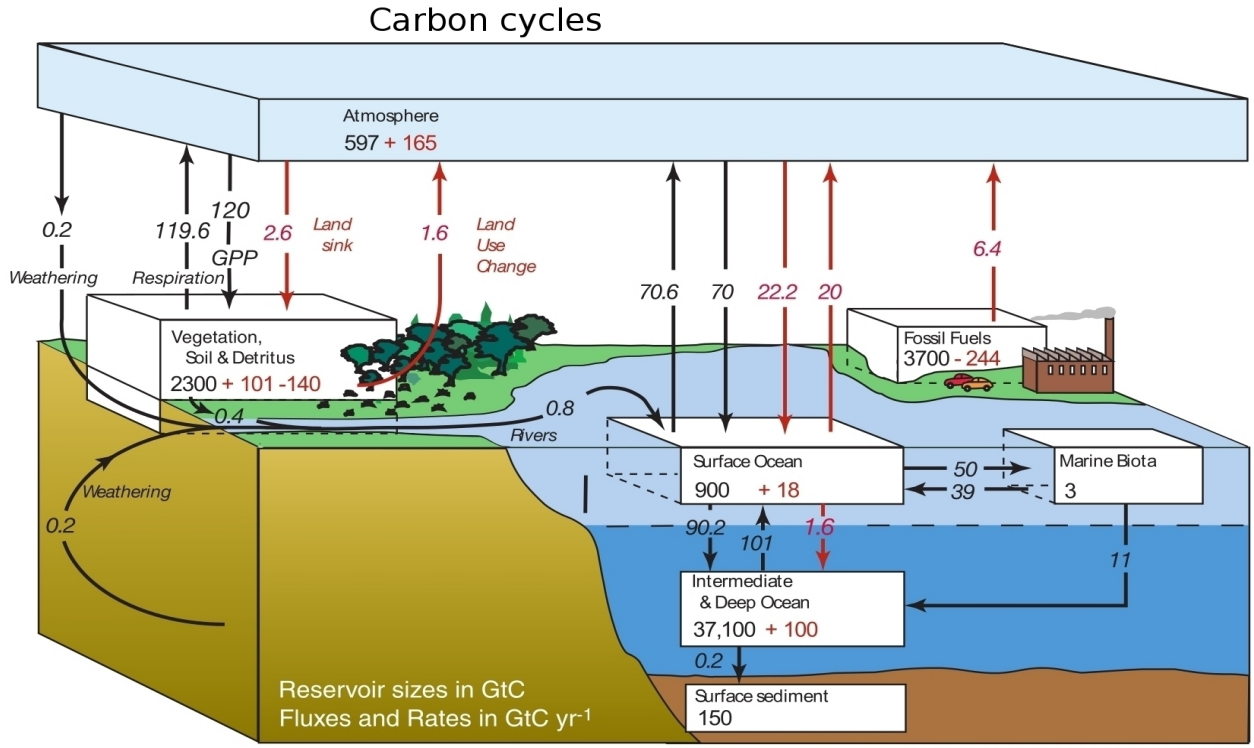

Fig. 1.2.1. General scheme of the global carbon cycle (from IPCC 2007)

If we consider an urban ecosystem we have to consider additional emission sources related to human activity known as *anthropogenic emissions*. Their amount represents only a few per cent (6.4 GtC/yr) of the total emission exchanged between the systems atmosphere-land (120 GtC/yr) and atmosphere-ocean (70 GtG/yr) (IPCC-2007). Anyway, despite a series of feedback processes enhancing the natural carbon uptake (Staudt et al. 2001), these anthropogenic emissions has been able to deeply modify the atmospheric CO_2 average concentration. Anthropogenic emissions are mainly due to the fossil fuel burning for energy supply, in Fig. 1.2.2 is described the partition of the components.

The *Net Ecosystem Production (*NEP) (Woodwell and Whittaker, 1968) is the variable that takes into account the emissions related to the heterotrophic organisms and the anthropogenic emissions, so it can be defined as the difference between the NPP and the rate of released CO_2 per unit of surface area and time due to the heterotrophic organism respiration and anthropogenic emissions.

A measurement station is not able to estimate the CO_2 flux distinguishing between organic or inorganic components, so it measures the sum of all the components of the carbon dioxide exchange flux: this variable is called *Net Ecosystem Exchange* (NEE); in accordance with a flux definition and conversely to the previous three definitions, it is considered positive if there is a net carbon emission in atmosphere. Inorganic carbon sources can essentially be identified with volcanic processes and processes that involve weathering dissolution of carbonates. Inverse process of sediment accumulation represents a carbon sink. Their contributions are estimated in the order of 0.1 GtC/yr.

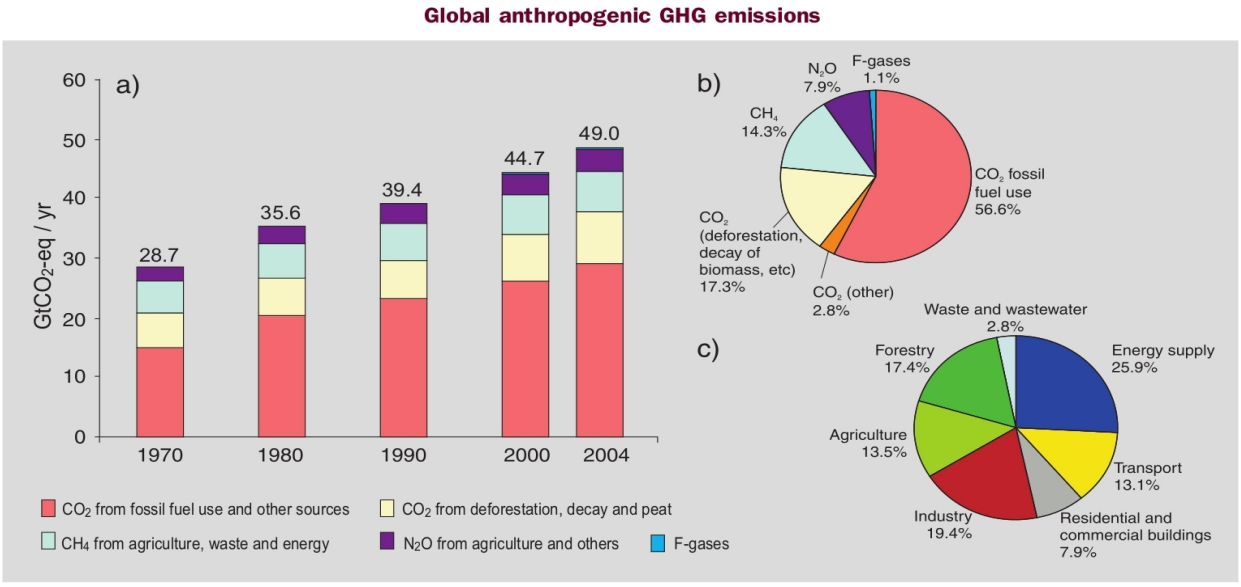

Fig. 1.2.2. *(a) Global annual emissions of anthropogenic GHGs from 1970 to 2004. (b) Share of different anthropogenic GHGs in total emissions in 2004 in terms of CO_2-eq. (c) Share of different sectors in total anthropogenic GHG emissions in 2004 in terms of CO_2-eq. (Forestry includes deforestation)* (from IPCC 2007)

2 State of the art and objective

An accurate estimate of the carbon exchange is crucial in order to keep a sustainable healthy thermal equilibrium of the planet and therefore plan CO_2 emission reduction strategies. Designing urban development, dictating the land management practices in agriculture and in general governing ecosystem management can allow for substantial benefits in combating climate change. A large scale assess can be retrieved collecting regional scale estimates, which assumes importance in the panorama of the global carbon exchange.

Different approaches are found in literature to estimate carbon dioxide exchange at regional scale.

The "*top-down*" or *inversion* approach is based on the analysis of observed flux data at selected sites combined with concentration measurements. Information are elaborated with Lagrange type dispersion and transport computational models: carbon exchange at regional scale is retrieved following the inversion path of diffusion processes and atmospheric flows (Göckede et al. 2010; Sarrat et al 2009; Gerbig et al. 2003; Gourdji et al. 2010). This indirect reconstruction of fluxes is in principle comprehensive of all kind of emissions: fuel burning plus all ecosystems sources and sinks plus all other processes emitting or absorbing CO_2 are considered. Results are generally coherent with observations. On the other hand they are in a coarse resolution that strictly depends on the mean distance between the observational stations.

The "*bottom-up*" or f*orward* approach is based on direct reconstructions of local fluxes and it responds to the requirement of higher resolution data. If it is possible to directly measure the changes in carbon stock at repeated intervals, then the cumulative amount can be calculated by integrating them over time (Ciais et al. 2010; Hsu et al. 2010). Specially for long term cumulative

anthropogenic emissions, carbon flux inventories are retrievable from economic parameters and energy supplies (Zhaoa et al., 2012).

With respect to shorter time flux variability, *in-situ* flux observations offer the most accurate data. It is clearly impossible to install the really expensive monitoring stations scattered over the whole territory, therefore, to obtain data from regions not covered by "*in situ*" observations, the simulation approach is achieved. This work has been carried out by the Soil-Vegetation-Atmosphere-Transfer (SVAT) models that, using meteorological and morphological input data, can accurately simulate turbulent fluxes. Outputs are relative to single points representative of limited areas of the magnitude order of 1 Km^2. In the last few years, SVAT models have been coupled to General Circulations Models (GCM) to obtain maps at larger scale. GCMs are able to provide the morphological and meteorological input data for the points representative of single pixel. Fluxes relative to each single pixels are then assembled in maps. In this way several studies leaded to the creation of CO_2 flux maps at regional scale. Sarrat et al. (2007) coupled the GCM *Meso-NH* with the SVAT model *Interactions-Soil-Biosphere-Atmosphere-CO_2-reactive* (ISBA-A-gs). They obtained a 2 Km resolution CO_2 flux map for a 300Km x 300Km domain located in the south west of France. In 2009, Tolk et al. coupled the GCM mesoscale model *RAMS-Leaf3* with the SVAT model *5PM* to simulate 22 days of CO_2 exchange for a 320Km x 320Km domain located in Netherland. A different approach was followed by Marushchak et al. in 2012 to calculate the total annual emission for a subarctic tundra area of 98.6 Km^2 in the Northeast European Russia. In this case the annual carbon exchange was obtained starting from a great number of observations spread over the territory and scaled up to the whole studied area using two data sets. A land cover classification and a leaf area index map, both based on field data and 2.4 m pixel-size satellite image provided the base to characterize fluxes at extremely high resolution.

Most of the carbon flux maps at regional scale were collected over several ecosystems located on region with continental climate, only few papers dealing with Mediterranean climate carbon fluxes can be found (Gioli and Miglietta, 2007). This lack of knowledge, concerning with these climate

ecosystems, is worth it to be investigated.

In the present work, within the general frame of the bottom-up approach, the coupling between the Advanced Canopy-Atmosphere-Soil Algorithm (ACASA) model (Pyles et al., 2000b) and the Weather Research and Forecast (WRF) model (Skamarock and Klemp 2008 http://www.wrf-model.org/; http://www.mmm.ucar.edu/wrf/users/) has been used to fill this knowledge gap about the Mediterranean climate ecosystems.

Therefore, the main aims of this study are:

- test the coupled model WRF-ACASA performance on grape vineyard ecosystem located in the south of Sardinia, using Eddy Covariance micrometeorological observed data
- validate a method to create maps of carbon fluxes at regional scale
- create the map of CO2 flux for the Sardinia island for the month of May 2010

The island of Sardinia was selected for three reasons. First because, in force of its position, it allows for analysis of a large scale carbon exchange concerning with a region characterized by the unique variability of the Mediterranean climate. Second because the wide range of different ecosystems supply a new test case for the WRF-ACASA model. Third because the region surrounded by the sea can be considered an isolated source/sink system: this last feature could be very useful in future studies based on the inversions approach concerning the Mediterranean basin.

The needs to consider a peak period for photosynthetic activity and physiological process controls, together with a relative lack of water stress not limiting the surface-atmosphere CO_2 exchange, lead to the choice of the period.

In the next chapters, it follows a brief description of the general structure of both Numerical Atmospheric Models and Soil-Vegetation-Atmosphere-Transfer models, while a detailed description of the ACASA and WRF models, together with their coupling, is shown in the Materials chapter.

3 Structure of Numerical Atmospheric Models

Numerical Atmospheric Models (NAM) include the set of mathematical models able to simulate certain aspects of atmospheric dynamics at regional (Mesoscale/limited area) or global (GCM) scales. Given the fluid nature of the atmosphere, all the GCM are built on the basic set equations of fluid dynamics known as Navier-Stokes (N-S) set. Starting from observed data, NAMs simulate the future atmospheric state for a time interval that strictly depends on the spatial resolution of the forecast. Discretization of the mathematics solving the Navier-Stokes equations requires care in selecting the spatial grid and time-step intervals (the finer the spatial resolution, the shorter the time step). The N-S set of partial differential equations are not currently known to have analytical solutions, and therefore solutions to these equations are instead approximated with discrete numerics. As model physics and precision improve, a growing computational effort is required. At the same way more accurate schemes, able to better describe the meteorological processes occurring in the system, imply a higher computational speed. The aim of this chapter is to give an overview on how a numerical atmospheric circulation model is structured. The first point of concern is the equations used to describe the atmosphere, while the second is how they are numerically solved.

3.1 Deducting the equation

The Navier-Stokes set comprises five scalar equations derived starting from the principle of three-dimensional momentum conservation, the mass conservation, and energy conservation. The principle of three-dimensional momentum conservation states that moving materials conserve their momenta (*mv)* even while forces (*F)* may act on them. The relation between force and momentum

variation is described by the vectorial equation:

$$\vec{F} = m \cdot \vec{a} = \frac{d}{dt} m \cdot \vec{v} \tag{3.1.1}$$

(see for examples Goldstein et al. 2002). Considering a fluid, the left side forcing terms in this general equation are three (Holton 1992). The first is the gravitational vertical force for an air parcel per unit mass:

$$\frac{d\vec{F}_g}{dm} = \vec{g} = -G\frac{M}{r^2}\vec{k} \tag{3.1.2}$$

where g represents the gravitational acceleration: it is the Newtonian gravitational law where M is the earth mass, r the distance from the earth barycenter and $G=6.67259\ 10^{-11}\ N\ m^2 kg^{-2}$ the universal gravitational constant. The second is the pressure gradient force for unit mass:

$$\frac{d\vec{F}_P}{dm} = -\frac{1}{\rho}\vec{\nabla}P \tag{3.1.3}$$

where P represents the pressure field and ρ the air density, it states that the force is proportional to the pressure gradient and it is directed from regions of high to regions of low pressure. The third is the viscous force for unit mass:

$$\frac{d\vec{F}_\tau}{dm} = \nu\frac{1}{\rho}^2\vec{\nabla^2}\vec{U} \tag{3.1.4}$$

where ν is the air viscous kinematic coefficient depending on the specific fluid and U is the

vectorial velocity. It states that the force is proportional to the spatial variations of the gradient of the velocity.

It is possible obtain the momentum conservation equation in the non-inertial rotating frame of the earth surface. If the general equation is projected on a spherical coordinate system *O=O(r,θ,ϕ,)* centered on the Earth's barycenter, rotating around the vertical axis with the same angular velocity of the Earth ω, considering the inertial forces we have:

$$\frac{du}{dt} = F_{\tau x} - \frac{1}{\rho}\frac{\partial P}{\partial x} + 2\omega v\sin(\Phi) - 2\omega w\cos(\Phi) + \frac{vu}{a}tg\Phi - \frac{uw}{acos\Phi} \tag{3.1.5}$$

$$\frac{dv}{dt} = F_{\tau y} - \frac{1}{\rho}\frac{\partial P}{\partial y} + 2\omega u\sin(\Phi) - \frac{u^2}{a}tg\Phi - \frac{wv}{a} \tag{3.1.6}$$

$$\frac{dw}{dt} = F_{\tau z} - g - \frac{1}{\rho}\frac{\partial P}{\partial z} + 2\omega u\cos(\Phi) - \frac{u^2 + v^2}{a} \tag{3.1.7}$$

Where *a* is the earth radius, *Φ* the latitude, *θ* the longitude, *u* is the velocity along parallels related to the local variation in time of the coordinate $x=a\cdot\Phi$, *v* is velocity along the meridians related to the local variation in time of the coordinate $y=a\cdot\theta$ and *w* is the vertical velocity related to the local variation in time of the coordinate *z=r*. The term involving *2ω is* known as *Coriolis acceleration* and represents the inertial apparent force due to rotation of the frame with earth.

The fourth scalar equation is the mathematical formulation of the mass conservation principle:

$$\frac{d\rho}{dt} + \rho\cdot\vec{\nabla}\cdot\vec{V} = 0 \tag{3.1.8}$$

and it states that the variation in time of the density of a fluid is equal to the divergence of the mass flux $\rho\vec{V}$ vector (Holton, 1992).

The last equation descend from the first principle of thermodynamics which states that the energy entering a fluid is partially converted into work done by the system and partially in internal energy:

$$J = p\frac{d}{dt}\left(\frac{1}{\rho}\right) + C_v\frac{dT}{dt} \tag{3.1.9}$$

where J (Wm^{-2}) is the flux of total thermal energy (radiant, latent and convective, conductive) for unit mass ingoing in the unit air parcel, T the temperature (K) and C_v the specific heat at constant volume ($J\ kg^{-1}\ K^{-1}$) (Holton, 1992).

Scale analysis can simplify a little the momentum equations. Considering layer of atmosphere not in direct contact with the surface, the term in the momentum equation representing the viscous force can be neglected because it is comparable with the other only at the scale of millimeters from the surface. In all three momentum equations also, the term involving the earth radius (*a)* can be neglected being two order lower than the pressure gradient component. Conversely only in the vertical motion equation the term involving $cos\phi$ can be neglected (Holton, 1992).

The set is made of seven unknown variables ***u,v,w,P,T,J,ρ*** and since there are five equations, the set is not closed. The closure of the model can be realized using the perfect gas equation to express the temperature T in function of P, the hydrostatic approximation to relate pressure and density, the radiative transport equation to estimate the radiative forcing J, the latent heath can be estimated with the Penman-Monteith equation. The choice of the relations used to close the set depends on the particular model and within the same model there are often different closure options.

It is important to underline how the set equations are linear at the first differential order, it means that there exists a general analytic solution in closed form, provided that boundary and the initial conditions of the air mass are available.

Observations are made relative to a fixed point in which it is possible to measure a local variable at different times. So by reason of the flow, the time series of measurements refers not to the same air parcel but at the one that passes at that moment in the place in which the meteorological station is

located: it is hard to follow an air parcel to measure how its properties vary over time. Thus, to use the initial and boundary conditions available it is necessary that a "local" variation appears instead of the classical total variations. It can be done by decoupling the derivative component relative to time from the ones relative to space. Considering a general scalar field *T=T(t,x,y,z)* representing, for example, the temperature, we can write:

$$\frac{dT}{dt} = \frac{\partial T}{\partial t} + \frac{\partial x}{\partial t}\frac{\partial T}{\partial x} + \frac{\partial y}{\partial t}\frac{\partial T}{\partial y} + \frac{\partial z}{\partial t}\frac{\partial T}{\partial z} = \frac{\partial T}{\partial t} + \vec{U}\vec{\nabla}T \qquad (3.1.10)$$

It states that the total instantaneous rate of change of the variable *T* following the motion *dT/dt* is equal to the local change of *∂T/∂t* (exactly what a station can measure in a fixed point) plus the variation due only to the spatial movement along an instantaneous "picture" of the scalar field, known as the advection term. The first side of the equation is referred to as the Lagrangian derivative or total derivative, while the local derivative *∂T/∂t* is known as the Eulerian derivative. By introducing the Eulerian derivative in the Navier-Stokes set it is possible to take advantage of measured fields to find its solutions, but this spells the end of linearity of the equations with respect to the first derivative. This is the reason why the only possible real general solutions of the Navier-Stokes set are obtained using discrete numerics.

The momentum equations in which viscous forces are neglected are able to accurately describe the free atmosphere, which is the part not directly influenced by the surface. In the free atmosphere the flow remains mostly non-turbulent. Turbulent flows are characterized by irregular quasi-random motions spreading in a continuous spatial and temporal spectrum, so nearby air parcels drift apart, mixing properties such as momentum and potential temperature (Stull, 1988).

Due to the molecular viscous forces acting within the first few millimeters of all surfaces, a weak wind blowing across all types of surfaces can create a strong velocity shear. This shear is thus able to continuously generate turbulent eddies in the lowest part of the atmosphere known as the

"*planetary boundary layer*"(PBL). Unlike large-scale flows, which have depth scales that are small compared to their horizontal scales, the turbulent eddies of concern in the PBL tend to have similar horizontal and vertical dimensions: the largest of these eddies often range from 30 m in condition of nocturnal strong static stability to 3 Km in conditions of deep convective activity. These turbulent motions have embedded within them spatial and temporal variations at scales much smaller than those resolved by the meteorological observing network. From a macroscopic point of view, a turbulent flow will always have scales that are unresolvable: they have frequencies greater than the observation frequency and spatial scales smaller than the resolution of the observations. They may range from as little as 1 mm and 10^{-3} s. Even if it is possible to detect the field locally at such high resolution, the information is often not applicable to the parameterized scales of the meteorological model. The turbulent flow remains "localized" information that is not possible to extend to a larger region for the continuously changing field of space and time. With respect to the PBL, also if from a theoretical point of view the set of Navier-Stokes is always able to govern the motion, in practice should be faced the problem indirectly related to the viscous force.

Another approach is required to treat the turbulent flow involving the PBL. It requires further modification of the Navier-Stokes set of equations.

In order to extract from the turbulent flow the mean component representing the large scale flow, as in the scheme introduced by Reynolds (Holton, 1992; Stull, 1988; Wallace and Hobbs, 2005) it is possible to decouple the variables related to the flow into a slow-varying mean component and a fast-varying eddy component. The former is obtained from the turbulent flow averaging over a long enough time to average out the effects of small-scale eddy fluctuations, but short enough to retain trends in the main (resolved-scale) flow. The latter is obtained by the difference from the original field and the main flow. For example, the velocity in the parallels direction (*u)* can be expressed as $u=\langle u\rangle+u'$ where $\langle u\rangle$ and u' are respectively the main and the eddy flow. It is important to point out how the mean value of an eddy field variable is zero: $\langle u'\rangle=0$. It implies that also the mean of the product of a mean flow variable with an eddy flow variable is zero:

$$<<u'><\theta>>=<u'><\theta>=0<\theta>=0 \quad (3.1.11)$$

Conversely, the mean of the product of two eddy flow variables $<u'\theta'>$ generally does not vanish. The term $<u'\theta'>$ assumes enormous importance within turbulence theory and all of meteorology. It is known as eddy covariance because it is the mean value of the product of the two deviations from its averaged value, $<u>$ and $<\theta>$ in this example, and it represent the turbulent flux of the variable θ transported with the velocity u' in the parallels direction. The eddy covariance is positive if terms are both positive or both negative, in this case they are positively correlated. While if they have opposite sign they are negatively correlated.

The temperature that an air parcel assumes if adiabatically expanded or compressed to reach a specific pressure (generally the sea surface pressure) is called potential temperature and is generally indicated with the Greek letter θ. Following the approach suggested by Holton (1992) or at the same way by Stull (1988) it is possible introduce the potential temperature θ into the energy conservation equation and the continuity equation. The former in the Reynolds form becomes:

$$\frac{d<\theta>}{dt}=\frac{J}{C_p}\cdot\left(\frac{P\_s}{<P>}\right)^{R/c_p}-\left(\frac{\partial<u'\theta'>}{\partial x}+\frac{\partial<u'\theta'>}{\partial y}+\frac{\partial<w'\theta'>}{\partial z}\right) \quad (3.1.12)$$

while the latter becomes:

$$\frac{d<\rho>}{dt}=-<\rho>\left(\frac{\partial<w>}{\partial z}+\frac{\partial<v>}{\partial y}+\frac{\partial<u>}{\partial x}\right)-\left(\frac{\partial<u'\rho'>}{\partial x}+\frac{\partial<v'\rho'>}{\partial y}+\frac{\partial<w'\rho'>}{\partial z}\right) \quad (3.1.13)$$

Applying the Reynolds averaging to the horizontal momentum of the Navier-Stokes equations, after setting $2\omega sen=f$ and considering $\rho=<\rho>$ (Boussinesq approximation, Holton 1992) we obtain:

$$\frac{d<u>}{dt} = -\frac{1}{<\rho>}\frac{\partial <P>}{\partial x} + f\cdot <v> - \left(\frac{\partial <u'u'>}{\partial x} + \frac{\partial <u'v'>}{\partial y} + \frac{\partial <u'w'>}{\partial z}\right) \qquad (3.1.14)$$

$$\frac{d<v>}{dt} = -\frac{1}{<\rho>}\frac{\partial <P>}{\partial y} - f\cdot <u> - \left(\frac{\partial <u'v'>}{\partial x} + \frac{\partial <v'v'>}{\partial y} + \frac{\partial <v'w'>}{\partial z}\right) \qquad (3.1.15)$$

For the vertical equation the Boussinesq approximation is not possible because it would cut off the buoyancy force, but considering the mean flow in hydrostatic equilibrium it is possible to write:

$$\frac{d<w>}{dt} = -\frac{1}{<\rho>}\frac{\partial <P>}{\partial z} - g\cdot\frac{\theta'}{<\theta>} - \left(\frac{\partial <u'w'>}{\partial x} + \frac{\partial <u'w'>}{\partial y} + \frac{\partial <w'w'>}{\partial z}\right) \qquad (3.1.16)$$

Outside the boundary layer, the turbulent flux terms can be generally neglected, except for conditions of strong wind shear as can occur in jet stream cores or in thunderstorm convective clouds. But the same approximation is not possible in the PBL, also if we are interested only in the main flow.

Some assumptions can be made to simplify the set for the turbulent flow: in regions of horizontal homogeneity the horizontal turbulent flux can be neglect.

In the equations where the Reynolds average introduced the new unknown eddy variable another closure problem turns up. This can be overcome through applying a series of assumptions in order to relate the five mean variables ***u,v,w,P,T*** to the eddy variable. The most widely-used and relatively simple theory, k-theory, linearly relates eddy variables to local mean variables and implies that all fluxes proceed down-gradient. The set can be closed in a more elaborate and sophisticated way considering theories developing parameterizations based on differential relations of higher order, such as the influences of larger eddies acting within the system and related potentials for counter-

gradient flux transport.

3.2 Numerical solution: the finite difference method

The numerical solution for the equation set described above is obtained through integrating the equations with a finite-difference method (Mitchell and Griffiths, 1980). The basic idea is to substitute the incremental ratio between two adjacent points for which the solution is required in place of the derivative present in the analytical equations. Thus the entire domain, spatial and temporal, is replaced with a discrete domain of grid points: the final solution will be available only for this point. As the grid step tends toward zero points are closer and the incremental ratio tends to the derivative, therefore the numerical solution tends to be exact. There are various ways to approximate the derivative in the grid point. If the incremental ratio is calculated considering the point to which the derivative refers and the next ones in the direction in which the derivative is taken, the scheme is called *Forward Finite Difference* (FFD). If the incremental ratio in calculated considering the point to which the derivative refers and the previous ones the scheme is called the *Back Finite Difference* (BFD). If the two adjacent points are used, the previous and the next lying in the grid in the direction where the derivative is taken, the scheme is called the *Central Finite Difference* (CFD).

The CFD will give better results because the best approximation of derivative is in the middle of the interval limited by the two points used to calculate the incremental ratio: in the CFD scheme the middle of the interval coincide with the point in which the approximated derivative is taken. While in the BFD and FFD scheme the best approximation point lies on the left or on the right respectively of the point for which the approximated derivative is taken. The CFD scheme,

involving three points, requires more complicated code and is more computationally exhausting. Generally a CFD scheme is adopted for spatial grids and an FFD scheme for the time grids. The reason for this diversity lies mainly on initialization: a CFD scheme for a time grid requires initial conditions at two different time steps, while the observations are relative to a single time (Leveque, 1992).

If the function obtained from substituting the difference finite derivative for the analytic derivative tends to the analytic function as the grid step tends to zero, then the scheme is called *coherent*. If the error due to the initial data approximation, as it propagates in the solution, remains stable or lowers, then the scheme is called *stable*. If coherence and stability conditions are verified, the Lax equivalence theorem (Strikwerda, 1989; Lax and Richtmyer, 1956) assures that the approximated final solution in the grid point can tend to the analytic solution as the grid step tends to zero: this last condition is called *convergence* of the scheme and is the requirement to obtain a correct solution.

4 Structure of Soil-Vegetation-Atmosphere-Transfer model

The Soil-Vegetation-Atmosphere-Transfer models (SVAT) are simulation models able to reconstruct turbulent fluxes of mass and energy between the surface and the planetary boundary layer. Turbulent fluxes emission is the final result of a complex process in which simpler processes interact with each other, SVAT models supplies a numerical representation of this complex process. Therefore they are not causal theoretical models *explaining* the behavior of the complex system, but rather they *simulate* it; a SVAT model can be described as a general frame in which simpler process models, that already exist, are nested. Turbulent fluxes are retrieved starting from morphological parameters that characterize the vegetation and land surface together with meteorological data.

In general complex ecosystems have very different behaviors depending on their characteristics, so the model calibration assumes great importance and strongly depends on the considered system. Input data describe the characteristics of a single point for which the simulation is conducted. This single point should be chosen in order to represent a uniform well defined area in which the simulation validity can be extended. This local validity area has generally magnitude order of some Km^2. Only assembling results of simulation conducted for different points it is possible reconstruct information at larger scale, which in principle can be extended at global scale.

Meteorological data comprise temperature, humidity, radiation, precipitation, wind, atmospheric pressure; soil conditions data comprise temperature and humidity at different depths; while characteristics related to the ecosystem morphology comprise optical canopy parameters, soil type and biome/land use. The meteorological data can be scanned using weather stations, or by coupling the SVAT model to a GCM (Xiu and Pleim 2000; Chen and Dudhia, 2001; Manning and Chen,

2005) able to provide the required information.

Typical turbulent flux outputs comprise kinetic energy, water vapor, sensible heat, carbon budget and vertical profile of meteorological data. All the output data are available in a broad lapse of time step ranging from one day to 30-60 minute depending on the model.

The “big leaf” category, used in growth process and biogeochemical model or when computation time is a problem, can be considered “zero dimensional model”: output comes only in punctual bulk information without a vertical profile. Sometimes, such models are run with a daily time step e.g. PnET-N-DND, (Kiese et al., 2005) in global climate model simulations. The more sophisticated “intermediate big leaf” models introduces some implicit forms of vertical dimensioning in the parametrization of radiation, turbulent exchange and stomatal conductance. Time step are generally shorter then one day as for example PLATIN (Falge et al., 2005), facilitating usages that require diurnal cycling information in fluxes and micro-environmental conditions. The “multi-layer” set represents the latest generation “state-of-the-art” models, and are the most sophisticated both theoretically and computationally. They divide the canopy and the soil in a great number of layers in order to give the vertical profile of the simulated variables. Typical time steps are about 30-60 minute e.g. HIRVAC model, (Goldberg and Bernhofer, 2001), MixFor-SVAT model (Olchev et al., 2008), Svat-CN model (Kuhnert and Köstner, 2009). The higher accuracy of the “multi-layer” with respect to the “big leaf” requires a larger number of a priori parameters.

Supplying the best way to simulate interactions between atmosphere and surface, SVAT models are used in larger scale gridded atmospheric models by meteorologists and climatologists: the former use SVAT to simulate the PBL in the weather forecast, while the latter use SVAT as a preliminary base of work to evaluate future climatic scenarios or to analyze past climate. SVAT models are also exploited by ecologists and biogeochemists to study ecosystem behaviors in different environmental conditions. They are also important to plan the programming line in agriculture (e.g. water budget) and to design the urban development (Marras et al. 2009).

4.1 Processes involved in a SVAT model

The individual processes involved in a SVAT model are the fluid dynamics processes of the planetary boundary layer, radioactive transport, energy fluxes from atmosphere to the Earth's surface, evapotranspiration, functional stomatal processes, photosynthesis and respiration.

The general equations governing the planetary boundary layer are, again, the Navier-Stokes set equations, the same used by GCM for PBL described in the previous chapter. The radiative transport process, as described in the first chapter, supply the energy to the surface needed to drive the physics and physiology that generate the energy, mass, and momentum fluxes emanating there from. The atmosphere-transmitted fraction of the solar energy reaching the surface has a band peak around $0.50\mu m$ and spread over $0.35\mu m<\lambda<3\mu m$. While the lower frequency energy radiated directly by the atmosphere has a wave length $5\mu m<\lambda<100\mu m$. The sum of these two components represents the incident energy $\boldsymbol{R_s}$. The former is clearly present only during the day and strongly inhibited in presence of clouds that can reflect and scatter a significant part of the energy, so it is possible divide the solar radiation in direct and diffuse (Wallace and Hobbs, 1977). At the same way, the long wave component is the sum of the energy coming from two different processes: the first is the direct thermal emission of the air molecule that radiate isotropically, the second is the fraction of the radiation emitted from the earth that is scattered back toward the surface. In this case the effect of clouds is to improve the mechanism of emission-scattering. The energy flux $\boldsymbol{R_s}$ reaching the surface is in part reflected back and in part absorbed by the surface. The fraction of energy reflected back respect to the incident energy is called *albedo* $\boldsymbol{A}$ so the net energy absorbed $\boldsymbol{R_n}$ by the surface is $\boldsymbol{AR_s}$. The energy balance surface equation describe how the net radiation forcing term $\boldsymbol{R_n}$ is partitioned into latent heat intensity flux $\boldsymbol{LH}$, sensible heat intensity flux $\boldsymbol{H}$, soil heat storage intensity flux $\boldsymbol{G}$, biomass heat storage intensity flux $\boldsymbol{S}$, and into the ecosystem metabolism

process intensity flux ***M***:

$$R_n = H + G + S + LH + M \tag{4.1.1}$$

Considering land surface during the day, the radiative short wave term is greater than the emitted long wave component so $R_n > 0$ and a positive amount of energy is absorbed by the soil surface. Here a first part ***G*** is diffused under the surface in the lower soil layer and a second part ***S*** is diffused in the living elements of the ecosystem where it is stored. Living elements are responsible also for a third part ***M*** of energy related to metabolic processes. A fourth part ***H*** warms the air directly in contact with the surface causing an expansion of the fluid, so the augmented specific volume guarantees the buoyancy force sufficient to enable air to leave the surface in the form of turbulent flux of sensible heat. The fifth part ***LH*** warms the soil moisture that can pass into/out of the vapor state, creating a turbulent flux of latent heat. This is a really complex process actually mediated by the plant activity. Often modelled by invoking resistance metaphors, it can be described by the Penman-Monteith equation (Monteith, 1981):

$$LE = \frac{sR_n + \rho C_p \cdot g_a \cdot \delta_e}{s + \gamma(1 + g_a / g_s)} \tag{4.1.2}$$

where R_n is the net radiation, δ_e the vapor pressure deficit, g_a the aerodynamic boundary layer conductance, g_s the surface bulk conductance, γ the psychometric constant, ρC_p the volume heat capacity of air at constant pressure, s the derivative of saturation vapor pressure respect to the temperature, ***LE*** the latent energy of vaporization. The Penman-Monteith equation is by far the most commonly relation used for such calculations within big-leaf and similar models. Latent heat

flux is deeply influenced by different kind of vegetation which can have different g_s: this factor is very important in modeling the turbulent flux. Generally the surface bulk conductance g_s is considered linearly proportional to the *Leaf Area Index* (LAI) that is the area of leaf coverage per unit area of land surface. It is also considered linearly proportional to the maximum carboxylation rate VCMAX, that is a measurement of the velocity of the process by which, starting from the atmospheric carbon dioxide, carbon compounds is synthesized:

$$g_s = g_l \cdot LAI \cdot VCMAX \tag{4.1.3}$$

The single leaf conductance g_l has a maximum for a temperature interval in order to open the stems during the normal photosynthetic activity. The leaf conductance decrease in conditions of high temperature specially if coupled with water stress or high vapor pressure difference between the inner part of the leaf and the air. Also for temperatures lower the 0°C conductance decreases in order to prevent icing (Smirnova et al., 2000). So collecting all this term g_l can be expressed as:

$$g_l = g(LAI_a) \cdot f(\delta_e) \cdot f(T) \cdot f(\psi_l) \tag{4.1.4}$$

where $g(LAI_a)$ is the leaf conductance function of the only *LAI* active component, $f(\delta e)$ is the factor due to the vapor pressure difference between the inner part of the leaf and the air, $f(T)$ is the factor due to the leaf temperature, $f(\psi)$ a function of the water potential taking into account the water stress (Jarvis, 1976; Farquhar et al., 1980; Farquhar et Caemmerer, 1982; Stewart, 1988; Leuning, 1990; Collatz et al., 1991; Collatz et al., 1992; Cox et al., 1998; Smirnova et al., 2000).

During the night the flux are often reversed in sign. Without the solar radiation the surface emits

more energy than what it receives and it tends to get colder. The energy released into the PBL during the day in the form of sensible and latent heat particularly can return to the surfaces at night in the form of negative sensible heat transfer. So the air gives heat back to the surface lowering its temperature and inverting the sensible heat flux. If the temperature of air is cold enough to origin condensation of air moisture also the latent heat flux can be reversed with respect to the diurnal flux.

Others important processes considered in a SVAT model are photosynthesis and plant respiration. Photosynthesis is the physical-chemical process by which plant and algae introduce the energy transported by the sunlight into the biosphere, it is easy to figure out the importance of this process for life on Earth, (see for example Singhal et al. 1999, or Blankenship, 2002). Photosynthetic organisms use electromagnetic energy to drive the synthesis of organic compounds in which the radiant energy is transformed into chemical bound energy. During the photosynthetic process, the molecular oxygen necessary for the survival of oxygen consuming organisms is released in the atmosphere, while carbon dioxide used to synthesize carbohydrates is removed from the atmosphere. The biochemical production of carbohydrate from CO_2 and H_2O is a reduction reaction based on the rearrangement of covalent bonds between carbon, hydrogen and oxygen. Glucose ($C_6H_{12}O_6$) is a six carbon sugar, one of the most frequently found as intermediate product, therefore the equation for photosynthesis is often described as:

$$6CO_2 + 12H_2O + \text{electromagnetic energy} \rightarrow C_6H_{12}O_6 + 6H_2O + 6O_2 \qquad (4.1.5)$$

the free energy required for the reduction of one mole of CO_2 to the energetic level of glucose is +478 kJ/mol so its synthesis requires therefore +2.870 kJ/mol (Singhal et al 1999; Blankenship, 2002). The overall formula is misleadingly simple. In fact, to carry out the carbohydrate synthesis a complex set of physical and chemical reactions is required: to produce a sugar molecule such as

sucrose, the coordinate work of almost 30 different proteins must occur. The energy used for the survival of life on earth is stored in ready-to-use stable compounds able to last for a long time: the fossil fuels currently being burned to provide energy for human activity were synthesized hundred millions of years ago. CO_2 by animal, plant and microbial metabolism, and by biomass combustion represent the reduced carbon returned to the atmosphere. The process by which the carbon returns to the atmosphere is an oxidation reaction between the carbohydrates and molecular oxygen. This oxidation, when driven by metabolic reaction of living organism, is known as *respiration process a*nd is the way how animal, plant and microbial obtain the energy to carry out all the biological process. If the generic carbohydrate is indicated as (CH_2O) the reaction can be described by the formula

$$(CH_2O) + O_2 \rightarrow CO_2 + 2H_2O + \text{Energy} \qquad (4.1.6)$$

For an ecosystem the coupled processes of photosynthesis and respiration can be described by the overall formula:

$$6CO_2 + 12H_2O + \text{electromagnetic energy} \Leftrightarrow (C_6H_{12}O_6) + 6H_2O + O_2 \qquad (4.1.7)$$

LIGHT REACTIONS ⇨ ⇔ ⇦ DARK REACTIONS

These reactions represent the main mechanism by which the energy coming from the Sun is introduced into the biome, and every model includes the simulation of these processes.

5 Materials

5.1 ACASA model

The University of California, Davis, Advanced Canopy-Atmosphere-Soil Algorithm (ACASA) (Meyers 1985; Meyers and Paw U 1986; Pyles et al., 2000, 2003) is a SVAT model of the last generation that simulates the turbulent fluxes in a vertically-layered profile relative to a single point. It is classified as multi-layer model: a multi-layer model divides the canopy and soil into a large number of layers in order to produce information about the vertical profile of the meteorological variables and turbulent flows. In this investigation ACASA was configured with ten layers for the canopy, ten layers above-canopy and ten for the soil. As explained in chapter 3.1, the Navier-Stokes equation set for the planetary boundary layer is not a closed set. Therefore, it is necessary to define additional relationships between the eddy variables and the mean variables in order to close the system of equations of turbulence and allow for a solution. To accomplish the goal the ACASA model uses differential equations of the third order, based on a diabatic theoretical approach developed by Meyers and Paw U (Meyers and Paw U, 1986),(Meyers and Paw U, 1987) that parameterize 4^{th}-order interactions as quasi-Gaussian produces of 2^{nd}-order quantities. Thus the model is classified as "Higher-Order-Closure" turbulence model.

The model therefore simulates second-order turbulent fluxes inside the canopy as independent variables. At the core of the heat, moisture, CO_2, and momentum simulated fluxes are calculations

of an array of different surface temperatures arising within the canopy subscale regime. These latter, calculated using the 4^{th}-order relationship developed by Paw U and Gao (1988), is able to consider large deviations from the air temperature following the same diabatic approach used in the turbulence closure. Responses of physiological processes for different micrometeorological conditions are estimated considering the Ball-Berry stomatal conductance (Leuning, 1990; Collaz et al, 1991). The Farquhar and von Caemmerer photosynthesis equations (Farquhar, et al., 1982) are used to estimate carbon dioxide emissions following an approach suggested by Su (1996). The soil module calculates heat storage processes, values of temperature, evaporation and moisture by adapting the soil and snowpack thermal and hydrological diffusion equations of the Mesoscale Analysis and Prediction System (MAPS) (Smirnova et al., 1997, 2000). The original MAPS subroutines have been generalized in order to deal with large stems, trunks, building walls and soil considering a different diffusion constant for each of these materials; another modification has introduced the ability to handle thermal exchanges over multiple snow layers. The main architectural advantage that ACASA provides to the MAPS framework of soil and snow calculations is the simulations of soil and snowpack dynamics as occurring within forest and urban canopies, in contrast to the one-surface, "bulk" metaphor that is invoked for lower-order schemes.

Another important issue is that in a sensitivity analysis of the model the most crucial parameters related to the simulated CO_2 exchange are the Leaf Area Index (LAI) and the maximum ideal carboxylation rate (VCMAX) (Staudt K. et al., 2010). These adjustable quantities, both of which can be measured, are fundamental to the model's calculations of carbon, water, and heat exchanges.

The model is being continuously improved upon: removal of typographical errors bugs and/or contradictory numerical conceptualizations found in the code often lead to improvements in the results.

The equations, that clearly do not have analytical solutions, are computationally solved by the method of finite differences and recursive iteration.

Creating maps at large scale for the output variable has naturally evolved by coupling the ACASA

model with a limited-area Atmospheric Circulation Model with mesoscale resolution. The Atmospheric Circulation Model selected for this work is the Weather Research and Forecasting (WRF) model.

5.2 WRF model

Weather Research and Forecasting (WRF) is currently one of the most advanced and widely-used numerical mesoscale weather models, with applications ranging from pure research to operational weather forecast. Developed in the United States mainly by the National Center for Atmospheric Research (NCAR) and the National Oceanic and Atmospheric Administration (NOAA), WRF simulates both real and ideal configuration scenarios through a simple data assimilation protocol. The resolution can vary between hundreds of kilometers to the theoretical length of about one meter.

WRF is an open-source software package, version of the source code is available on-line at http://www.mmm.ucar.edu/wrf/users/download/get_source.html. To obtain an executable file ready to be installed the source code (nothing more than a simple algorithmic text file) should be compiled. This procedure is often erratic as a result of the code and the compiler having different answers depending on the type of machine and operating system used. There are some general instructions for compiling the code on different platforms provided by WRF user-support and FAQ literature, but the process should be tailored to the characteristic of the calculus structure. The code is written mostly in FORTRAN90 programming language and is supported for different operating systems such as Darwin, AIX, and others. Linux, the open source operating system derived from the UNIX operating system, is mainly used to provide the background environment to run the software. The convenient and widely-recognized Net-CDF data storage-retrieval software is used both by WRF for output and by the WRF Pre-Processing-System for the treatment of the initial data. This

operation consists of three phases.

- the morphological data are processed for the selected spatial-temporal domain.
- the meteorological data are processed fort the selected period of simulation.
- the meteorological and morphological data are merged into a single file.

Following the completion of the previous steps, the dynamic core elaborations can be performed. This dynamical solution is also executed in multiple phases.

- the preparation of the initial and boundary conditions for the differential equation.
- the actual processing.

There are two types of the dynamic core: a Nonhydrostatic-Mesoscale Model, mainly oriented to weather forecast, and the Advanced-Research-WRF (ARW), which is able to analyze idealized situations. The output data comes in a standard NetCDF format that can be handled for example by the graphics software NCAR-Graphics-Command-Language (NCL), Panoply or Ncview. This software architectural framework depends on dozens of other software (including libpng, pkg-config, fontconfig, freetype, pixman, expat, cairo, jasper, g2clib, g2lib, HDF-5, HDF4) as well as Net-CDF which, in turn, depends on 5 other packages (HDF-5, UDUNITS-2, libcurl, zlib, szlib). The complete set of software packages is open-source and, thus, available for free, but they must be compiled and installed, requiring intimate knowledge of the nuances of various supercomputer systems. NCL provides the maps and the final images in jpeg or png format.

The dynamic core fundamentally solves the equations of Navier-Stokes with the finite difference method. It works together with a number of other subprograms that are nested in this general frame: they exploit a first output provided by the dynamic core, processing a portion of the output already obtained. The outputs of the latter are in turn re-used by the dynamic core to obtain the final solutions. WRF provides a wide choice of these subroutines, which are listed in the manual as "physics options". These physics options are grouped into five categories: “Microphysics” analyzes the processes of precipitation; “cumulus-parametrization” characterizes the vertical cloud formation; planetary-boundary-layer calculates turbulent flux, friction velocity and heat transfer

coefficients; “radiation” considers the radiative processes; the “land-surface-models” containing the multi-layer SVAT models already described.

WRF does not have a graphical interface and every order must be executed through the command line, making the approach not exactly user-friendly.

5.3 WRF-ACASA coupling

The two models are coupled using the meteorological data and morphological parameters provided by WRF (version 3.1) to initialize and drive the ACASA model (Falk et al. 2010). The ACASA model feeds back to WRF the part of its output array corresponding to those variables required by WRF. Coupling the two models is realized exploiting the structure of the “physics option” NOAHLSM, as the land-surface-model NOAHLSM is the most similar to the ACASA scheme in terms of the input data arrays, therefore code implementation was more straightforward. Unlike ACASA, NOAHLSM it is not a “higher order closure model” and is not able to predict the carbon dioxide emission or turbulent fluxes inside the canopy.

The required meteorological input data are the same needed as those in an in-situ ACASA simulation: above-canopy values of air temperature, pressure, wind speed, precipitation rate and phase, long wave radiation flux density (Near-Infrared-Radiation and Thermal-Infrared-Radiation), short wave radiation flux density (Photosynthetic-Active-Radiation) and CO2 concentration (assumed constant at 392 ppm in 2009). Except for CO2, these variables are the same of the lowest level of the WRF-terrain-following pressure vertical coordinate. Those variable values are supplied to ACASA for each model’s time interval at each surface point.

The morphological parameters are necessary to characterize each single point of the domain and are directly or indirectly supplied by WRF structure.

In ACASA many of the adjustable parameters produced little sensitivity in the model output (Staudt et al. 2010), and to facilitate coupling with WRF, only the most sensitive morphological parameters are adjusted between points. Fortunately, these do not exceed in number the amount of morphological parameters required by NOAHLSM.

The directly supplied morphological parameters are latitude, land use type (in the 33 United-States-Geological-Survey classification), soil type (in the 16 United-States-Department-Agriculture classification), urbanized human population density, and Leaf Area Index. The first four are static data while LAI is provided by WRF as monthly value for each land use type accordingly to the United-States-Geological-Survey parameterization. Based on the land use type a group of inner ACASA parameters are indirectly associated at each single point that will represent a pixel in the map. They are canopy architecture (the leaf vertical density distribution, important to calculate fluxes inside the canopy), mean leaf/canopy element drag coefficient, canopy height in urban-buildings, a series of optical parameters and VCMAX at 25°C. VCMAX parameterization is basically achieved according to the NCAR Community Land Model 4.0 (Lamarque et al., 2010). Initial soil temperature and moisture come with the initial condition of the meteorological input data.

A set of ACASA output variables are fed back to WRF and are dynamically exploited by the GCM; they are: sensible heat flux density, water vapor flux density, friction velocity, surface (skin) temperature, specific humidity, shortwave albedo, thermal emissivity and total turbulence kinetic energy.

6 Methods

6.1 Recent ACASA code modifications

To improve the performance of the ACASA model, new features were inserted in the software since its inception. In this section the main three meliorations involving the code are illustrated.

The first modification concerns the addition of a soil module able to evaluate the snow precipitation and accumulation together with the evolution of the snowpack deeps and its melt. The new routine is based on the NOAHLSM thermal and hydrological exchange scheme (Livneh et al., 2010) in which 10 soil and 10 sub-canopy snow layers are considered.

A second subroutine was added in order to prevent anomalous variability of soil variables. A preliminary test showed some anomalies related to the default soil input data prepared by WRF for the diffusion equation. This data set, structured in four levels, introduces some instability in the vertical profiles and in the horizontal variability of soil moisture and temperature. The problem was essentially due to the small number of soil data layers, allowing for few discretization errors arising in conditions of large thermal and hydrological gradients near the soil/snow surface. To create the best work conditions for the diffusion equation, the new subroutine interpolates the default values provided by the WRF framework creating a 10 layers input.

The third melioration of the code concerns with a more representative way to calculate the emission of carbon dioxide in urban environment. In the previous version, the CO_2 flux was retrieved considering only the land use categories that WRF ascribes to a single pixel. The land use assignment process is carried out considering the prevalent categories of each single pixel: in this

way the anthropogenic emission of CO_2 is taken into account only if the urban area results prevalent. With respect to the Sardinia's population distribution, at scales ranging from 3 to 10 Km^2, only a handful of "urban" grids carrying anthropogenic CO_2 fluxes would arise. In the general structure of WRF, data from population density and land use type are independently provided, so this information was exploited to obtain a better result. In the new version, the buildings elevation (therefore the urban canopy height), and the carbon emission rate are now more directly bound to the population density.

The three new features were incorporated into the two WRF files in which the ACASA model is split:

1) module_sf_noahdrv.F
2) module_sf_noahlsm.F.

In addition, four other files were rewritten or partially modified; they contain some routines that allow for dynamical passage of data exchanged between WRF and ACASA, and contain the driving variables needed for ACASA:

1) WRFV3/phys/module_sf_surface_driver.F
2) WRFV3/phys/module_sf_radiation_driver.F
3) WRFV3/din_em/module_first_rk_step_part1.F
4) WRFV3/din_em/module_first_rk_step_part2.F.

The first part of the code involving the dynamic solver of the Navier-Stokes equations lies in the last two files, while in the first two files lies the parts of the code involving the surface and radiation processes needed to close the Navier-Stokes set. Therefore the subroutines contained in the first two files are called by the routines enclosed in the last two files.

Finally, the two registry files were modified to introduce the new variables "*snow", "snowh", "snowc",* (the snow mass for square meter, the snow height, and the snow cover, respectively) in the final output:

1) WRFV3/Registry/Registry.EM

2) WRFV3/Registry/registry.dimspec.

The software was installed both on a server provided with a 16 core Intel processor and 256GB of RAM, and on a laptop of the latest generation equipped with an Intel i7 processor and 10GB of RAM. The possibility of driving short simulations on a machine equipped with graphic interface provides a quicker and more direct instrument to check the set up of the involved domains. Moreover, the software was tested on both the latest Intel and PGI compilers to assure a greater code stability and portability between future users.

6.2 Experimental set up

Once system architectural and software issues were resolved, the attention was turned to the simulation phase. As declared in the second chapter, the main objective of this work concerns with providing a map of carbon exchange at regional scale. The steps of this work can be summarizes as follow:

- evaluate the coupled model WRF-ACASA performance in a single point of the domain, by using Eddy Covariance measured data
- formulate the hypothesis under which a single point validation can provide a reliable methodological framework useful to produce maps of carbon fluxes at regional scale
- create the carbon flux maps for the Mediterranean island of Sardinia.

The location of the island, in force of its typical climate, provides the possibility to fill a knowledge gap concerning with CO_2 emission for the Mediterranean climate regions; for the same reason, it represents an important new test case for WRF-ACASA model. It was selected the spring month of May because during this time plants show a peak photosynthetic activity and physiological process

control, while the soil water content is high enough to have a limited water stress conditions. The single test point is located in a grape vineyard ecosystem in the south of Sardinia.

6.2.1 Climate and morphological description of Sardinia

The climate of Sardinia is characterized by mild and relatively wet winters, while summers are dry and warm. It is classified as Internal Mediterranean climate and can be considered as a transition zone between the tropical climate zones, where the seasons are defined according to the amount of rain, and the temperate climate zones, where the seasons are characterized by temperature changes. Consequently, it involves large inter seasonal variations in temperature and precipitation without reaching the typical extreme values of the two climatic areas (Critchfield, 1983; Martyn, 1992). The main cause of significant climatic seasonal differences is the migration of the high-pressure cells northern boundary which characterizes the adjacent subtropical regions (Peixoto, 1992). From a general circulation point of view, this migration can be considered as a consequence of the displacement of the Hadley cell. In summer, in fact, subtropical high-pressure cells affect the entire Mediterranean Sea, creating an area of high atmospheric stability. During the months of June, July and August, particularly in the southern part of the island, the atmospheric conditions can be considered typically arid subtropical (Barry and Charney, 1983). This often results in situations of clear sky with elevated maximum temperatures, even if accompanied by a nocturnal thermal excursion of some importance. In winter the same cells remain confined to North Africa and the Mediterranean is exposed to the more humid Atlantic flow or to the cold polar flow. A large part of the cyclonic structures affecting the Sardinia Island is generated in the gulf of Genoa. Cyclogenesis is due to the strong baroclinic gradient between North-Central Europe and the Mediterranean Sea, enhanced by orographic Lee effect observed when an Atlantic disturbance reaches the Alps (Tibaldi

et al., 1990). It is interesting to note how the Mediterranean region has the highest frequency and concentration of cyclogenesis in the world (Landsberg, 1988). Basically, the seasonal contrast reflects the annual change in the energy balance in the atmosphere (Holton, 1992), leading to the presence of two seasons with pronounced periods of transition between winter and summer (March-April), and vice versa (September-October) (Benzi et al., 1997). Another feature of the Mediterranean climate is strongly connected to the location of orographic systems of great extent, as well as the sea itself. The relatively shallow and enclosed sea softens the temperature excess less than the Atlantic and Pacific Oceans do at similar latitudes, and at the same time partly protects from the intense disturbances typical of more baroclinically-exposed areas of the globe located at the same latitudes.

The total surface area of Sardinia is 24082 Km^2, and its mean elevation is 380 m. From the orographic point of view, the island contains 18% flat lands, 67 % hilly lands, and 13% mountain territories, 1.5 % of which is above 1500 m in elevation (Camarda, 1993). The main plain is the Campidano region, which is a long and narrow lowland about 100 Km long and 10-15 Km wide, located in the south-center of the island, and oriented in the direction NNW-SSE (Fig 6.2.1.1). A second smaller flat region, called La Nurra, is located in the north-west of the island and its dimensions are about 20 Km. Mountain over 1000 m, in contrast, are spread all over the territory: Limbara (1362 m) and Marghine-Goceano (1251 m) in the northern part of the island, Sette Fratelli (1115 m), M. Arcosu (1090 m), and M. Linas (1236 m) in the southern part. Anyway, only the central group of mountains can overcome the 1500 m of elevation: Gennargentu reaches 1834 m and it is the only place on the island where, on north-facing slopes, snowpack can last all the winter from the end of November to the end of April.

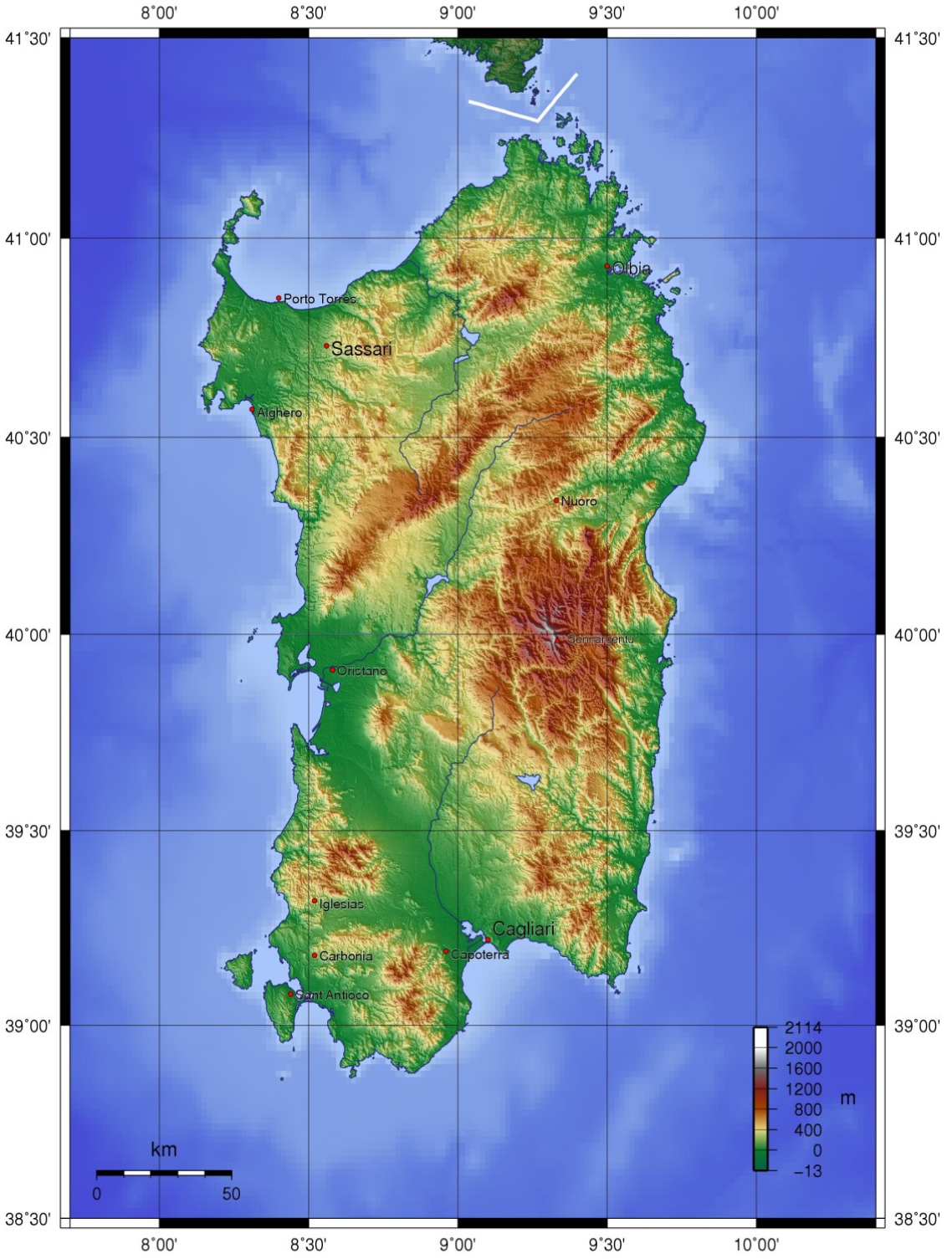

Fig. 6.2.1.1. Sardinia geographic map.

Based on the information provided by the Agenzia Regionale Protezione Ambiente Sardegna (ARPAS), it is possible to give some Sardinian climatological data relatives to the last three decades. Depending on different part of the island, the mean annual maximum temperature ranges

from 16 to 22°C (Fig 6.2.1.2a), while the mean annual minimum ranges from 7 to 14 °C (Fig 6.2.1.2b). During summer, temperatures often exceed 35°C, while in the winter temperatures cool down below 0°C quite frequently: the annual average number of days in which temperature overcome 35°C ranges from 3 to 15, while the average number of frost days ranges from 4 in the coastal areas to 28 in the central part of the island (Fig.6.2.1.3). In August, the mean maximum temperature ranges from 26 to 31°C, while mean minimum ranges from 15 to 21°C (Fig 6.2.1.4). In January, the mean maximum temperature ranges from 7 to 15°C, while mean minimum ranges from 1 to 8°C (Fig 6.2.1.5). Considering wind speed > 8 m/s, dominant directions are west and north-west, while for lower speeds the local orography has a growing importance smoothing the direction's statistical differences.

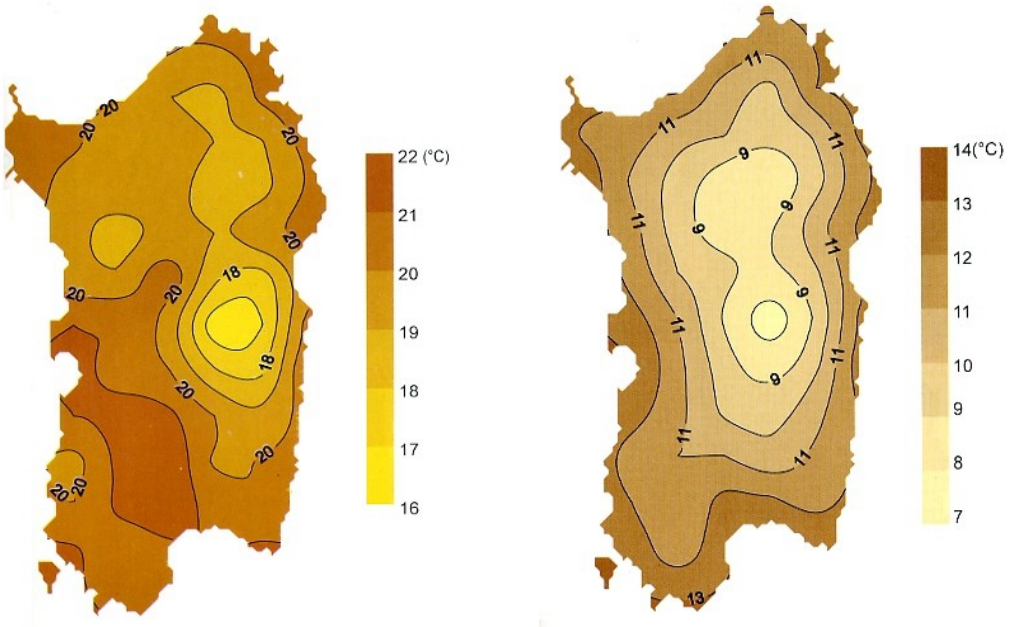

Fig 6.2.1.2. Mean annual maximum temperature (a), and mean annual minimum temperature (b) in Sardinia.

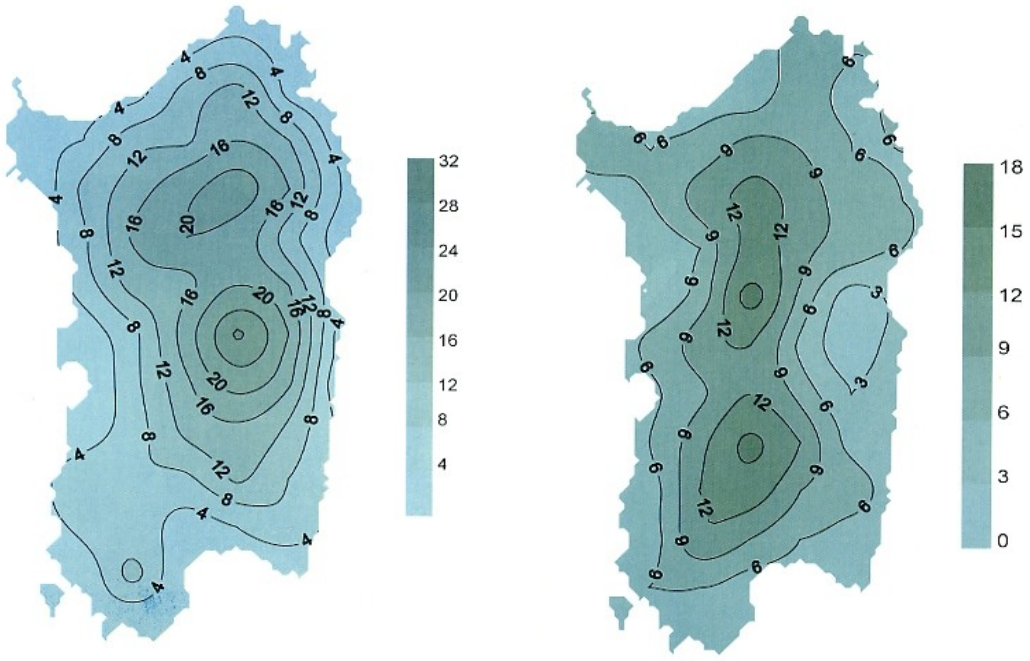

Fig 6.2.1.3 Mean annual number of days with temperature over 35°C (a) and below 0°C (b)

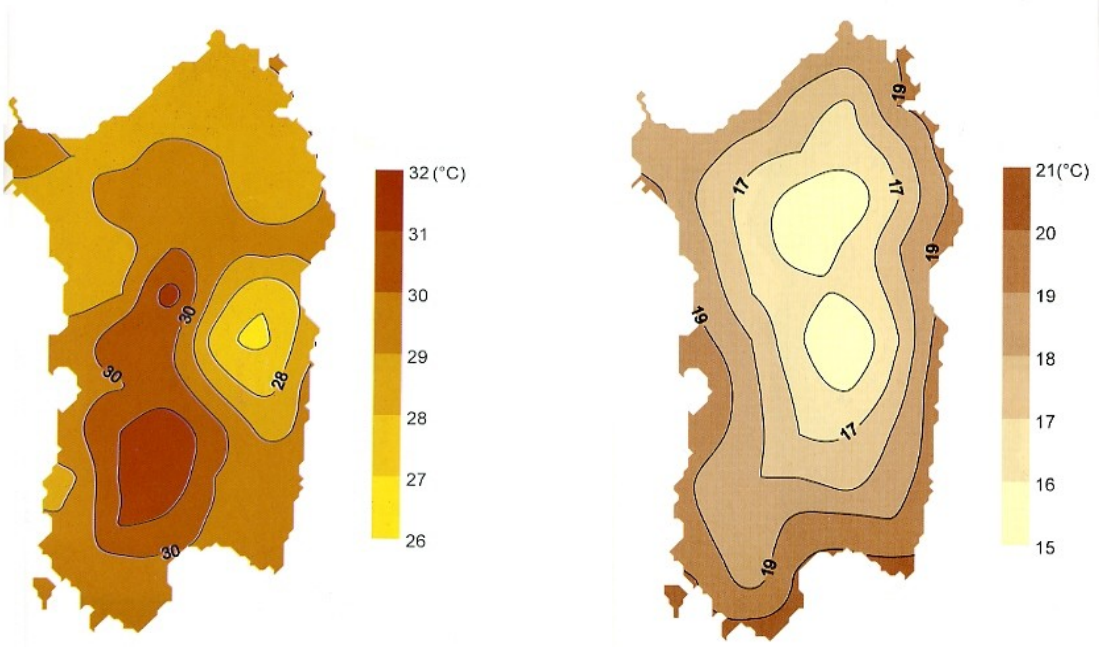

Fig 6.2.1.4. August mean maximum temperature (a) and mean minimum temperature (b)

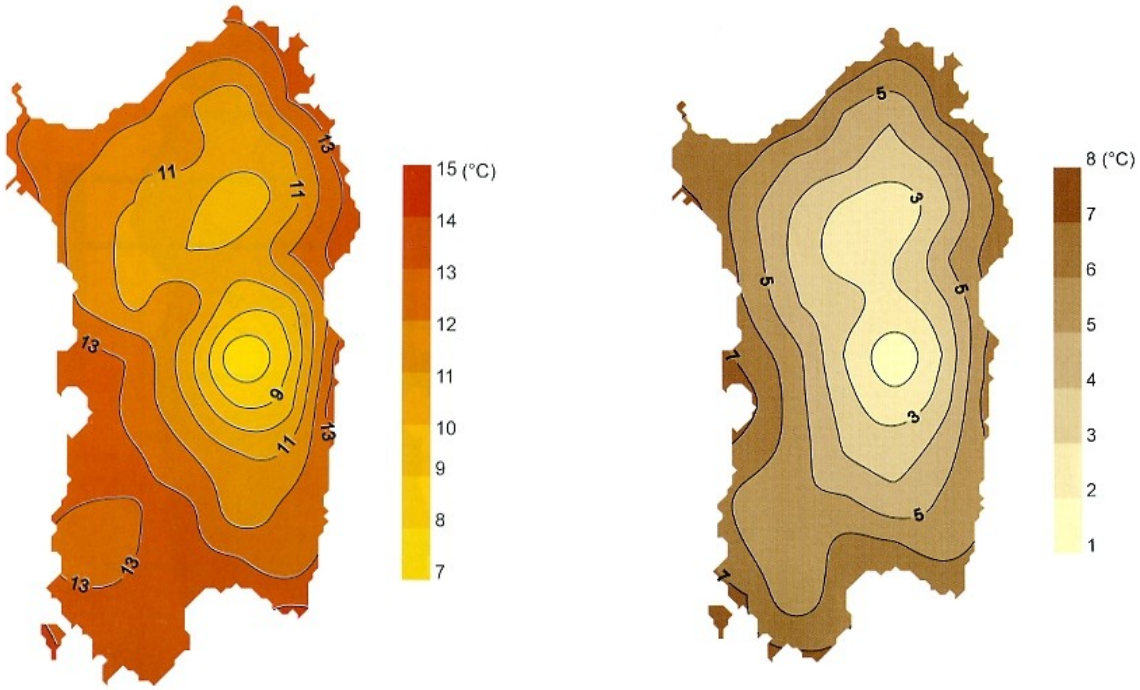

Fig 6.2.1.5 January mean maximum temperature (a) and mean minimum temperature (b).

The natural vegetation is the typical Mediterranean vegetation. Phytoclimatic areas are *Lauretum* and sub hot *Castanetum.* The former ranges from 400-500 m of elevation to 900-1000 m, the latter remains confined to the higher and colder areas of the island. In the *Lauretum* areas, vegetation is mainly represented by Mediterranean maquis species. Maquis can be divided into two types: if the canopy height remains between 2-3 m the dominant species are *Euphorbia, Genisteae, Cistus, Rosmarinus, and Pistacia lentiscus*. While if the canopy reaches 4-5 m the dominant species are *Quercus ilex, Quercus suber, Quercus coccifera, Phillyrea, Arbutus unedo* and *Juniperus*. In favorable conditions this maquis can evolve over time into a real forest, where the dominant species is *Quercus ilex* accompanied and in part replaced by *Quercus suber* in the warmer areas. This kind of forest is largely the most diffused: its coverage is about 15% of the entire island. Above 800 m of elevation, frequency of deciduous species of *Castanetum* is comparable with the evergreen species: in these regions *Quercus pubescens* often replaces *Quercus ile*x that gradually disappears within 1200 m, while the first can survive till 1400 m. In the C*astanetum* areas there are relics of an

ancient flora of the Cenozoic comprising yew, holly, maple trefoil. On the top of the reliefs, between 1000 and 1800 meters, are diffused steppes and scrublands similar to vegetation that in Alpine regions occupies altitudes of 2500-3500 meters. The forest coverage is what remains of the original Biome after an intense deforestation process, which peaked in the second half of the nineteenth century. Nowadays, a severe degradation of large areas exposes the island to desertification risk. The forest coverage has some peculiarities: the Sulcis maquis-forest is considered the largest in Europe, while the Montes Forest is one of the last primary oak forests of the Mediterranean area. Another important part of the landscapes are natural pastures where about 3 million sheep are bred. Natural vegetation covers roughly 1/3 of the entire surface of the island.

Total population of Sardinia is roughly 1.6 million, with a low population density: it does not reach 70 people for Km^2. The only metropolitan area is represented by the territory surrounding Cagliari, the main town of the island. Population of this urban area amount to 450 thousand people and is spread in the 25 central Km of the southern coast. The second town is Sassari with a population of 130 thousand people located in the north-west of the region.

6.2.2 Observed Eddy Covariance data

The experimental site is located within the Company Argiolas Winery near Serdiana, Cagliari, Italy (39°21'43" N, 9°07'26" E, 112 m a.s.l.) as depicted in Fig. 6.2.2.1. The distance between plants of the Vermentino variety grapevines is 0.8 m, while the distance between rows is 2 m. The orientation is in east-west direction and the vegetation is about 2 m tall with roughly 50% ground shading. The soil is mainly composed by clay. A meteorological station was established within the vineyard bound to measure the main meteorological variables, and data were transmitted by remote telecommunication system using a GPRS web protocol.

Fig 6.2.2.1.Location of the meteorological station in Serdiana, Cagliari, Italy.

Fig 6.2.2.2. Eddy Covariance instrumentation (sonic anemometer and infrared gas analyzer).

An Eddy Covariance station was set up to continuously monitor energy and mass fluxes from June 2009. A sonic anemometer (CSAT3, Campbell Scientific, Logan, UT, USA), and an open-path gas

analyzer (Li-7500, Li-cor, Lincoln, NE, USA) were used to measure vertical wind speed, water vapour, and CO_2 concentration (Fig. 6.2.2.2). Eddy covariance data were acquired at 10 Hz and averaged every 30 minutes. Data quality control was performed following the procedures of Baldocchi et al. (1997), Aubinet et al. (2000), Schmid et al. (2000), and Papale et al. (2006).

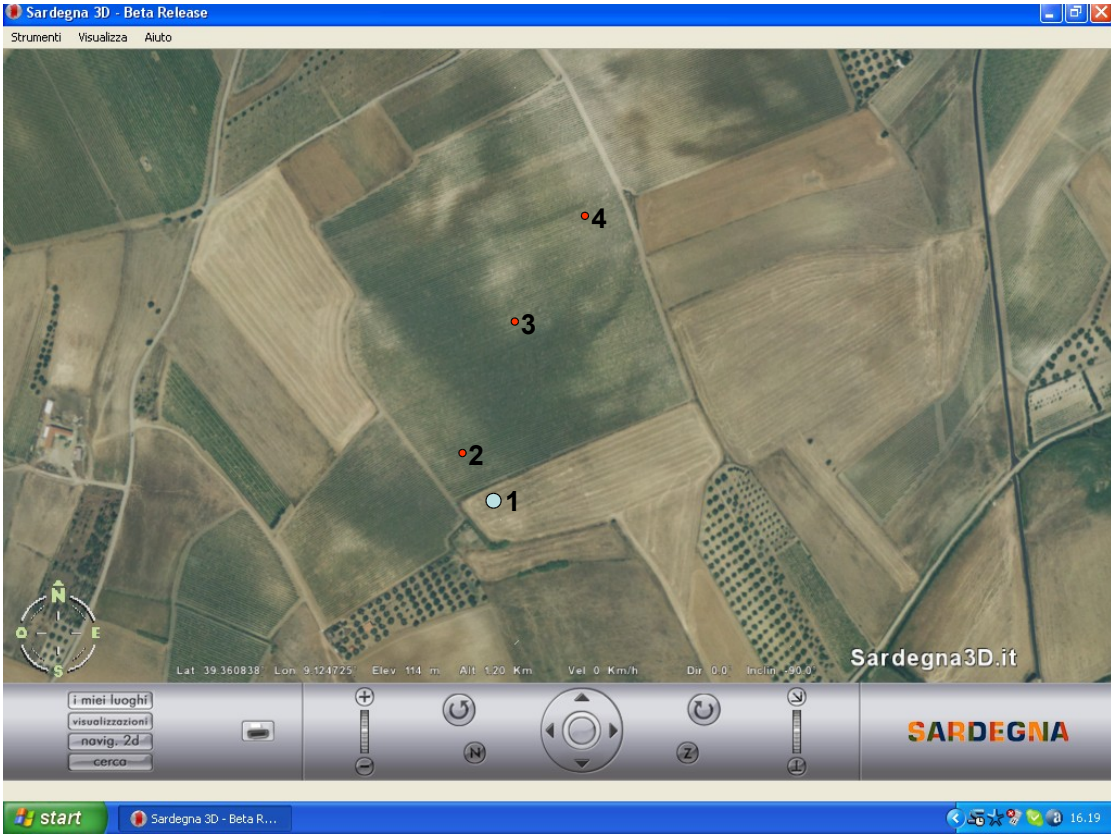

Fig 6.2.2.3. Location of the meteorological tower (point 1). In points 2, 3 and 4 are positioned soil moisture sensors.

Fig 6.2.2.3 shows the exact locations of sensors, which are positioned at 2.8 m from the ground. The difference between the height at which the sensor is placed and the canopy height is 0.8 m, so the fetch of the meteorological station is about 80 m. The distance between point 1 and 2 is less than 70 m so within the fetch boundaries, in the south-south-west direction, can be observed the presence of different vegetation, mainly represented by olive culture. It should be pointed out as this feature could affect measurements when the wind comes from south-south-west direction.

6.2.3 Input data

Meteorological and morphological input data are needed to run the WRF-ACASA model.

Meteorological reanalysis data, from the European Centre for Medium-range Weather Forecast (ECMWF), were used to initialize the coupled WRF-ACASA model. The ECMWF ERA-Interim reanalysis data are provided with resolution of 0.7 ° (77 Km) with 38 vertical levels distributed from sea level up to an altitude of 80 Km. (http://www.ecmwf.int/research/era/do/get/era-interim).

With respect to the morphological data, it is possible to note as the default land use maps provided by WRF are not very accurate. This inaccuracy propagates in all the simulations steps deeply affecting results, since the land use categories are the backbone of the morphological parameterization. To deal with a better morphological description of the region, a land-use map derived directly from those provided by the European Environment Agency was introduced in the WRF-ACASA framework. The Corine data set (http://www.eea.europa.eu/data-and-aps/data/corine-land-cover-2006-raster-2) comes with a 100 m resolution and divides the territory into 81 land use classes. WRF can manage only 33 land use categories, so it had been carried out a merging class process to adapt the Corine map to the WRF map format. During the merging process, quite different land use types were sometime grouped into the same categories. In Tab. 6.2.3.1 the details of the merging process are shown while meliorations in resolution and accuracy can be appreciated considering differences between the map obtained through the Corine (Fig 6.2.3.1) and the WRF default map (Fig. 6.2.3.2). Problems related to this mandatory choice will be discussed in the next section.

Table 6.2.3.1 Land use classes and detail on the merging class process.

Corine land use description	Area Surface in Km^2	WRF-USGS Code
Natural pastures	1447,765	2 Dryland Cropland and Pasture
Non-irrigated arable croplands	2511,729	2 Dryland Cropland and Pasture
Vineyards	246,857	2 Dryland Cropland and Pasture
Greenhouse croplands	17,69	3 Irrigated Cropland and Pasture
Orchards and berry plantations	119,074	3 Irrigated Cropland and Pasture
Simple crops and horticultural crop fields	2057,290	3 Irrigated Cropland and Pasture
Complex cultivation patterns	422,047	3 Irrigated Cropland and Pasture
Rice fields	46,605	3 Irrigated Cropland and Pasture
Annual crops associated with permanent crops	1,332	4 Mixed Dryland/Irrigated Cropland and Pasture
Annual crops associated with other permanent crops	579,322	4 Mixed Dryland/Irrigated Cropland and Pasture
Annual crops associated with vineyards	2,961	4 Mixed Dryland/Irrigated Cropland and Pasture
Lands principally occupied by agriculture, with significant areas of natural vegetation	292,810	5 Cropland/Grassland Mosaic
Artificial grasslands	1645,698	5 Cropland/Grassland Mosaic
Agro-forestry areas	574,277	6 Cropland/Woodland Mosaic
Natural grasslands	103,157	7 Grassland
Artificial recolonization areas	489,379	8 Shrubland
Bush riverbank vegetation areas	49,164	8 Shrubland
Annual croplands associated with Olive	117,142	8 Shrubland
Mediterranean maquis	3408,009	8 Shrubland
Olive groves	487,760	8 Shrubland
Bush and Shrubland	126,906	9 Mixed Shrubland/Grassland
Sparsely vegetated Areas, 5% <coverage <40%	495,685	9 Mixed Shrubland/Grassland
Garigue	200,476	10 Savannah
Arboriculture with broadleaf species	3,156	11 Deciduous Broadleaf Forest
Poplar, willow, eucalyptus mixed forest	191,813	11 Deciduous Broadleaf Forest
Broadleaf forest 20% <coverage <50%	919,954	13 Evergreen Broadleaf Forest
Broadleaf forest 50% <coverage <80%	1307,394	13 Evergreen Broadleaf Forest
Broadleaf forest 80% <coverage	1287,083	13 Evergreen Broadleaf Forest
Cork oak	804	13 Evergreen Broadleaf Forest
Evergreen needleleaf forest 20% <coverage <50%	70,093	14 Evergreen Needleleaf Forest
Evergreen needleleaf forest 50% <coverage <80%	23,855	14 Evergreen Needleleaf Forest
Evergreen needleleaf forest 80% <coverage	110,523	14 Evergreen Needleleaf Forest
Arboriculture with needleleaf species	17,967	14 Evergreen Needleleaf Forest
Needleleaf and broadleaf mixed Forest 20% <coverage <50%	188,569	15 Mixed Forest
Needleleaf and broadleaf mixed Forest 50% <coverage <80%	70,093	15 Mixed Forest
Needleleaf and broadleaf mixed Forest 80% <coverage	110,523	15 Mixed Forest
Urban vegetated areas	4,309	15 Mixed Forest
Marine natural fish farming	0,326	16 Water Bodies
Sea	0,105	16 Water Bodies
Intertidal areas	0,989	16 Water Bodies
Inland wetlands	13,592	17 Herbaceous Wetland
Natural recolonization areas	437,516	19 Barren or Sparsely Vegetated
Airports and heliports	10,559	26 Lava
Mines sites	66,711	26 Lava

Rock wall and cliff	62,197	26 Lava
Beaches with dimension larger than 25 m	16,807	27 White Sand
Beaches dunes and sand	0,067	27 White Sand
Vegetated dunes with dimension larger than 25 m	11,538	27 White Sand
Non vegetated dunes with dimension larger than 25 m	2,638	27 White Sand
coastal lagoon fish farming	3,847	28 Inland Water Bodies
Sea fish farming	0,025	28 Inland Water Bodies
Artificial lakes	101,432	28 Inland Water Bodies
Natural lakes	5,771	28 Inland Water Bodies
Channels and waterways	1,003	28 Inland Water Bodies
Rivers and creeks	5,968	28 Inland Water Bodies
Lagoons, lakes and coastal ponds	0,526	28 Inland Water Bodies
Lagoons, lakes and coastal ponds with natural fish production	72,281	28 Inland Water Bodies
Creek beds larger than 25 m	8,086	28 Inland Water Bodies
Estuaries and deltas	0,531	28 Inland Water Bodies
Salines	36,583	28 Inland Water Bodies
Salt marches	41,021	28 Inland Water Bodies
Other	1,201	30 Unassigned
Archaeological areas	1,103	30 Unassigned
Construction sites	26,762	30 Unassigned
Cemeteries	2,603	30 Unassigned
Scrap and Car dump	0,898	30 Unassigned
landfill site	2,810	30 Unassigned
landfill site and Scrap dump	0,035	30 Unassigned
Sport and recreational areas	29,970	31 Low Intensity residential
Continuous low intensity residential fabric	156,097	31 Low Intensity residential
Discontinuous low intensity residential fabric	88,707	31 Low Intensity residential
Rural buildings	93,436	31 Low Intensity residential
High Intensity residential areas	160,353	32 High Intensity residential
Port areas	7,523	33 Commercial/Industrial/Transportation
Important commercial unit	1,004	33 Commercial/Industrial/Transportation
Facilities related to commercial network	2,794	33 Commercial/Industrial/Transportation
Industrial commercial units and associated lands	96,363	33 Commercial/Industrial/Transportation
Important facilities and services units	10,922	33 Commercial/Industrial/Transportation
Road networks and associated lands	2,427	33 Commercial/Industrial/Transportation
Rail networks and associated lands	13,347	33 Commercial/Industrial/Transportation

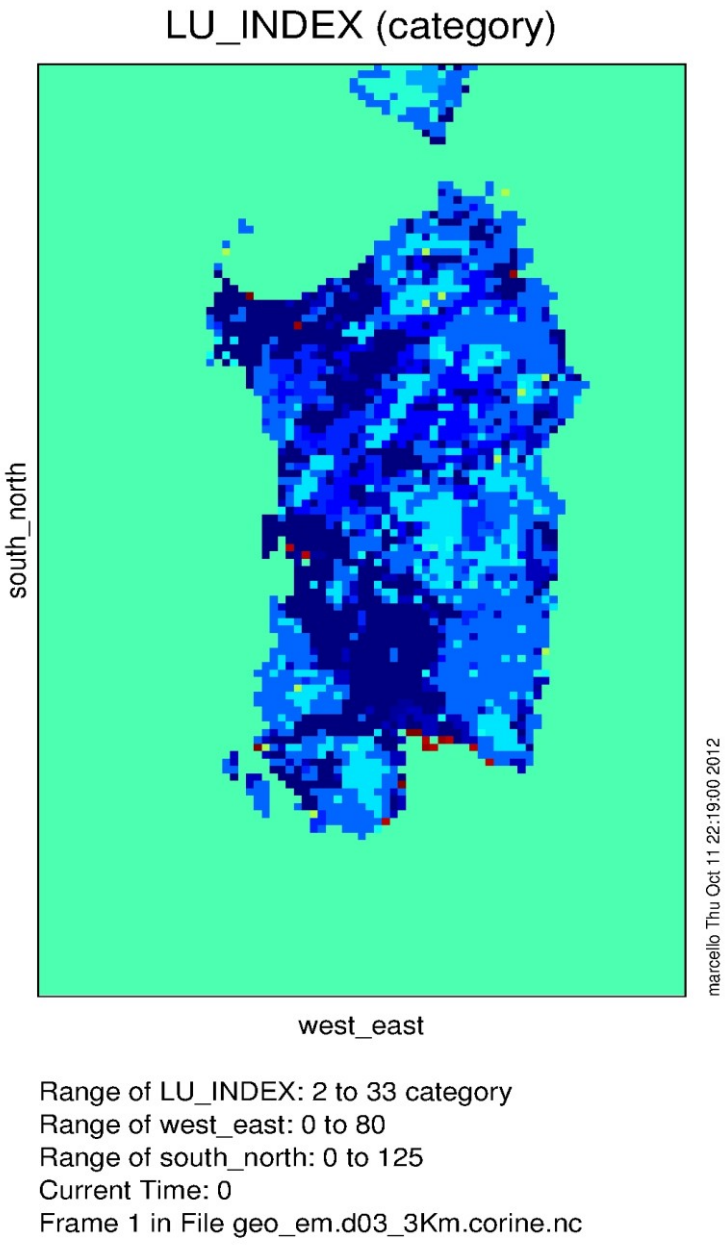

Fig.6.2.3.1. Land use classification of Sardinia based on the Corine data. It is possible observe a better resolution and the red point representing the urban land use located in the correct positions.

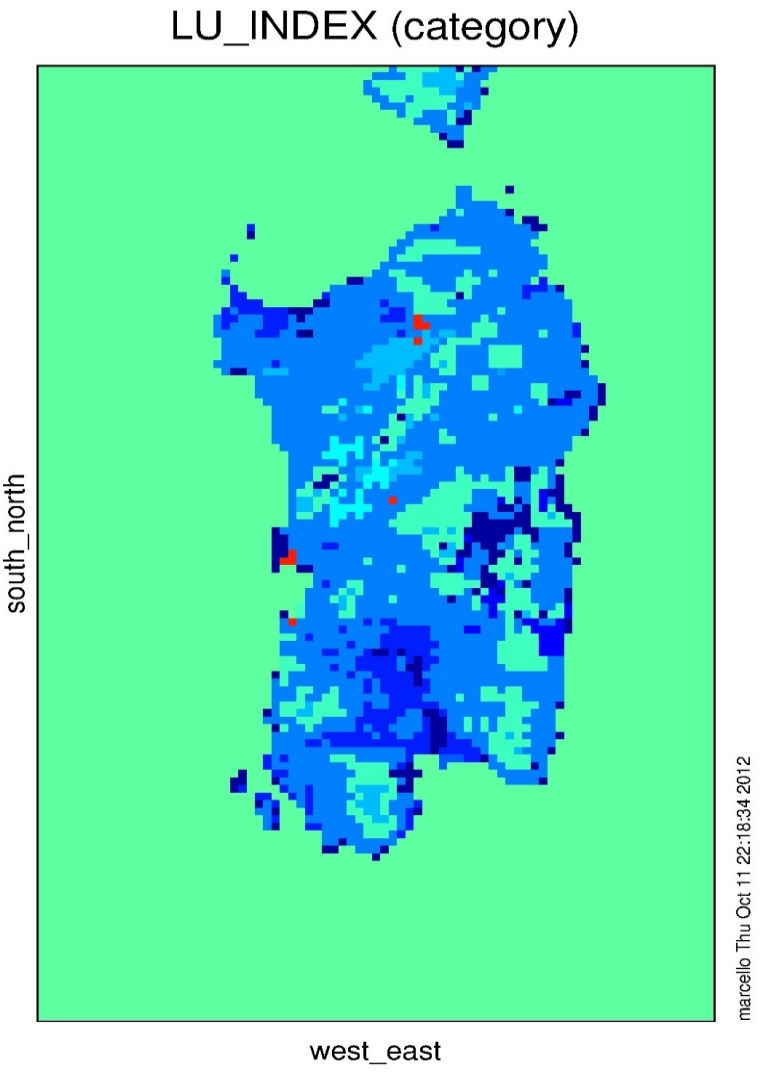

Fig 6.2.3.2. Land use classification of Sardinia based on the default WRF data. It is important to note as the red points representing urban areas are located in the wrong positions.

To transform the original Corine format into one that WRF can ingest, the program utilities read_geogrid and write_geogrid were utilized. They are directly provided with the WRF source code and adjustments were made in the model code to allow for the merging process.

6.2.4 Validation strategy

From a general point of view, the best validation for a simulation map should consider observations coming from sites with different characteristics and environmental conditions per each land use class. In practice, this situation never occurs in reason of a limited monitoring station network. In literature, the problem deriving from the lack of such information is generally overcame considering the following cogent hypothesis: if a map is validated in one point, it does not validate only a single point, but also the straightness of the method that lead to the reasonable result. Based on this assumption, simulations per each point derived with a such validated method can be considered acceptable, even though they are not directly tested (Mayaux et al., 2002; Chena et al. 2002; Miranda et al. 2006). In this study the same hypothesis has been used.

The merging process of the land use classes described in the previous section deeply influenced the remainder of this work, because the heterogeneity within the same categories triggered complications in the validation procedure. Observed data generally refers to a point located in an area with the same vegetation species, or that can be strictly categorized under common characteristics (such as the case of Mediterranean maquis). Available validating data in this work came from a vineyard. In the merging process, the vineyard land use class was coupled together with natural pastures and Non-irrigated arable croplands into the WRF land use category number 2 *Dryland Cropland and Pasture.* In May, the vineyard Leaf Area Index can be estimated around 1.5 (Marras et al., 2008), while for *"dryland cropland and pasture"* it can reach the value of 5 (Mitchellet al., 1998). The CO_2 flux simulated by the ACASA model results almost linear with respect to the LAI (Staudt et al., 2010). A simulation conducted with the WRF default LAI value would provide results that largely overestimate the flux in the vineyard: this discrepancy do not allow for the direct comparison between simulated and observed data.

To overcome this problem, a different approach requiring two different 30-day simulation of the

entire Sardinia was followed. In a first simulation, the significant parameters influencing the carbon flux of all the pixels belonging to land use type number 2 were set to the ones characterizing the vineyard land use class. It was so possible to extract the time series of the pixel where the meteorological station was located, and compare correct LAI value simulated data with observations. In this way, the model was validated for the vineyard land use class. Thus this first run demonstrated the veracity of the single point simulation data.

Then, a second WRF default parameter simulation was conducted: it represents the correct regional map of CO_2 indicated as one of the object of this work. The comparison of the two CO_2 maps (described in detail in the next chapter) shows insignificant differences for the pixels not involved in the changing of the parameters. Therefore, forcing the parameters of the land use category number 2 at the values valid for the vineyard category, can be considered as a small perturbation of the general structure that does not appreciably affect the remaining territory.

Clearly, the times series of the validated point of the first simulation is generated by the entire structure involved: the input data set (meteorological and morphological data), the coupled model WRF-ACASA, and the set up choices. Thus, the general structure itself has reasonably been considered cogent in how it carries on the simulations. Consequently a reliable work hypothesis became possible: if a general structure is coherent with the morphological and meteorological data, and if it produces a simulation that is validated at a single point, (not only the point simulation is considered validated but) all the general framework that produced the results can be considered reliable. Under this hypothesis, the second simulation performed using a set of morphological parameterization that correctly represents all the different land use classes of the territory, is automatically considered validated.

A second issue generated by the merging class process is the introduction of a basic error regardless of the spatial resolution which the model is ran with. As described above, some Sardinian land use classes are not represented in those that WRF can currently manage. This suggests that a higher resolution test does not necessarily beget more accurate results. A greater resolution clearly provides

data that better describe the territory, especially in non-homogeneous areas with respect to topographic and land use data. This increase in horizontal resolution reduces the error that occurs in assigning the land use class and elevation values per each pixel, resulting in more accurate description of the related variable. For example, the driving of CO_2-exchange, via LAI and VCMAX, strictly depends on land use, so it is easy to understand how a more detailed description of the landscape is important for more accurate carbon emission simulations. Higher resolution test effort should counterbalance the improvement in accuracy and precision of the final results. It means that the improvement deriving from a higher resolution simulation should really affect the final results. So it should be of the same (or higher) order magnitude then the error introduced by the merging process. The above lead to the decision to perform initial simulations at 3 Km resolution, and eventually in a second phase only a further downscaling could be performed.

Downscaling is performed with a process called nesting in which a coarse domain, the "parent domain," supplies the initialization data to a finer resolution domain, the "child domain". The ratio between the two resolutions can be different but in the WRF user manual a ratio of one-to-three is suggested as numerically optimal. So, with a single model run it is possible to simulate weather variables on a grid step of 1/3 of the input data step. When performing a nested domain run, it is possible to get 1/9 of the initial step because the output data from the first step are reused to initialize the run on the child domain. Thusly, also for the child domain the output is downscaled to 1/3 with respect to the parent domain. The operation can be repeated until the desired resolution is reached. In this case, three domains and two nesting processes were enough to reach a 3 Km resolution domain (Fig 6.2.4.1). The widest parent domains d01, with a grid resolution of 27 Km, is comprised of 81X125 points and extends for 2187Km X 3375Km. The second domain d02 with a grid resolution of 9 Km, is comprised of 82X127 points and extends for 738KmX1143Km. The last domain d03 with a grid resolution of 3 Km, is comprised of 82X127 points and extends for 246Km X381Km. Sardinia can be inscribed inside a rectangle of dimension 286KmX146Km. The space between the land boundaries and the domain boundaries is needed for the island to be in the

domain's “central part solutions”, which can be considered the most reliable output data zone.

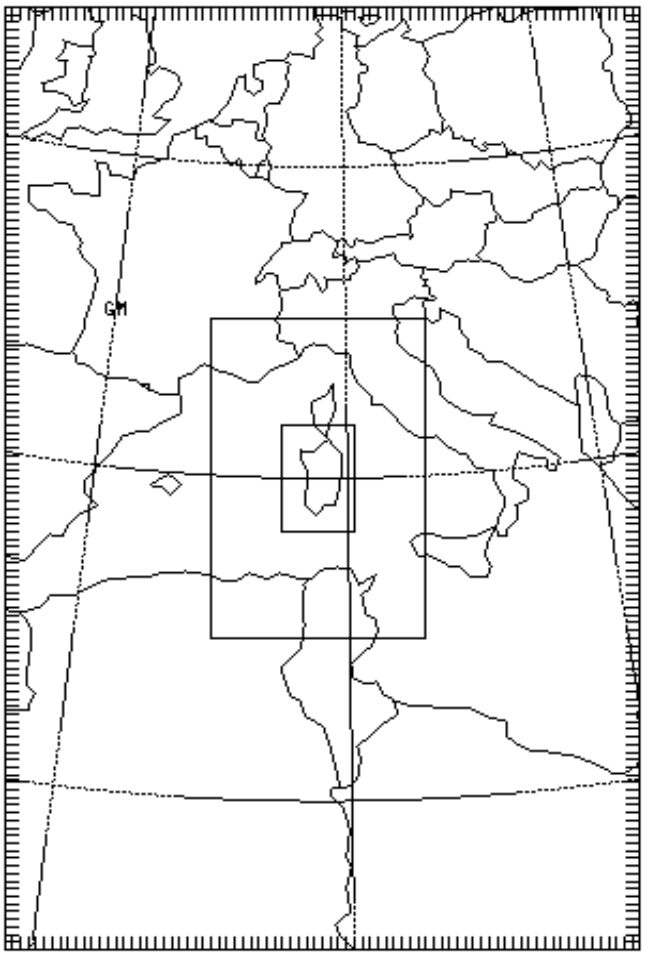

Fig 6.2.4.1 The three telescopic domains inscribing the island of Sardinia.

6.2.5 Model set up and LAI parameterization

For both runs, the one providing the validating time series and the one that gave the final map, the same model set up was used. The New Thompson microphysics scheme was selected for the precipitation process. For long wave and short wave radiative transfer the Rapid Radiative Transfer Model and the Dudhia scheme were used, respectively. For the Surface-Layer–PBL interface, the

Eta similarity scheme was selected. The Mellor-Yamada-Janjic scheme was chosen for the Planetary Boundary layer, while for the cumulus parameterization, the Grell 3d ensemble cumulus scheme was employed. Detail of the physic option can be found in the WRF User Manual (http://www.mmm.ucar.edu/wrf/users/).

As it has been already clarified in the description of the coupling between WRF and ACASA (chap. 5.3), the CLM model (Lamarque et al., 2010) provided the default values of VCMAX. In the case of Mediterranean Sardinia's climate some changes were required by considering values commonly found in the literature. For the land use category number 8, the ones involving mainly Mediterranean maquis, a value of VCMAX of 35 μmol $m^{-2}s^{-1}$, as found in the work of Marras et al. (2011), was selected. In the same effort, the value of 3 for leaf area index for the Mediterranean maquis was found: it was coherent with the default values supplied by WRF-ACASA. For the land use category number 13 (evergreen broad leaf forest), the CLM proposed values seems to be a little high as compared to the values found in *Quercus ilex* and *Quercus suber* specific studies. So a value of 47 μmol $m^{-2}s^{-1}$ (Vaz et al. 2011) was used instead of 72 μmol $m^{-2}s^{-1}$. And for the same land use category also leaf area index seems to be overestimated compared to the work of Sala et al. (1990), so the maximum value of LAI was lowered from 6.7 to 5.8.

Regarding the simulation run that provides the single point validating time series, it should be point out as WRF-ACASA assigned to the meteorological station pixel a default LAI value of 4.7 and a value of 50 μmol $m^{-2}s^{-1}$ for VCMAX. Considering the vineyard, while the value of VCMAX can be considered consistent with what is found in literature, such is not the case with LAI. Marras S. et al. (2008) suggested to use a value of leaf area index between 1.37 and 1.55, and a value of VCMAX that is between 25 μmol/m^2s and 60 μmol/m^2s. All the points with land use type 2 were then set with a LAI value of 1.5. This was achieved after modifying the LAI value for land use class 2 in the file WRF/run/ VEG.TABL. In Fig 6.2.5.1, Fig 6.2.5.2, and Fig 6.2.5.3 are depicted the spatial distribution of LAI with regards to the validation map, the real map, and the land use category map, respectively. The first two images differ only in the pixels with the land use category 2.

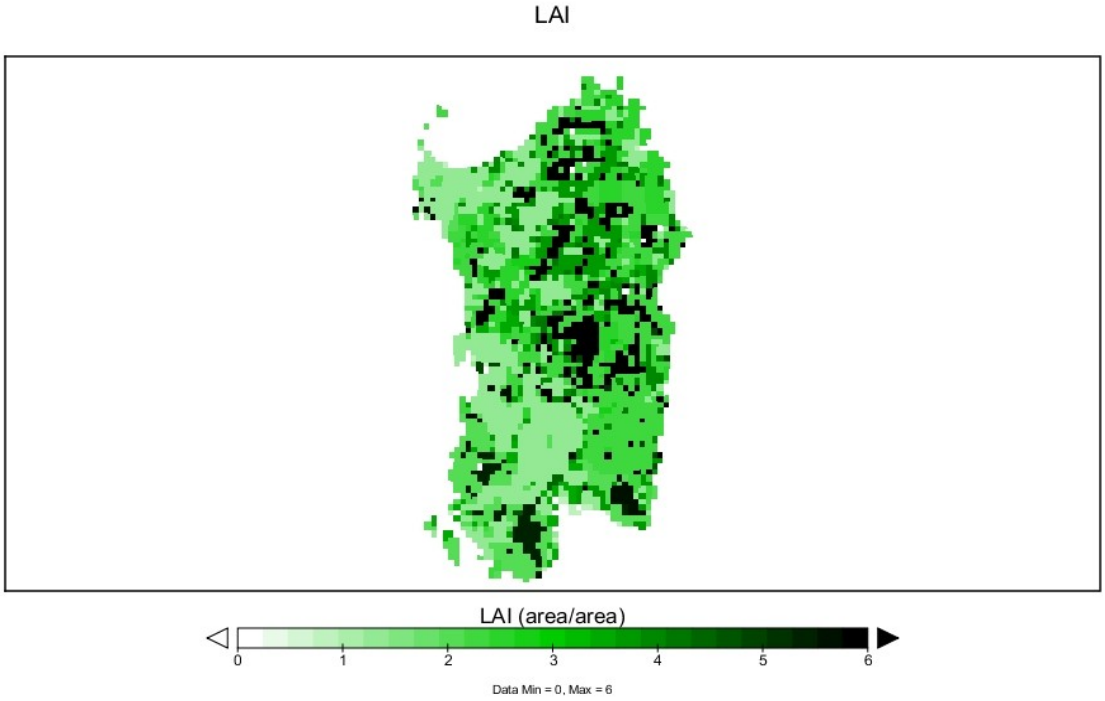

Fig.6.2.5.1. The Leaf Area map of Sardinia used only for the validation process

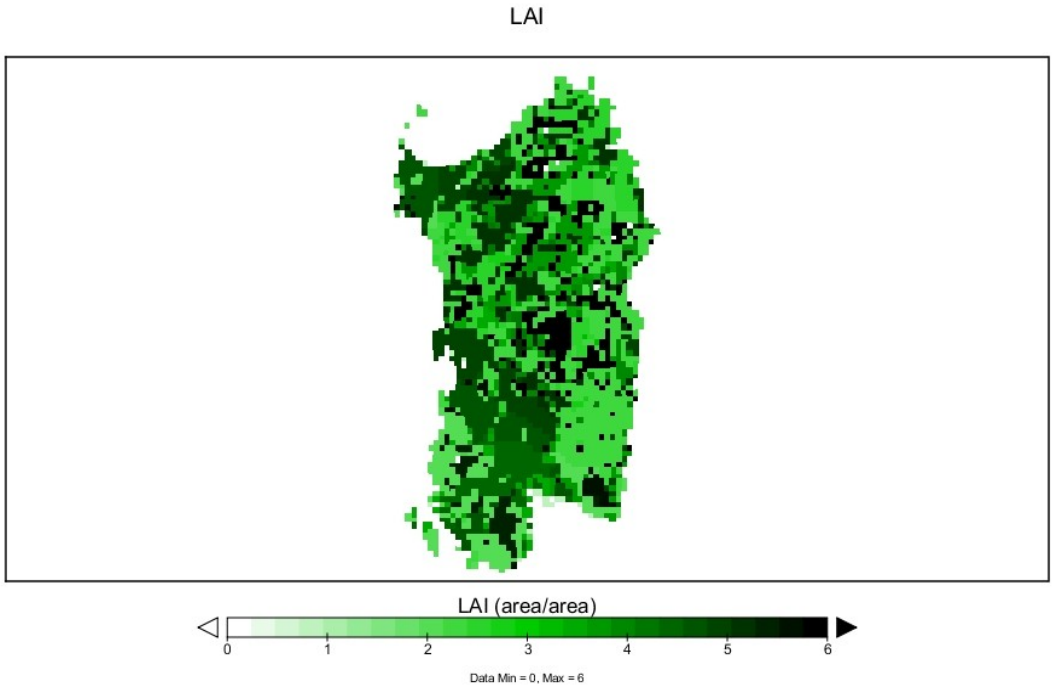

Fig. 6.2.5.2. The Leaf Area Index map of Sardinia used for the simulations

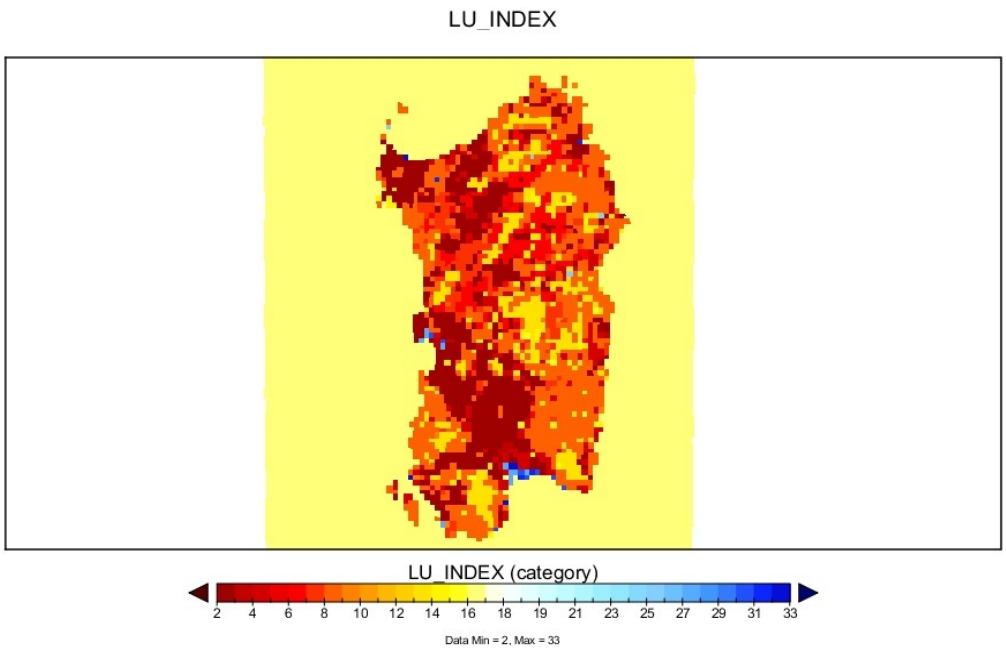

Fig. 6.2.5.3. WRF-ACASA Land use categories map for Sardinia after the merging class process: the dark red pixels represent the land use category number 2.

7 Results

The first section will describe the validation of the coupled model WRF-ACASA for the single point. From a first map simulating the carbon flux of the entire island of Sardinia, the time series of the vineyard validation point was extracted. In this simulation, the WRF default morphological parameters influencing the carbon flux of all the pixels belonging to the land use category number 2 (the category of the validation point), were set to the ones of the vineyard. The validation is accomplished comparing of the simulated and measured Eddy Covariance data. This single point validation represents the first hypothesis allowing for the creation of a reliable carbon flux map of the entire island of Sardinia.

The second section concerns with the methodology of the map validation. In this part, the second hypothesis required for the general framework validation is verified: changing the default parameters for the pixels belonging to land use category number 2 should produce a small perturbation of the general framework not influencing the remaining territory. This is achieved by comparing a second map, obtained with the default morphological parameters, to the previous first map obtained by modifying morphological parameters of the land use category number 2. In this way, it is demonstrated how the new parameters only affected the territory subjected to the parameter modification, while the remaining part of the island is not involved. This second map represents the final validated map.

The third section describes the final validated map as result of the simulations for the entire island of Sardinia.

The software for data analysis was specifically written (FORTRAN 90) for this study. This choice

took longer in the first place, but it provided for a more direct, simpler and faster data analysis over time that will benefit future work. This effort is especially effective for analyzing multiple results from simulations, where repetitive math are performed. A second reason is the common proprietary software limit for handling huge number of data points, such as the amounts involved in the calculus of the total carbon dioxide exchange over the model domain. For each of the 4500 pixels of the rectangle enveloping the island, it was considered a half hourly dataset for 30 days: there are more than 6 million points in the dataset.

7.1 Single point validation

Two sets of analyses were performed for the validation point located nearby Serdiana (Cagliari, Italy) One was conducted considering all the 1440 half-hour data (30-minute mean values of the 10Hz-instantaneously-measured carbon dioxide flux density) for the 30 firsts days of May 2010. For the second analysis, the simulated half-hour data were sorted by time and averaged. In both analyses, the sample of data numbers 30 or greater. Therefore, by way of the central limit theorem, it is reasonable to treat such data distributions as possessing a normal (Gaussian) distribution. Mean and standard deviation were used to assess the variable value and its error, respectively.

7.1.1 All data analysis

Referring to the non-aggregated data, the mean and the standard deviation of the observed and simulated fluxes of carbon dioxide were calculated. All data are listed in Table 7.1.1.1. For both observed and simulated data, it is possible to note the larger value of the standard deviation

compared to its mean. The reason results from the inclusion of diurnal and nocturnal values, often very different from each other, in each set of calculations. The Root Mean Square Error (RMSE) between observed and simulated points seems large when compared with the mean observed value, but it represents less than 12% of the range of variation interval of the mean half-hour observed data. From an average point of view, the model was in good agreement with observations, even if it slightly underestimates the carbon exchange (positive value of Mean Bias Error, MBE). The good model performance is also revealed by a correlation coefficient equal to 0.96; for a sample of 1440 elements the possibility that two not linearly correlated variable (null hypothesis) show a correlation coefficient ≥ 0.96 is $\leq 0.01\%$. This fact, often referred to as P-value ≤ 0.0001, represents an extreme statistical significance.

Table 7.1.1.1. Statistical parameters calculated for half-hourly data set. RMSE = Root Mean Squared error, MAE = Mean Absolute Error, MBE = Mean Bias Error, Coefficient of Correlation (a), and linear regression results (b).

Statistical parameters					
Observation	**Model**	**RMSE**	**MAE**	**MBE**	**Corr. Coeff.**
$\mu molCO_2m^{-2}s^{-1}$	$\mu molCO_2m^{-2}s^{-1}$	$\mu molCO_2m^{-2}s^{-1}$	$\mu molCO_2m^{-2}s^{-1}$	$\mu molCO_2m^{-2}s^{-1}$	
-2.84±4.69	3.25±4.39	1.45	1.19	0.41	0.96

Linear regression			
Slope	**Intercept**	**RMSE**	**R^2**
		$\mu molCO_2m^{-2}s^{-1}$	
0.894±0.007	-0.70±0.04	1.30	0.91

Linear regression analysis was also performed between the two time series of data. The value of the slope of the least squares line, depicted in Fig. 7.1.1, is 0.894±0.007. It means that with the probability of 95%, the slope is between 0.908 and 0.880. The y-intercept value is -0.70±0.04: at 95% it is within the interval -0.78 and -0.62. These two parameters are coherent with the MBE in considering the model slightly underestimating the CO_2 flux. The RMSE between observed data and the regression model data is 1.30 $\mu molCO_2 m^{-2} s^{-1}$. Coherently, it is little lower than the RMSE between observed and simulated data. R^2 is often referred to as the *coefficient of determination* and in a linear regression it is equal to the squared correlation coefficient between the regression predicted values and the observed values. For the Serdiana point simulation, the R^2 calculated value is 0.91. For this quantity, the P-Value is < 0.0001, which is again extremely statistically significant. It is possible interpret the simulated data as saying that the WRF-ACASA model is able to explain more than 90% of the observed data. Figs. 7.1.1.2, 7.1.1.3 and 7.1.1.4 show a graphical comparison between observed and simulated time series.

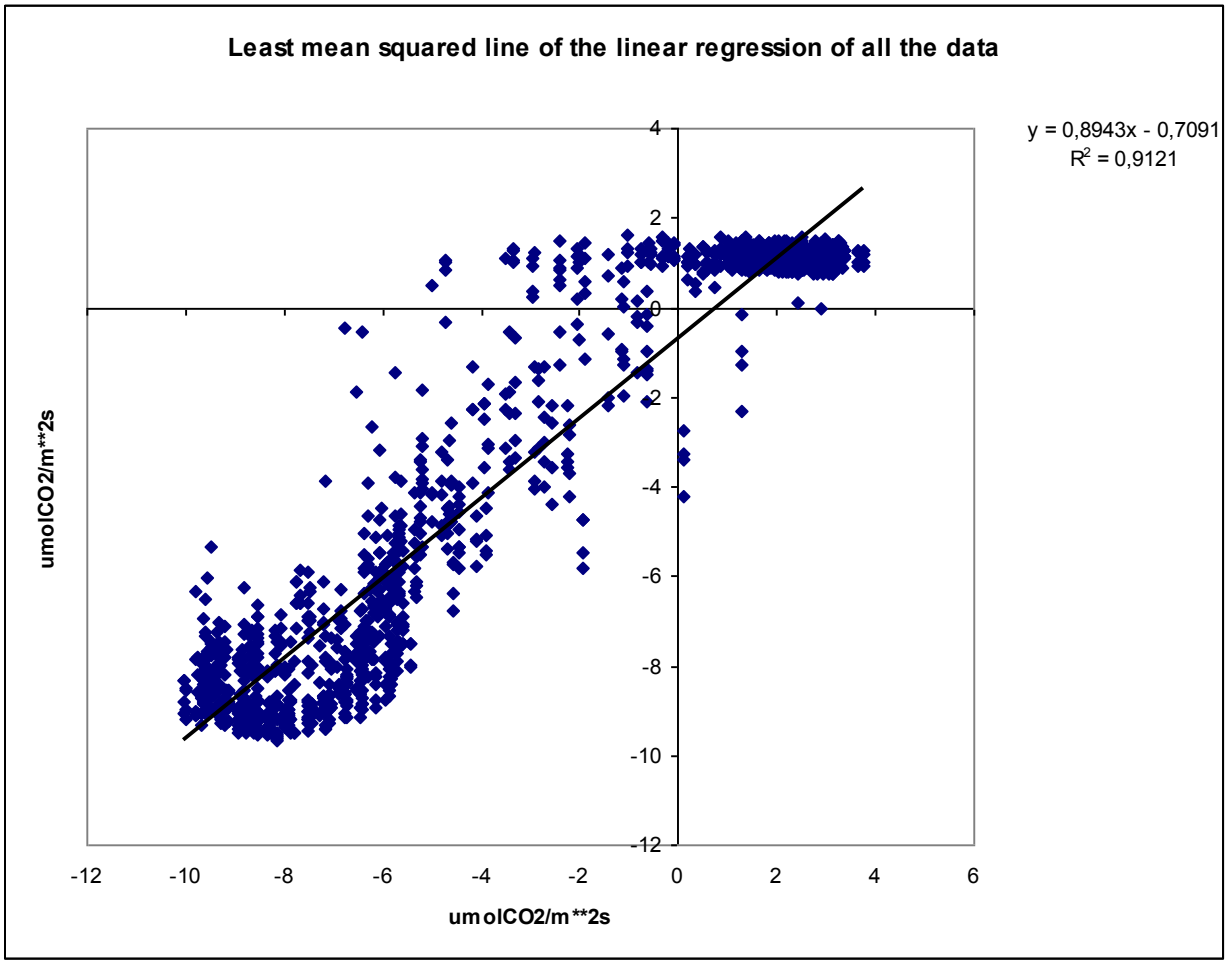

Fig. 7.1.1.1. The least mean squared line of the linear regression between simulated (y-axis) and observed (x-axis) half-hour data.

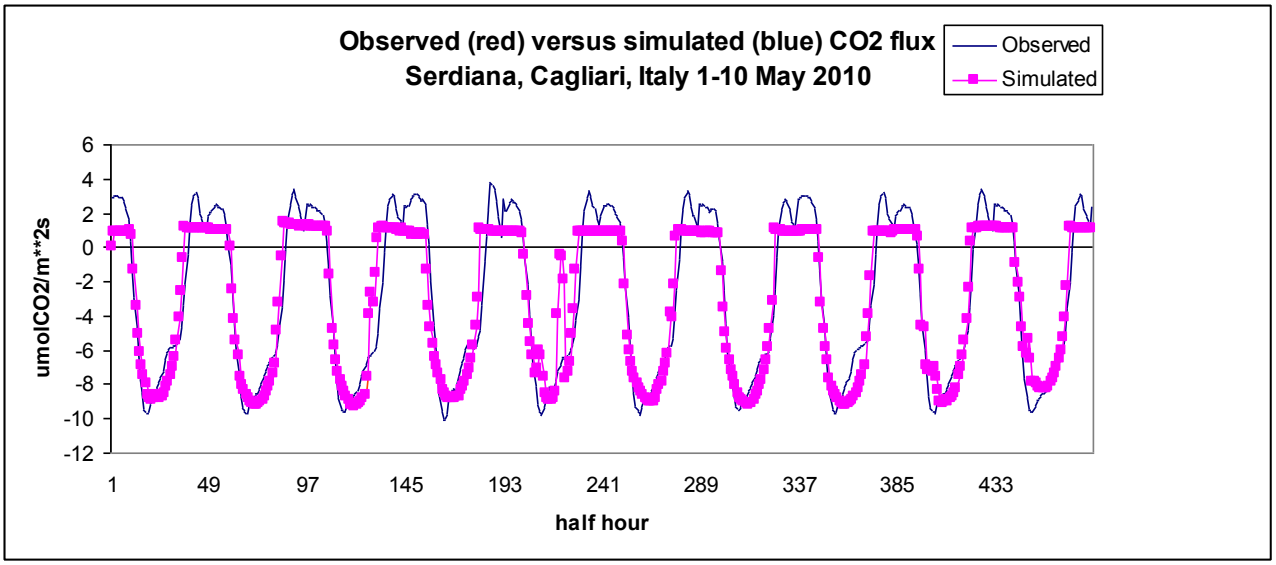

Fig. 7.1.1.2. Comparison between observed and simulated data set during the first 10 days of May 2010.

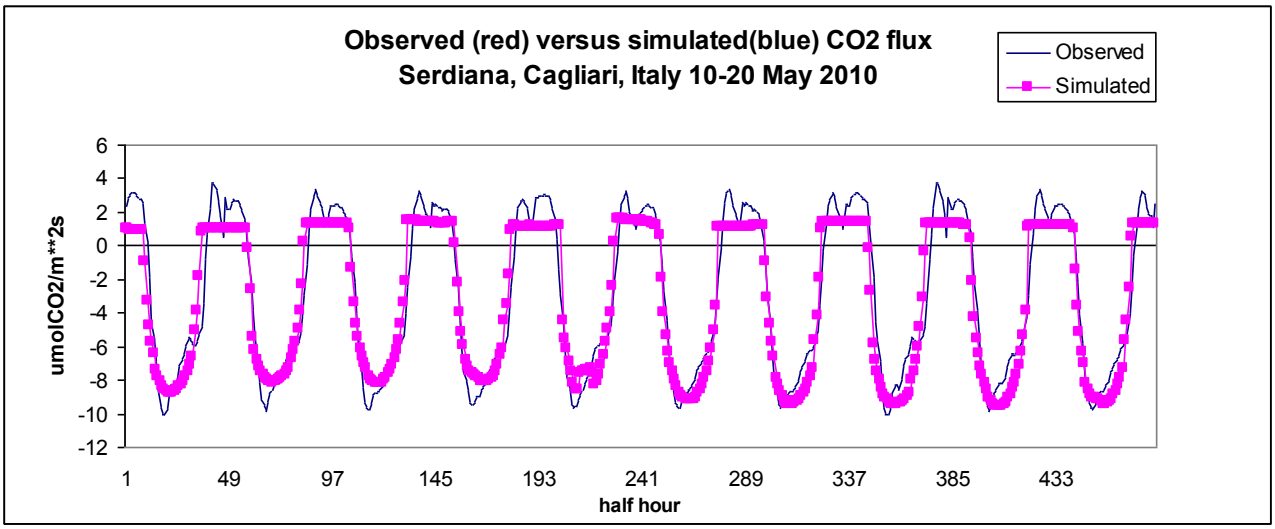

Fig. 7.1.1.3. Comparison between the observed and simulated data set from 10 to 20 May 2010.

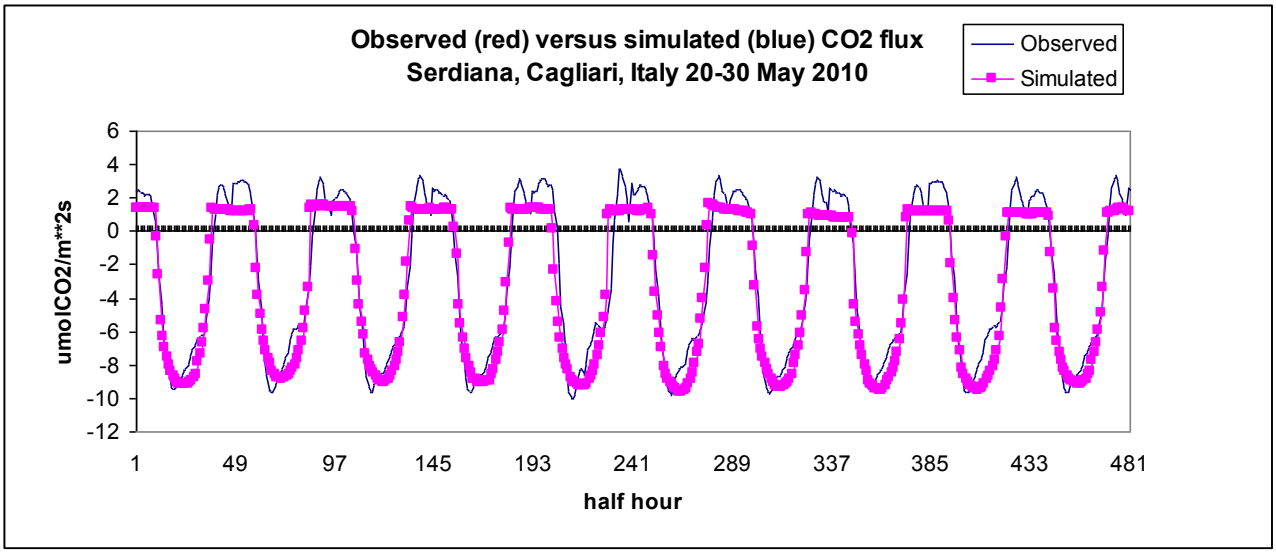

Fig. 7.1.1.4. Comparison between observed and simulated data set for the last 10 days of May 2010.

As it is clear from a first graphic analysis of Figg. 7.1.1.2-7.1.1.4, the model shows its better performance for the carbon exchange rate between -1.5 to 6.0 $\mu molCO_2m^{-2}s^{-1}$, while for values outside this range the observed and modeled values differ somewhat more, although these differences are not overwhelming.

7.1.2 Half-hour aggregated data analysis

Considering the aggregated data, the mean and standard deviation were calculated, together with the RMSE, MAE, MBE and correlation coefficients between observed and simulated data. All parameters are listed in the Table 7.1.2.1, while the trend-lines, including error bars, are depicted in Fig. 7.1.2.1.

First of all it is important to point out the low values of the correlation coefficient between the simulated and the observed data belonging to the same half-hour interval: only in two cases overcame the threshold of 0.3. Technically it is because the standard deviations of the group are higher than variation due to the physic phenomena, so a correlation cannot be evidenced. On the other hand, it means that all the information contained in the time series have been exploited and, also if the observed data were available in shorter time step (for example 15 min), it would have made little sense to aggregate the data in a larger number of groups (for example 96).

In this case comparison of standard deviation with mean values of both observed and simulated data shows a ratio considerably smaller with respect to the non-aggregated data case. Except for morning and evening transitions data, this ratio is always lower than 20% and, for some periods of the day, is around 4-5%.

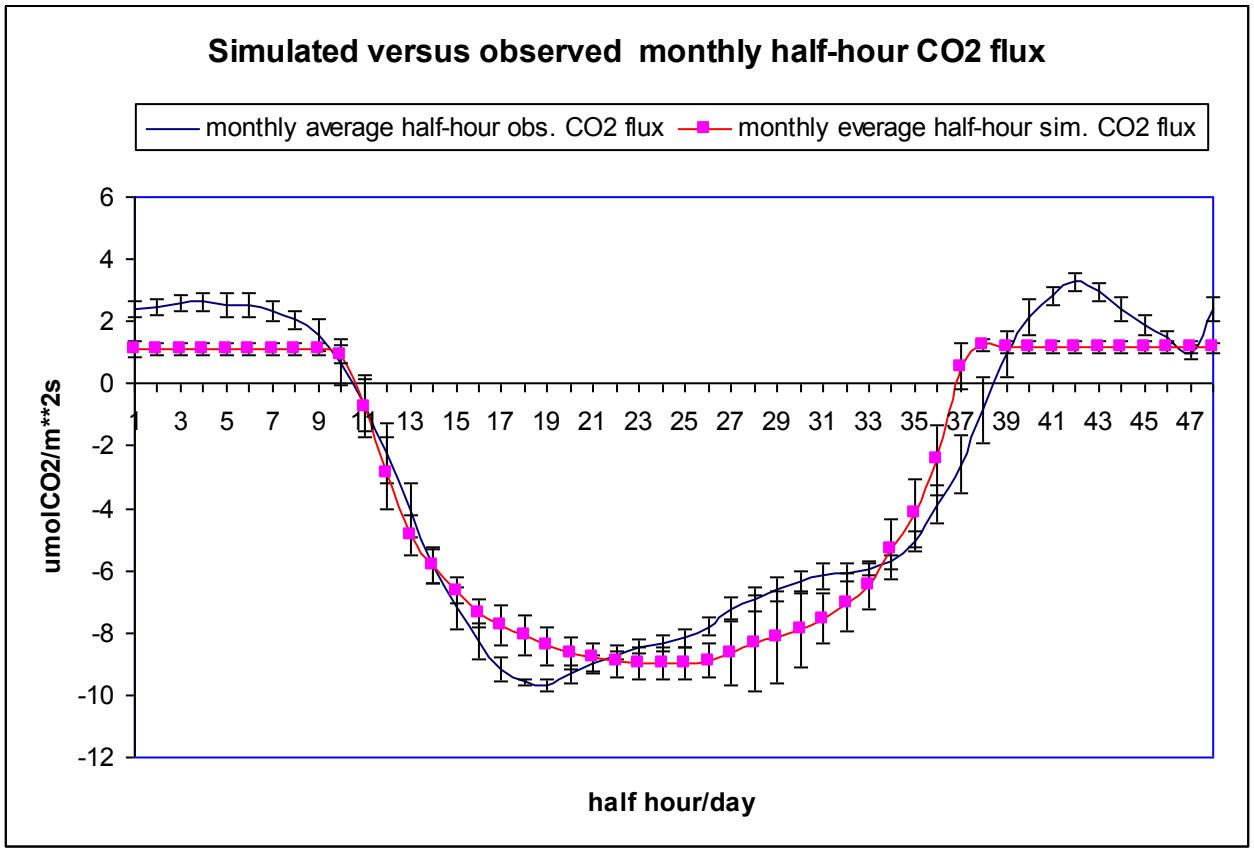

Fig. 7.1.2.1. Comparison between simulated and observed data. Data are sorted by time and averaged.

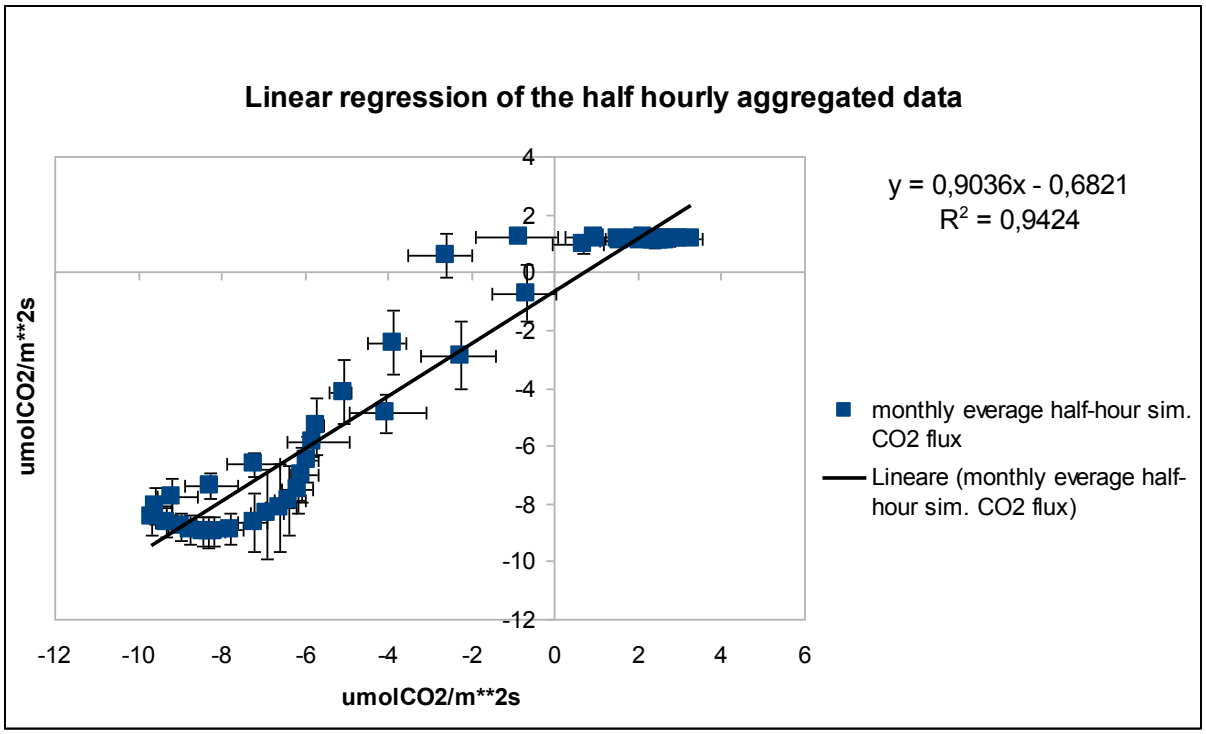

Fig 7.1.2.2. The least squared relative to the linear regression for the aggregated data set.

Table 7.1.2.1. Statistical parameters calculated for the mean values of the aggregated time series

Half hour n.	Observed	Simulated	RSME_O-S	MAE_O-S	MBE_O-S	Corr. Coeff.
	$\mu molCO_2m^{-2}s^{-1}$	$\mu molCO_2m^{-2}s^{-1}$	$\mu molCO_2m^{-2}s^{-1}$	$\mu molCO_2m^{-2}s^{-1}$	$\mu molCO_2m^{-2}s^{-1}$	
1/48	2.38 ± 0.27	1.11 ± 0.28	1.35	1.28	1.28	-0.34
2/48	2.46 ± 0.28	1.13 ± 0.19	1.38	1.33	1.33	-0.17
3/48	2.58 ± 0.24	1.13 ± 0.19	1.49	1.46	1.46	-0.16
4/48	2.65 ± 0.29	1.11 ± 0.19	1.58	1.54	1.54	-0.16
5/48	2.54 ± 0.37	1.12 ± 0.19	1.49	1.43	1.43	-0.15
6/48	2.53 ± 0.36	1.12 ± 0.19	1.48	1.41	1.41	-0.17
7/48	2.34 ± 0.32	1.11 ± 0.19	1.29	1.23	1.23	-0.14
8/48	2.06 ± 0.30	1.11 ± 0.19	1.02	0.95	0.95	-0.09
9/48	1.58 ± 0.50	1.11 ± 0.19	0.71	0.48	0.47	-0.07
10/48	0.68 ± 0.73	0.93 ± 0.30	0.87	0.71	-0.25	-0.22
11/48	- 0.69 ± 0.83	-0.72 ± 0.97	1.39	1.10	0.03	-0.23
12/48	-2.24 ± 0.97	2.86 ± 1.18	1.79	1.38	0.62	-0.26
13/48	-4.07 ± 0.89	-4.87 ± 0.67	1.47	1.08	0.80	-0.30
14/48	-5.82 ± 0.60	-5.86 ± 0.54	0.91	0.75	0.04	-0.33
15/48	-7.20 ± 0.67	- 6.66 ± 0.42	1.02	0.87	-0.54	-0.26
16/48	-8.28 ± 0.58	-7.39 ± 0.46	1.17	1.04	-0.89	-0.12
17/48	-9.17 ± 0.37	-7.75 ± 0.63	1.60	1.42	-1.42	-0.10
18/48	-9.57 ± 0.11	-8.08 ± 0.65	1.62	1.49	-1.49	0.05
19/48	-9.69 ± 0.17	-8.43 ± 0.63	1.42	1.26	-1.26	-0.01
20/48	-9.33 ± 0.28	-8.66 ± 0.51	0.87	0.68	-0.67	0.08
21/48	-8.98 ± 0.29	-8.80 ± 0.49	0.56	0.43	-0.18	0.11
22/48	-8.73 ± 0.12	-8.92 ± 0.50	0.53	0.44	0.19	0.08
23/48	-8.44 ± 0.21	-8.97 ± 0.50	0.74	0.67	0.53	0.08
24/48	-8.32 ± 0.25	-8.99 ± 0.52	0.85	0.77	0.67	0.16
25/48	-8.17 ± 0.32	-8.96 ± 0.52	0.96	0.83	0.79	0.20
26/48	-7.79 ± 0.30	-8.88 ± 0.53	1.22	1.09	1.09	0.23
27/48	-7.22 ± 0.37	-8.64 ± 1.03	1.76	1.65	1.43	0.11
28/48	-6.90 ± 0.39	-8.35 ± 1.55	2.12	1.87	1.45	0.08
29/48	-6.58 ± 0.38	-8.14 ± 1.50	2.16	1.96	1.56	0.09
30/48	-6.37 ± 0.35	-7.90 ± 1.22	1.98	1.84	1.53	-0.05
31/48	-6.17 ± 0.40	-7.53 ± 0.81	1.63	1.52	1.36	-0.05
32/48	-6.07 ± 0.28	-7.03 ± 0.94	1.37	1.19	0.96	-0.08
33/48	-5.94 ± 0.19	-6.48 ± 0.79	0.97	0.78	0.55	0.03
34/48	-5.72 ± 0.21	-5.30 ± 0.98	1.04	0.66	-0.42	0.15
35/48	-5.08 ± 0.33	-4.15 ± 1.11	1.42	0.99	-0.93	0.20
36/48	-3.88 ± 0.61	-2.43 ± 1.12	1.84	1.49	-1.46	0.24
37/48	-2.60 ± 0.91	0.56 ± 0.76	3.38	3.16	-3.16	-0.05
38/48	-0.84 ± 1.05	1.23 ± 0.19	2.30	2.06	-2.06	0.12
39/48	0.96 ± 0.72	1.20 ± 0.19	0.75	0.47	-0.24	0.13
40/48	2.14 ± 0.59	1.19 ± 0.18	1.11	1.06	0.95	0.16
41/48	2.82 ± 0.27	1.18 ± 0.18	1.67	1.64	1.64	0.17
42/48	3.27 ± 0.26	1.17 ± 0.18	2.12	2.10	2.10	-0.01
43/48	2.96 ± 0.30	1.17 ± 0.18	1.82	1.79	1.79	-0.08
44/48	2.38 ± 0.38	1.17 ± 0.18	1.29	1.21	1.21	-0.14
45/48	1.90 ± 0.34	1.17 ± 0.18	0.83	0.73	0.73	-0.10
46/48	1.51 ± 0.20	1.16 ± 0.19	0.45	0.37	0.35	-0.11
47/48	1.01 ± 0.20	1.16 ± 0.1	0.30	0.23	-0.15	0.05
48/48	2.40 ± 0.39	1.15 ± 0.18	1.32	1.25	1.25	-0.16

Table 7.1.2.2. Correlation coefficient, linear regression slope, intercept and R2 calculated for the mean values of the aggregated time series.

Corr. Coeff	Slope	Intercept	Std. Dev.	R^2
			$\mu molCO_2m^{-2}s^{-1}$	
0.97	0.90±0.03	-0.68± 0.18	1.06	0.94

Further features become evident when examining daytime and nighttime data in two separate sets. Daytime values span from 6:00-6:30 PM until 5:00-5:30 AM, while nighttime values cover the remaining times. On one hand, during the night, there is no photosynthetic activity and the model correctly simulates a positive emission of carbon due to the nocturnal plant respiration acting alone. On the other hand, considering the Mean Bias Error (MBE) and the mean absolute error (MAE) in the interval of the 8 hours centered on midnight, it is possible to notice as values are positive (excepted for the two half-hour number 46 and 47). It means that the model regularly under estimated the observed nocturnal respiration emission (RECO). It is easy also to note a peak at 9:00 pm and the fall at 23:30 pm in the measured emission rate. This feature should be investigated together with the wind direction data in order to understand whether advection from locally contrasting CO_2 emissions can significantly alter the measurements. Indeed, the 80 m fetch of the meteorological station is not completely positioned inside of the vineyard: as described in the previous chapter, in a little angular sector of 45° located 60 m from the tower in the south-southwest direction an olive plant vegetation area is present. Unfortunately wind direction data are not available for the simulated month.

In the diurnal time-interval, the model performs remarkably well. Error bars for simulated and observed values overlap during the entire period, except for the half hours number 17-18 and 37-38, corresponding to morning and evening transitions, Looking at the graphic it is possible to observe as the model slightly underestimates the carbon emission before the noon, while after the noon it

over estimates the CO_2 flux. The condition of rising temperatures likely reduces the net rate of carbon uptake by plants, due to increased respirational excitation, and if it is true for this site, this is perhaps not perfectly seen by the model. Considering this fact, together with the nighttime underestimation, it is reasonably to guess that the leaf area index used in the simulation could be lower than the real LAI value. This effect in the daytime is hidden and compensated by the thermal lowering of the carbon uptake rate. A higher LAI value together with a higher sensibility in thermal closure of stems could impress the final improve in the model performance. These differences can also be related to the simple Arrhenius-type exponential equation, which controls the chemical reaction rate: this equation is parameterized through a "Q-10" temperature coefficient, which is a measure of the rate of change of a biological or chemical system as a consequence of increasing the temperature by 10 °C. It is possible that this parameterization does not capture diurnal patterns of plant catabolism.

The correlation coefficients calculated for the mean values of each one of the 48 half-hour groups of simulated data, and the corresponding values of observed data is 0.97 (Table 7.1.2.2) with a P-value < 0.0001. A linear regression between the two data set was also performed, and a graphical illustration of the least squared line is shown in Fig. 7.1.2.2. The slope of the least squared line is 0.90±0.03 with an intercept of -0.68±0.18. It means that there is 95% probability that the slope is between 0.84 and 0.96 and the intercept is between 0.32 and 1.00.From an inferential point of view, in this case there is no gain with respect to the non-aggregated data. R^2 value is 0.94 with a P-value <0.0001. Thus the data aggregation improves the correlation between the regression model between predicted and observed data. In conclusion, it is possible affirm that, using a sufficiently correct parameterization, the model is able to explain more than 90% of observations at this site.

7.2 Methodology validation

The second step in this study is the development of a methodology by which carry out the map of carbon exchange for the entire island of Sardinia. After the single point time series validation, in order to validate the simulation general framework, the verification of the other working hypothesis described in the previous chapter is required: the changing of the parameters for the pixels belonging to land use type number 2 should not appreciably affect simulations over the remaining part of the territory. Only in this case, the modification can be considered a small perturbation of the general structure, which remains intact throughout the simulation.

In addition to the Sardinian CO_2 flux map obtained using the vineyard morphological parameters values for all land use types included into the class number 2 (first simulation), a second 30-day simulation using the WRF-ACASA default parameterization was conducted to verify the second hypothesis described above. Per each simulation, the map of the 30-day cumulative amount of carbon exchange was extracted. These two maps were used to create a further map representing the difference between the two simulations in 30-day cumulative amount of exchanged carbon.

The difference map is depicted in Fig. 7.2.1, while depicted in Fig. 7.2.2 is the land use map. It can be appreciated a significant difference only in the pixels that were the focus of the LAI alterations mentioned previously, those of land use type 2. It can be observed in the figure as the dark blue tiles in the land use map overlapping perfectly with the dark green tile in the carbon difference map.

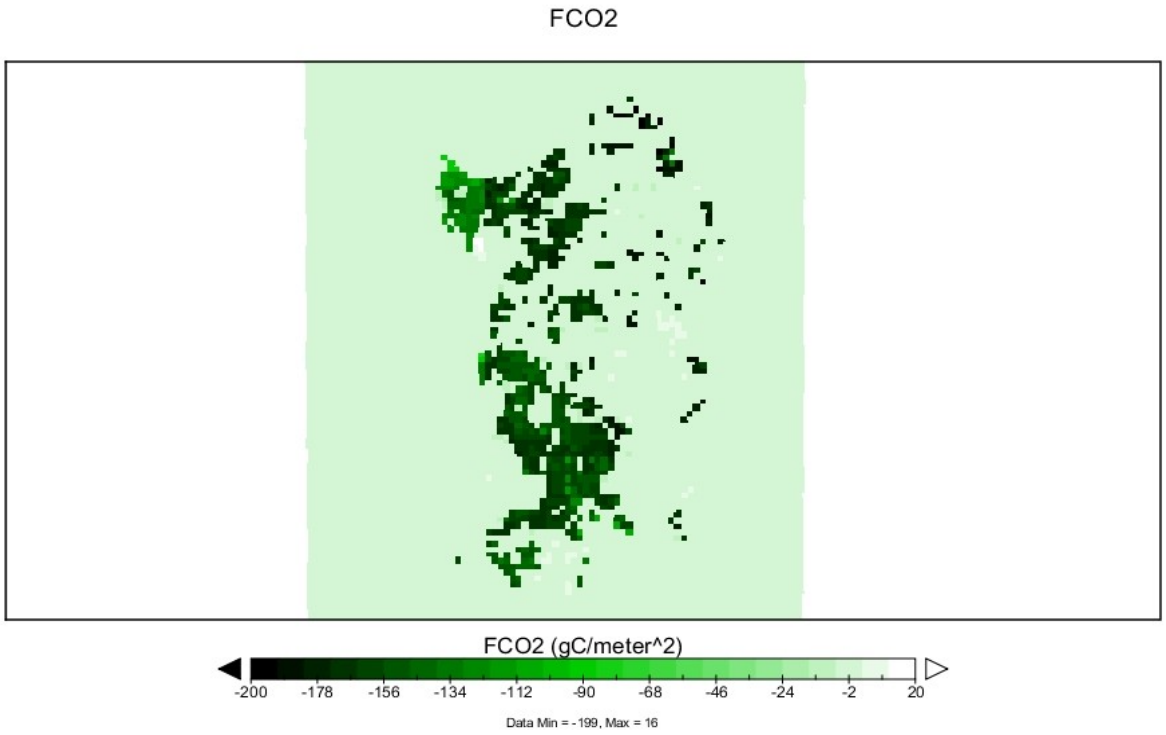

Fig 7.2.1. Difference map between the simulation elaborated with the changed parameters for land use type number 2, and the one with the default correct WRF-ACASA parameters.

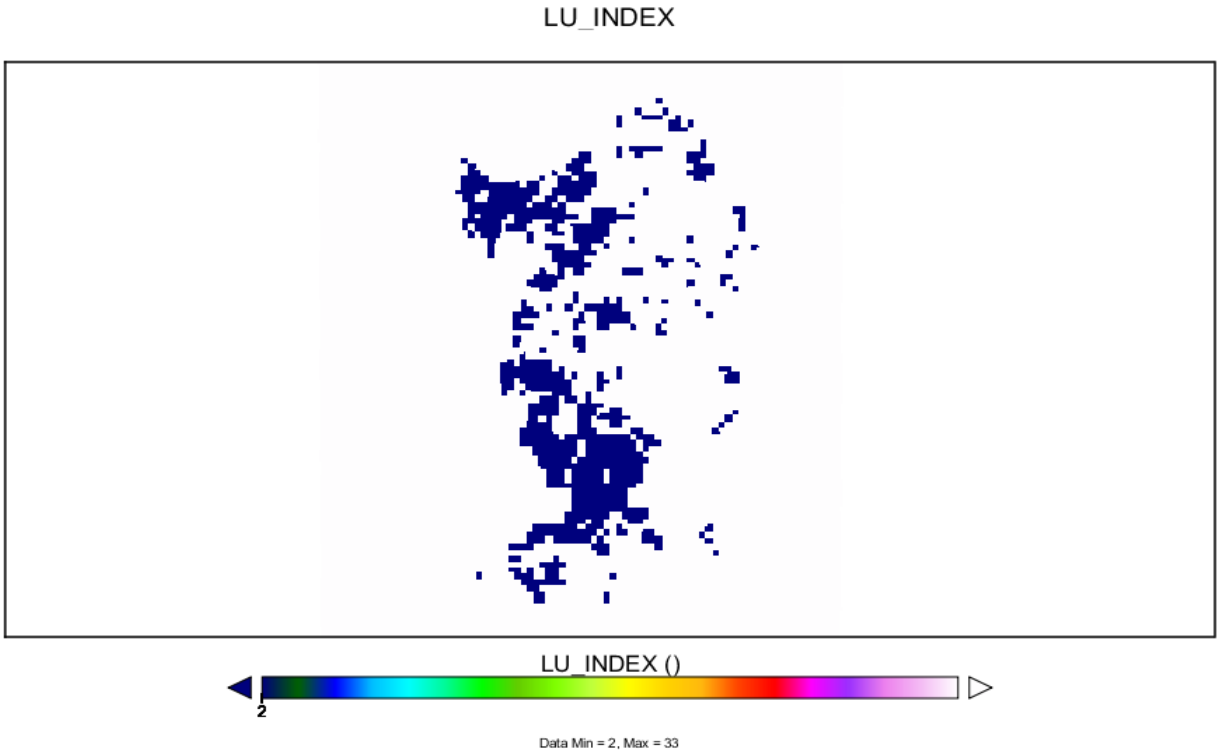

Fig 7.2.2. Dark blue tile show the land use category number 2, it is the land use category of the validating point.

This last feature validates the general framework of this investigation. Consequently with the working hypothesis, the Sardinian map of carbon exchange produced under these conditions and with the correct parameterization can be considered validated as well.

7.3 Sardinian CO_2 map

The simulations performed with WRF-ACASA generate a NetCDF file from which it was possible to extract the map depicted in the Fig 7.3.1. It is shown the carbon exchange for the entire month of May 2010 for Sardinia. The range spans from $-4.19 \cdot 10^2$ gCm^{-2} to $1.244 \cdot 10^3$ gCm^{-2}. It was also calculated the total amount for the entire island for the same period: 4.19 10^{12}g of carbon or 4.19 MtC.

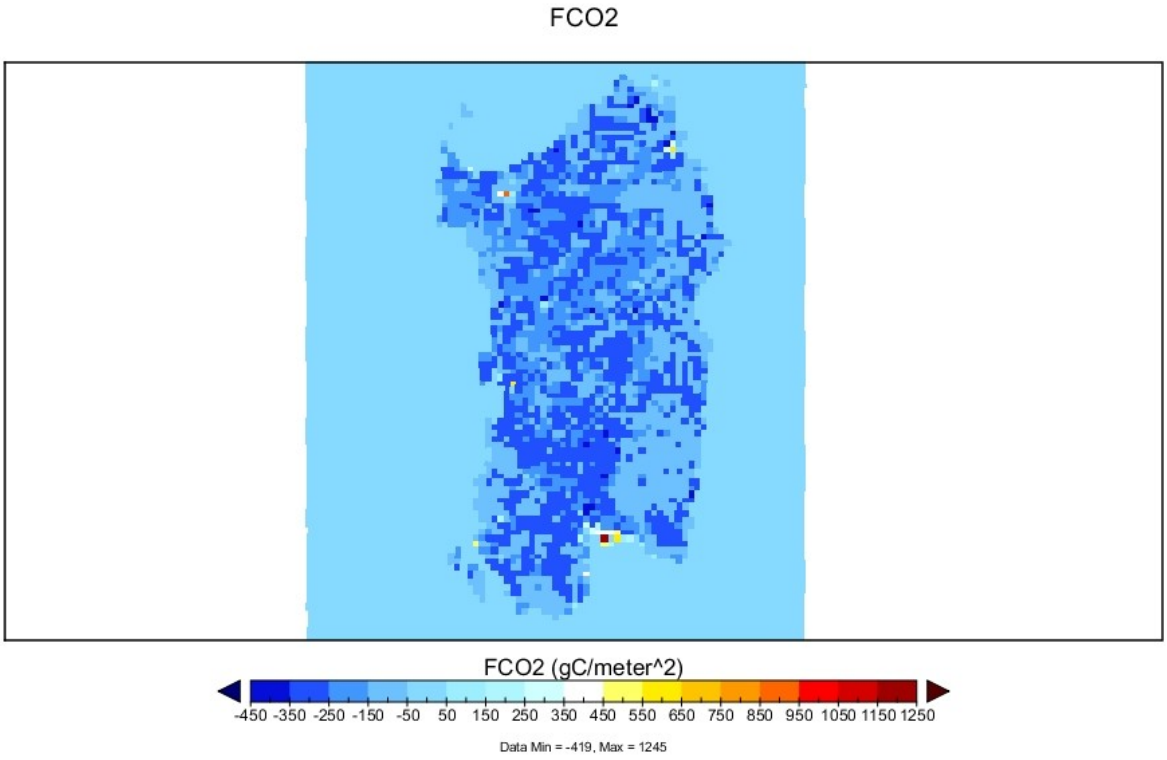

Fig 7.3.1. Sardinian map of carbon flux for the month of May 2010.

To highlight the areas of carbon uptake and emission, the Fig. 7.3.2 reports in green the areas with a net carbon uptake and, in brown and white, the net carbon release areas. In 7.3.3 is plotted the urban land use type. From the comparison of the two maps, it emerges as all the urban areas provide a positive contribution to the carbon exchange. In non-urban areas, except in the case of a few pixels indicated as net carbon sources, these vegetation-dominated land use types act as net sinks of carbon. The few exceptions of net carbon sourcing are related to the different kind of data that set the land use types and the population density: the former is considered an urban area only when this land use type is "dominant" in the pixel. So suburban areas, small cities, and rural towns cannot be labelled as urban in the WRF morphological description if they are not large enough. Conversely, the latter is a value that changes continuously, therefore the distribution of population is a number that is always considered nontrivial, even in remote areas.

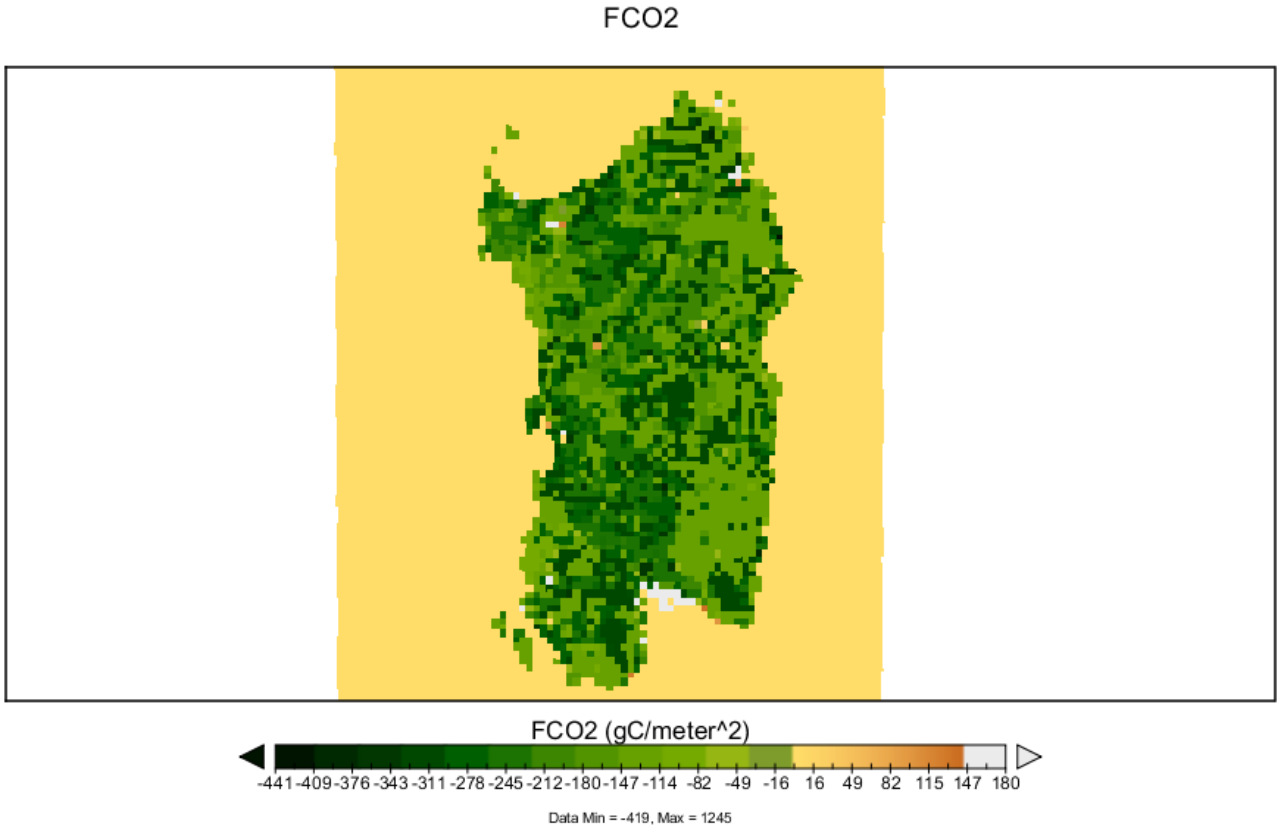

Fig. 7.3.2. Map of 30-day carbon flux with a focus on source areas, (in brown and white), and sink areas (in green).

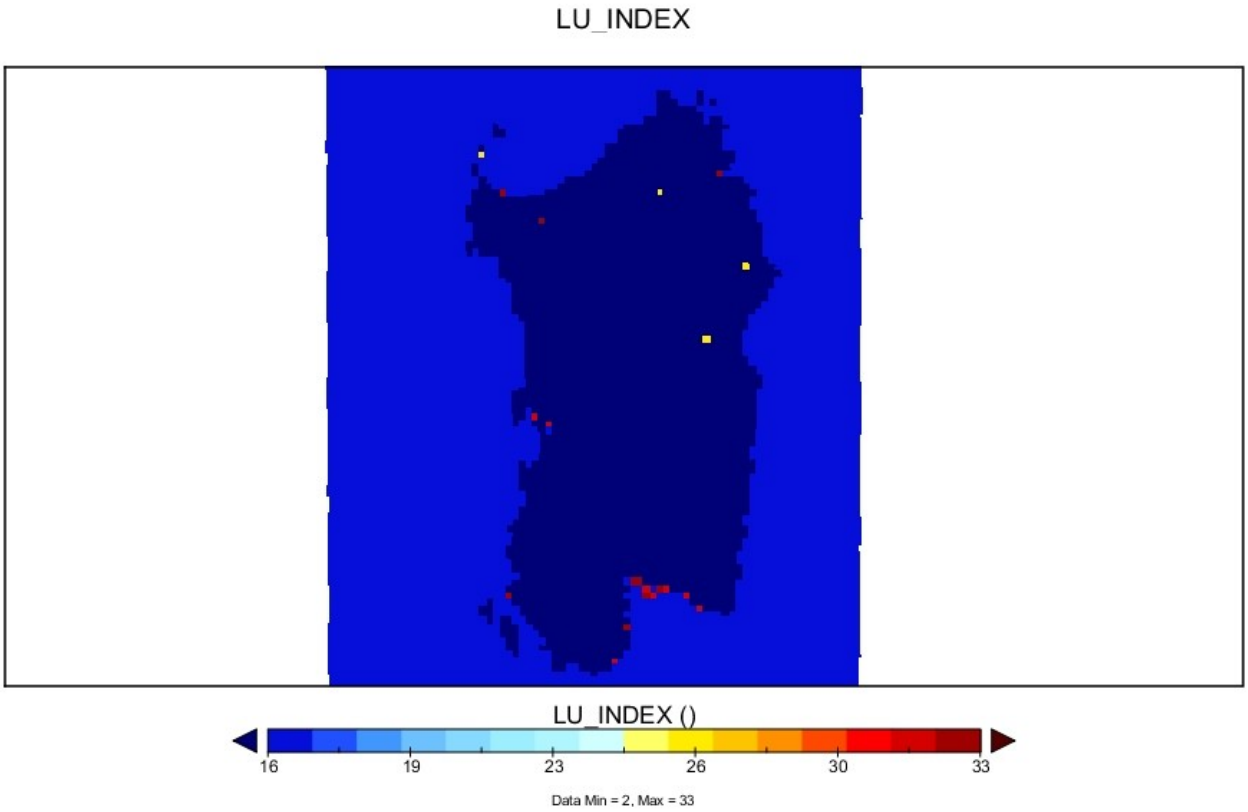

Fig 7.3.3. Urban land use types (dark red points).

It is important to emphasize that the sum of the territory represented by land use type numbers 2-3, 6-7, 8, 13-14-15, represents 80% of the total surface area of Sardinia. For each of these four groups, it is possible to identify typical range of carbon exchange.

Comparing the spatial distribution of maquis in Fig.7.3.4 (land use category number 8) and the map of the carbon exchange range between $-1.5 \cdot 10^2$ gCm^{-2} and 0 gCm^{-2} in Fig.7.3.5, it is possible observe that maquis has a net carbon uptake ranging between $-8 \cdot 10$ gCm^{-2} and $-1.45 \cdot 10^2$ gCm^{-2}. Only a few pixels are in the range between $-8 \cdot 10$ gCm^{-2} and 0 gCm^{-2}.

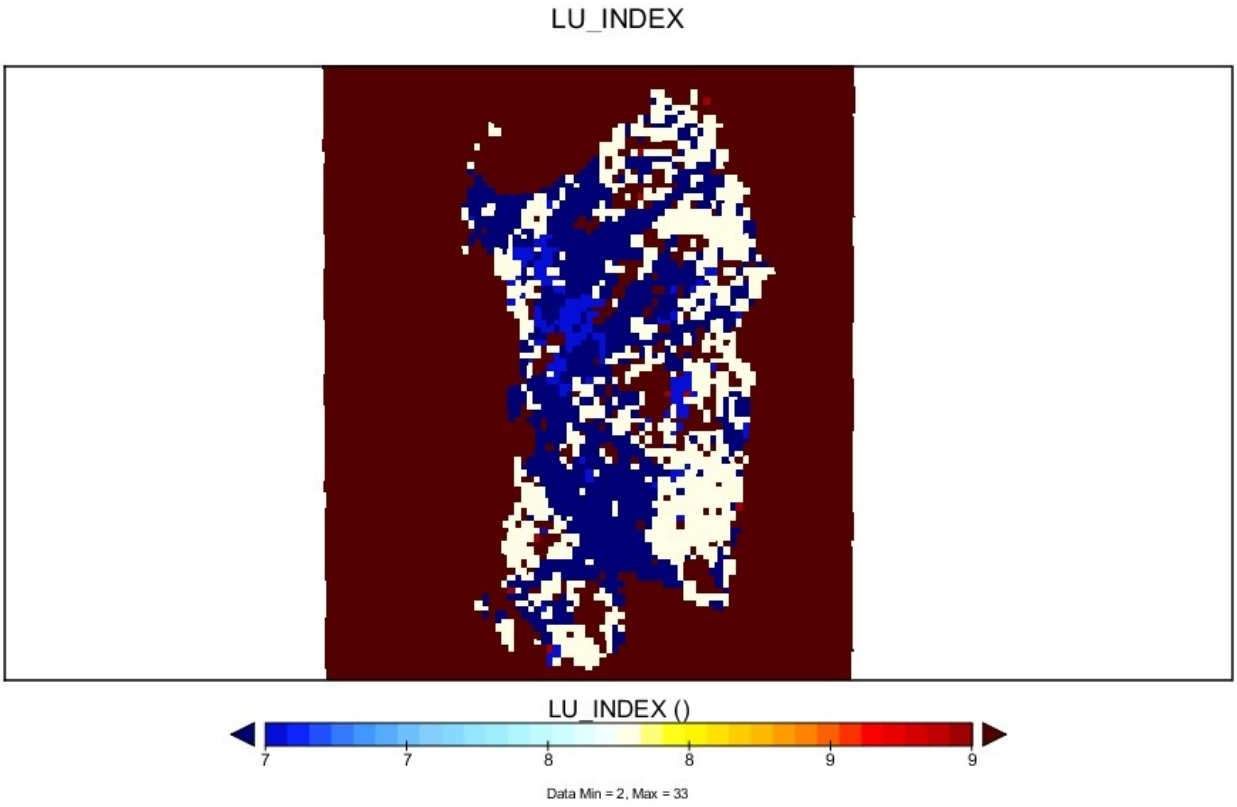

Fig.7.3.4 Land use type number 8 (Mediterranean maquis) plotted in white

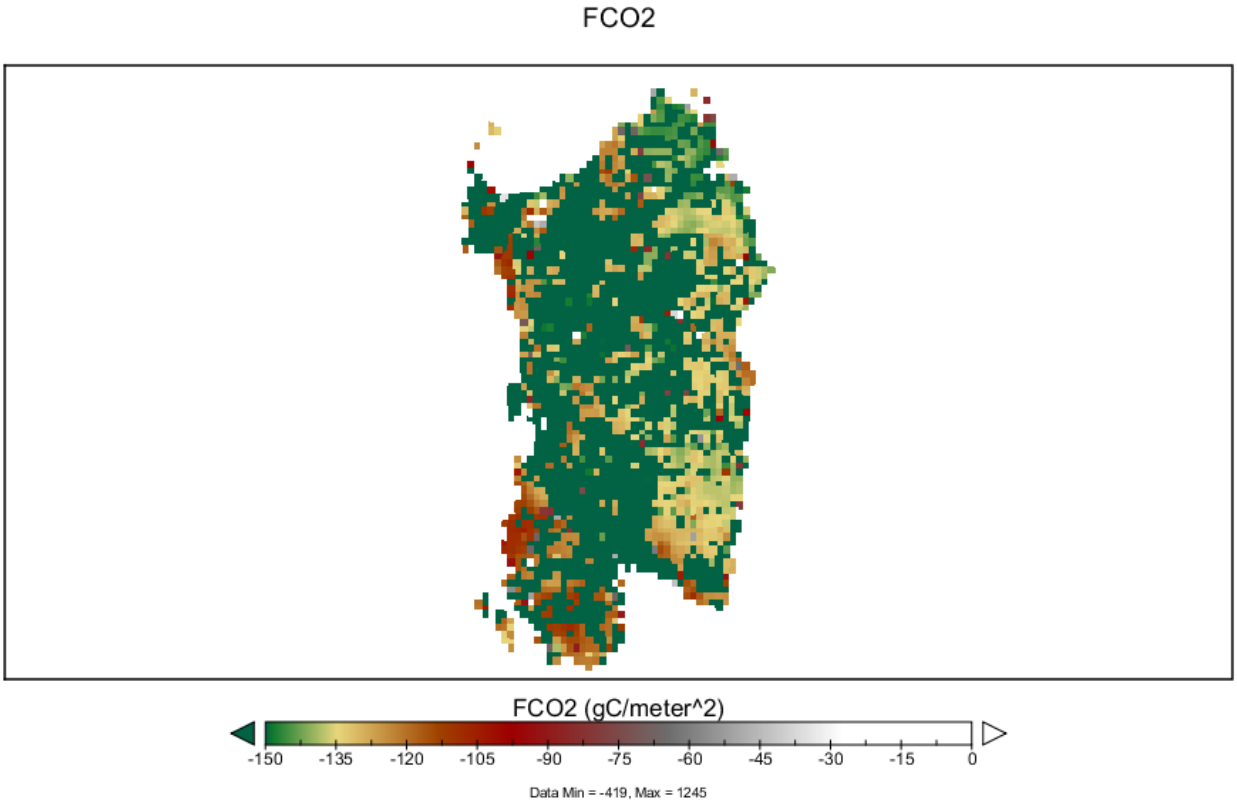

Fig 7.3.5. Map of 30-day carbon flux in the range -1.5·10^2 gCm^{-2} -0 gCm^{-2}.

Fig 7.3.6. Location of the Arca di Noe' natural reserve.

To have a general idea of how the model represents reality, it is of interest to compare the 30-day total amount of carbon uptake simulated by WRF-ACASA with observed values found in literature for other areas. The aim of this comparison is not to perform as a strict validation process as it was provided in the previous section, but rather to check whether model estimates for these landscapes are within the same order of magnitude of literature values. In fact, the actual carbon exchange varies depending on the meteorological conditions of the observation period, and all places possess different biota, so model and observed values will disagree regardless of the goodness of results of the simulation, but it is cogent to guess that they should have at least the same order of magnitude. Within the work of Marras et al. (2011) can be found the monthly observed value of the carbon exchange during the three years 2004-2006 for a site located in the Arca di Noe' natural reserve,

Alghero, Sardinia, which is replete with Mediterranean maquis vegetation. The exact position of the Eddy Covariance tower is 40°36'18''N, 8°9'7''E, and it corresponds to the pixel (21,81) of the simulated map. WRF correctly registers the pixel in question as land use type number 8. The measured value was estimated to be ~$9 \cdot 10$ gCm^{-2}, while the simulation forecasted an uptake of $1.15 \cdot 10^2$ gCm^{-2}, as can be seen in the Fig. 7.2.7. Based on these values, the model seems to produce reliable simulations.

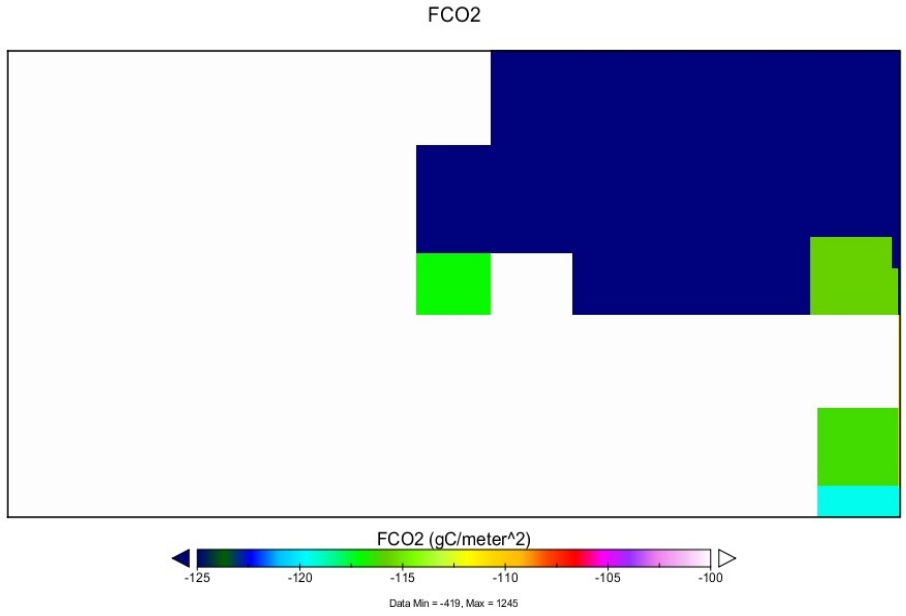

Fig 7.3.7. Map of 30-day carbon flux in the Northern Sardinia. The central pixel in green is (21,81) the ones in which is located the "Arca di Noe" Eddy covariance tower.

In the Fig. 7.3.8 the yellow and white pixels identify the land use categories number 6 (Cropland/Woodland Mosaic) and 7 (Grassland), respectively. Fig. 7.3.9 shows the carbon exchange range between $-2.1 \cdot 10^2$ gCm^{-2} and $-1.5 \cdot 10^2$ gCm^{-2} (orange, yellow, white and clear blue pixels). From the comparison of the two maps, it is possible to recognize the carbon exchange due to the land use categories 6 and 7.

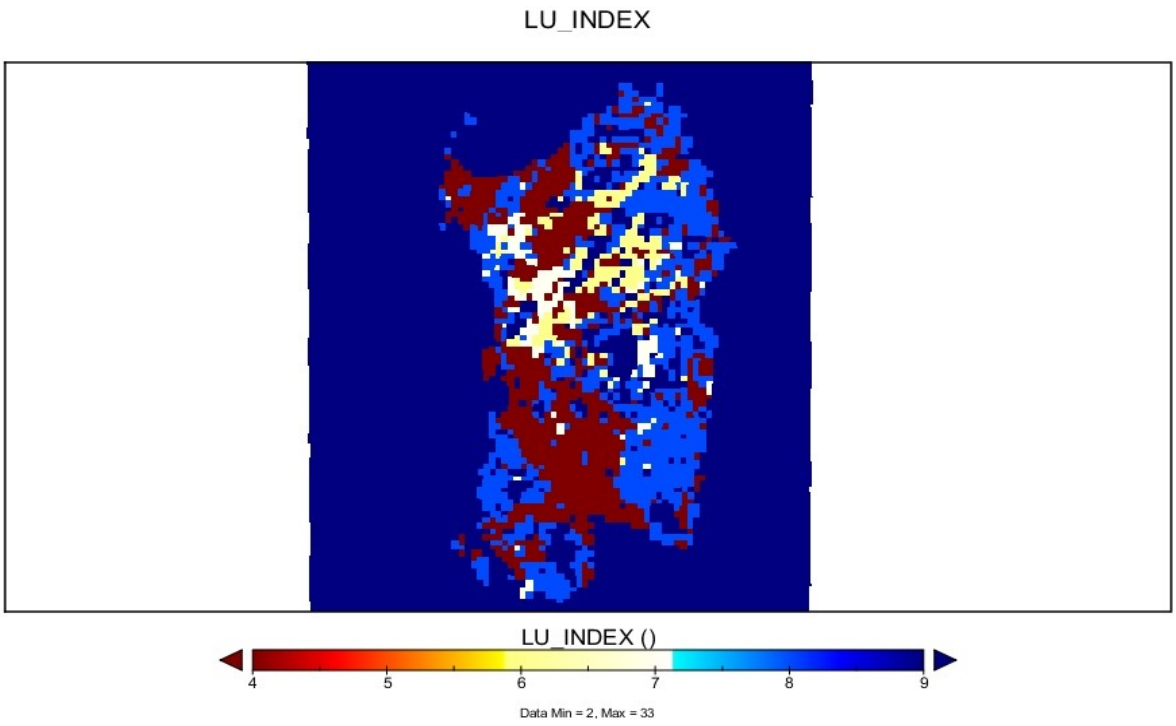

Fig 7.3.8. Land use type 6 and 7 (yellow and white pixels).

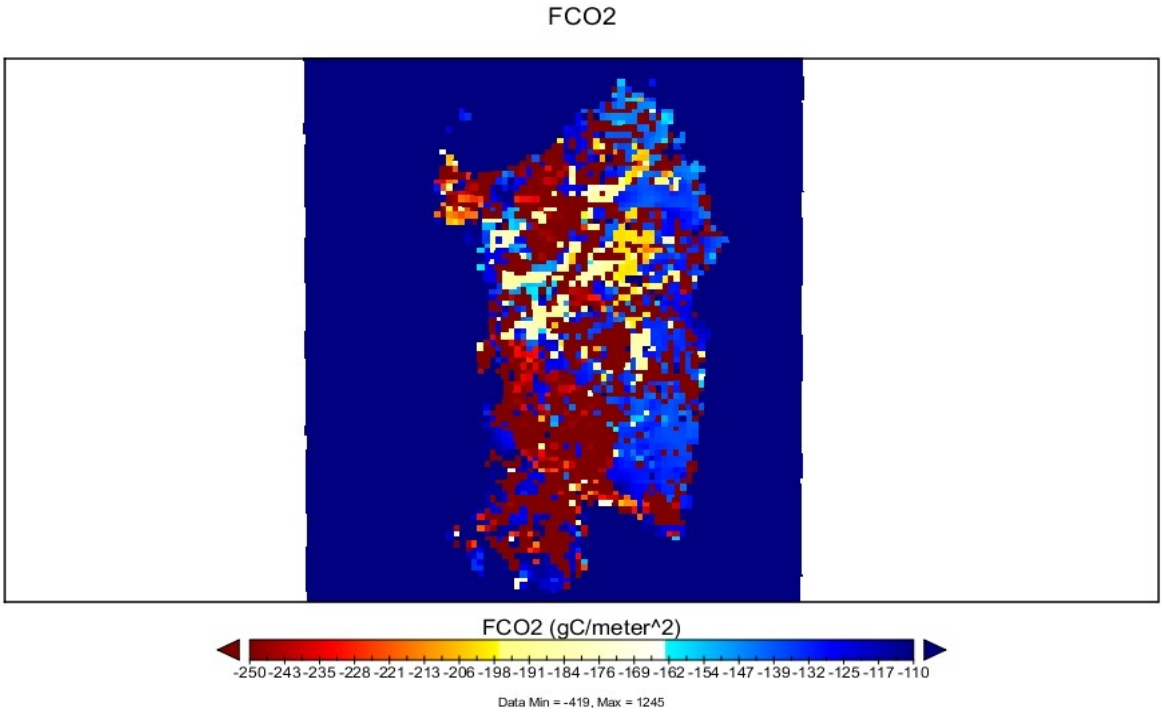

Fig.7.3.9 Orange, yellow, white and clear blue pixels shows the 30-day carbon emission range -2.1·10^{2}gCm^{-2} and -1.5·10^2 gCm^{-2}

The land use types numbers 2 and 3, representing “Dryland Cropland and Pasture” and “Irrigated Cropland and Pasture”, respectively, have a monthly carbon uptake rate that mainly spans between $-2.9 \cdot 10^2$ gCm^{-2} and $-2.2 \cdot 10^2$ gCm^{-2}, as it can be seen when comparing Figures 7.3.10 and 7.3.11.

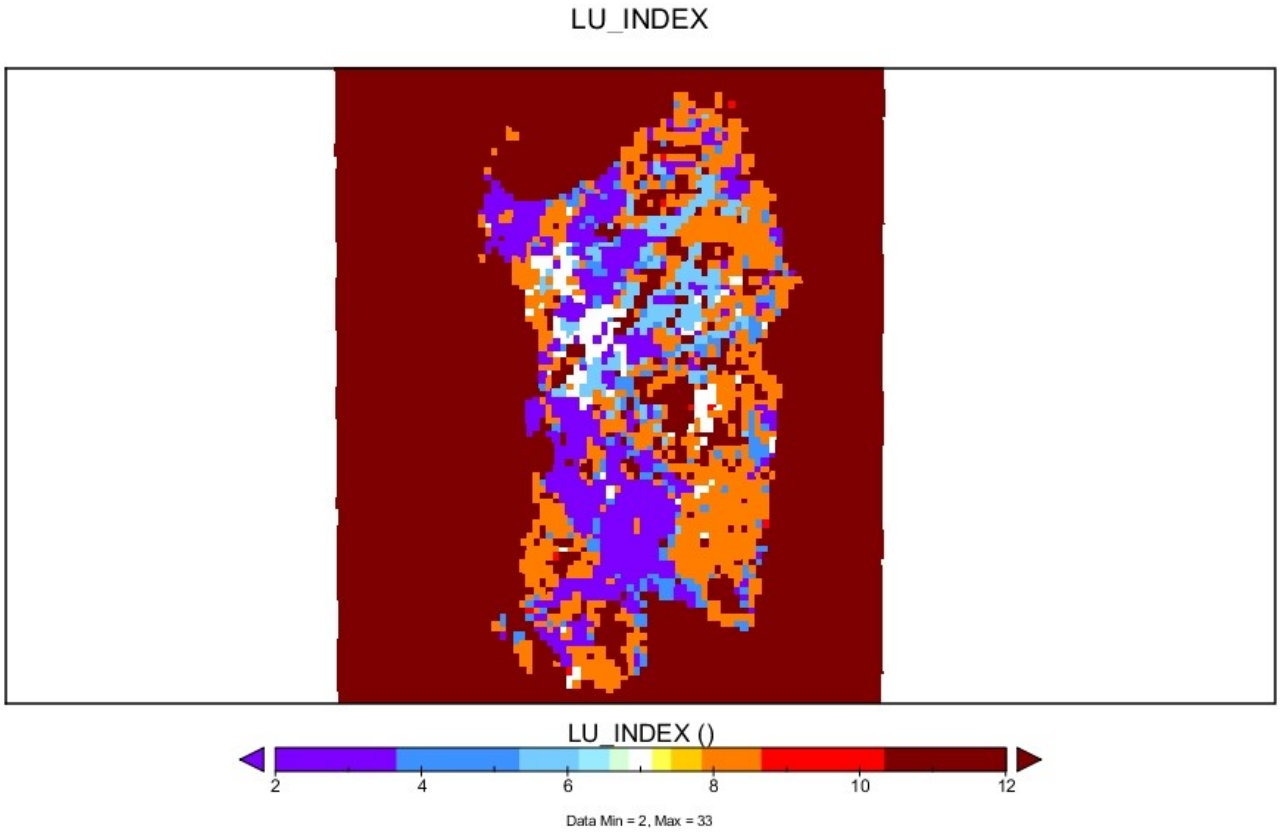

Fig 7.3.10 Land use type number 2 and 3 (violet pixels).

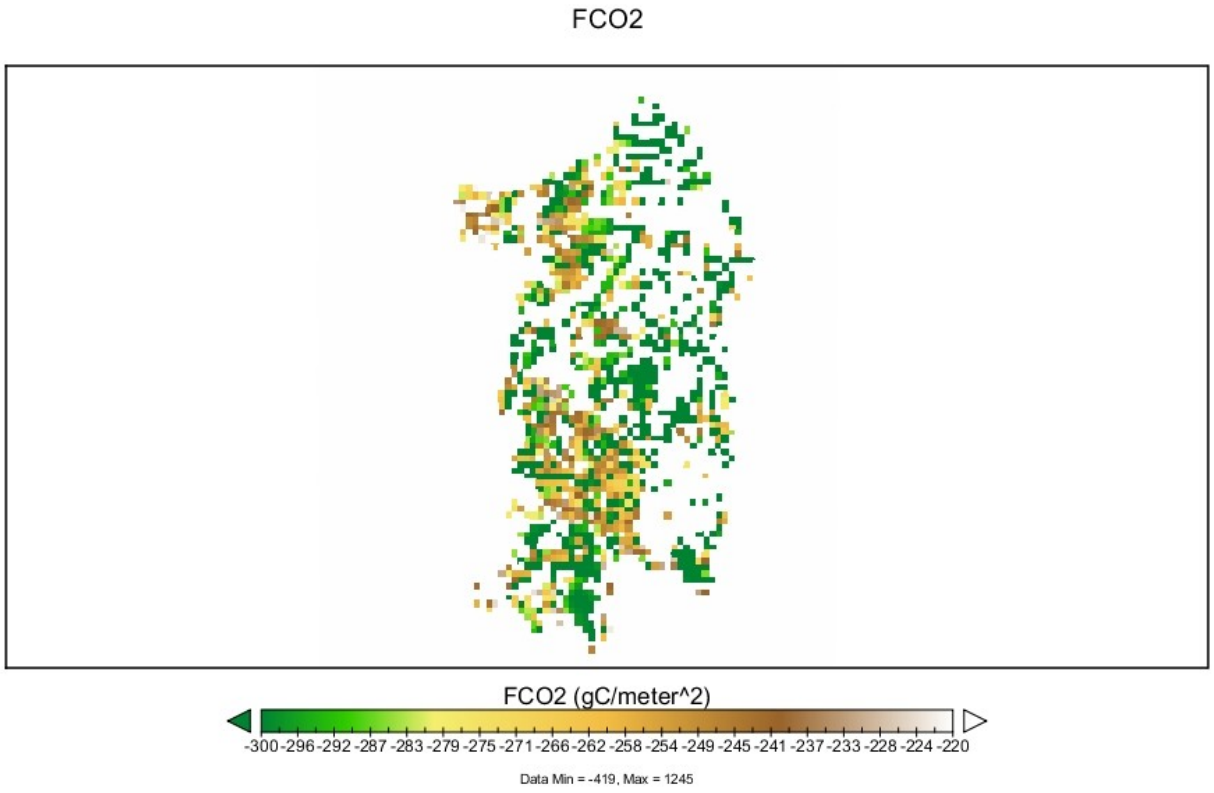

Fig. 7.3.11. Map of the 30-day carbon exchange between -3·10² gCm⁻² and -2.2·10² gCm⁻², brown and clear green pixels shows the range between -2.8·10²gCm⁻² and -2.35·10² gCm⁻².

In Fig. 7.3.12 yellow white and blue pixels show the territorial distribution of vegetation types involving the Mediterranean forests, mainly represented by *Quercus ilex* and, in second order, by *Quercus suber*. Comparing this map with the spatial distribution of the brown pixels in the Fig 7.3.14, representing the range of carbon exchange between $-2.90 \cdot 10^2$ gCm^{-2} and $-3.30 \cdot 10^2$ gCm^{-2}, it is possible to identify the above interval as the range emission of the Mediterranean forest. Although in the literature there are no observations in the Mediterranean forests in Sardinia, there are several studies characterizing the carbon exchange of this kind of ecosystem in similar sites outside the island. There is a wide variation among sites concerning the carbon uptake of the Mediterranean forests: for example in the work of Valentini et al. (2000) the annual carbon uptake measured (for fifteen years) at the Castelporziano site averaged $6.6 \cdot 10^2$ gCm^{-2} per year, while in the

Puéchabon forest located in the southern France, roughly $2.54 \cdot 10^2$ gCm^{-2}per year was observed (Allard et al. 2008). In the work of Garbulsky et al. (2008), the Mediterranean forest of Castelporziano in central Italy was also studied for five years. The climate in this region is Mediterranean, with 800 mm of mean annual rainfall and a mean annual temperature of 14.8°C over the 2001-2005 experimental period. In the five years, the observed mean value of GPP for the month of May was found to be ~10 gCm^{-2} per day. The average daily value predicted by the WRF-ACASA model for NEE (GPP–RECO) was found to be ~10 gCm^{-2} per day. Although the wide variation illustrated above, a little overestimate of the model WRF-ACASA can be guessed.

It is important to point out how the range of carbon exchange in "Dryland Cropland and Pasture" and "Irrigated Cropland and Pasture" categories are partially overlapped with the range for the Mediterranean forest. For example, it is possible to observe as the carbon uptake of a few "dry cropland and pasture" pixels surrounding the city of Olbia (located in the north east of the island) in the monthly map are greater than $3.5 \cdot 10^2$ gCm^{-2}. The phenomena are forecasted in zones near the sea, so high values of air humidity and soil moisture can cause an increase in carbon uptake. However, general trends of WRF-ACASA simulations are in agreement with the work of Ma et al. (2007) on Mediterranean forests and grassland. Non-irrigated grassland and pasture uptakes should be lower than the forest uptake, but during the month of May, values can be very close.

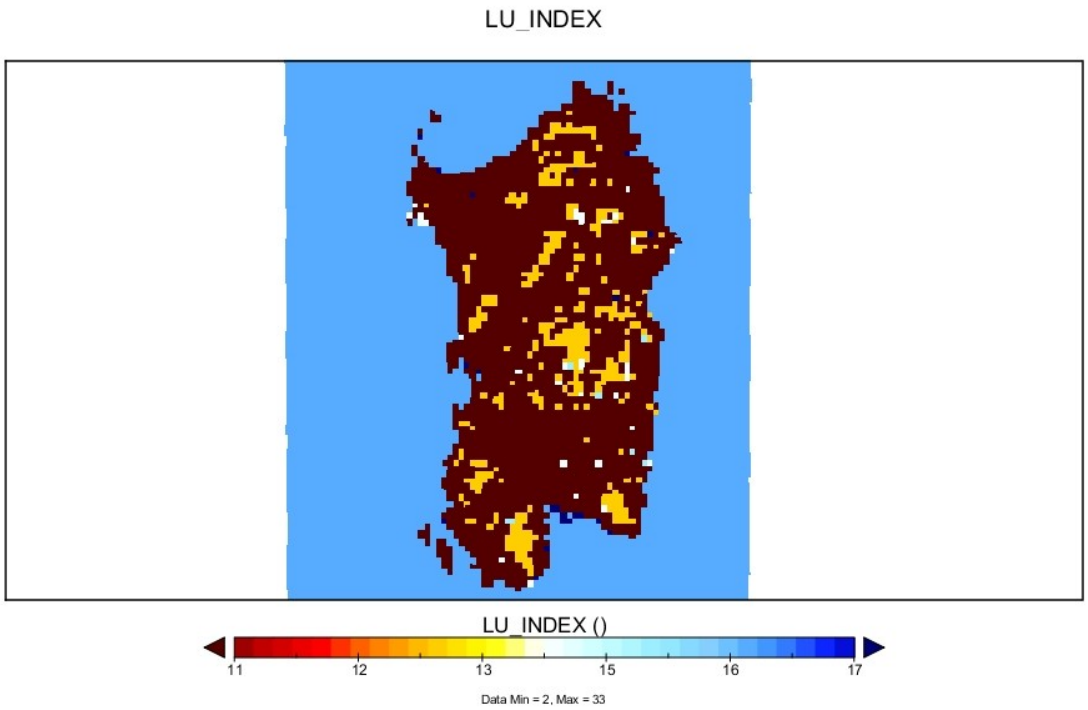

Fig. 7.3.12. In yellow the distribution on the territory of the Mediterranean evergreen forest (land use category number 13), in white the needleleaf evergreen forest (land use category number 14), and in clear blue the mixed forest (land use category number 15) are shown.

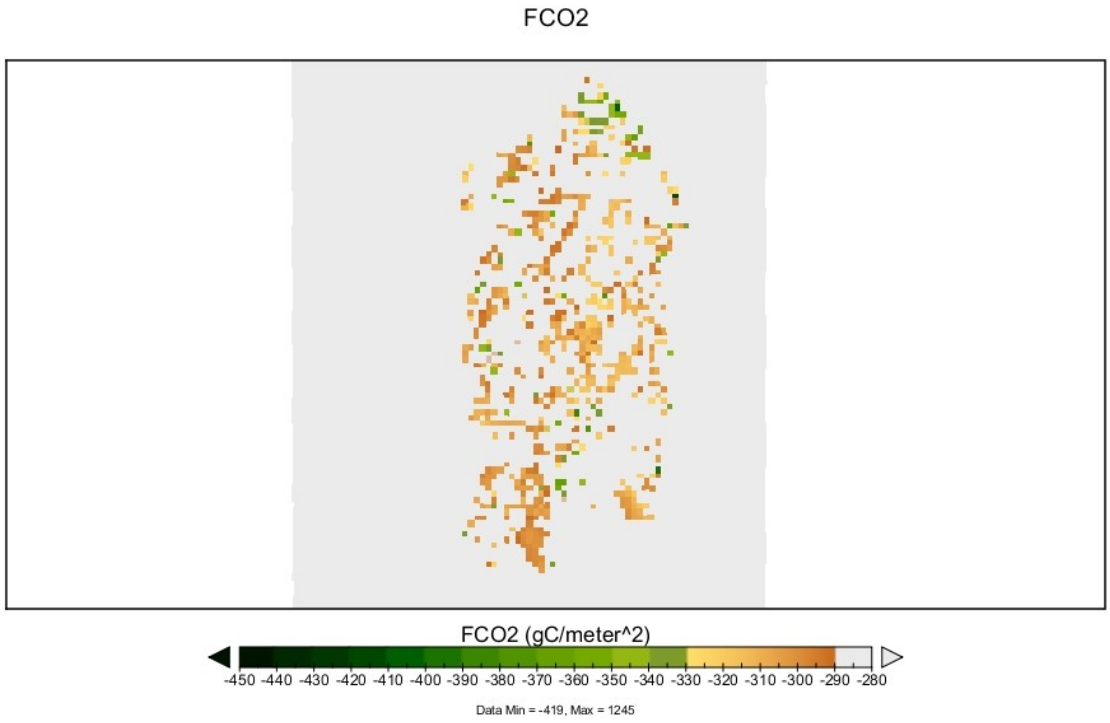

Fig 7.3.13. In brown are plotted the pixels corresponding to a 30-day carbon exchange range between -3.3·10² gCm⁻² and -2.9·10² gCm⁻².

8 Conclusion

It is now accepted by the scientific community that global warming and related climatic changes, which the Earth is experiencing, is due to emissions of gases that enhance the greenhouse effect in the atmosphere. At the same way it is known as the main contribute to this increased greenhouse effect is due to carbon dioxide. Therefore, the importance to plan and evaluate climate mitigation strategies limiting the CO_2 emissions requires accurate estimates of carbon exchange between the land surface and the atmosphere.

Following a "bottom-up" approach, in this work a modelling framework that accurately represents surface-atmosphere carbon exchanges at high-resolution has been developed. Model simulations were preformed over a large enough area and for a long enough time interval to validate a methodology applicable to estimate annual CO_2 emissions in regions that extend for thousands of Km.

To validate the method, the entire island of Sardinia, located in the center of the Mediterranean Sea, was chosen as the focus of this research. Simulations were conducted for the first 30 days of May 2010 to generate 3 Km resolution carbon exchange maps. The area was selected mainly for two reasons: the first is the wide range of different ecosystems, which allow for testing the model on very different meteorological conditions and landscape types. The second reason lies in its typical climate, which allow for filling a lack of knowledge about carbon flux estimates at regional scale in Mediterranean climate ecosystems. The SVAT model ACASA, one of the most elaborated multilayer higher-order-closure model of the last generation, was embedded within the mesoscale

meteorological forecast model WRF. Model simulations were compared with Eddy Covariance observations for a single point located in the south of the island. Two statistical analysis were performed: the first considering all the data of the time series, while the second analysis dealing with the simulated half-hour data sorted by time and averaged. With respect to the first analysis, results were evaluated through a linear regression of model versus observed data with a slope of 0.89 and R^2 = 0.91, and a correlation coefficient of 0.96. So, the model was able to explain more than 90% of the total observed variation in carbon dioxide with a P-value<0.0001. Considering the aggregated data analysis, it can be observed a little improvement in the above three parameters: the slope of the linear regression of the model versus observed data is 0.90, R^2=0.94, and the correlation coefficient 0.97 with a P-value<0.0001. The model seems to show a small underestimate of the carbon emission related to the nocturnal respiration while it performs very well in retrieving the diurnal carbon uptake where almost all the observations lies within the error interval of the simulated values. From a global point of view, the simulation results in a slightly overestimation of the carbon uptake, but values of the above parameters demonstrate that the model is surprisingly efficient in reproducing the carbon flux. It is shown that it can well explain more than 90% of the observations.

The analysis of the map referring to the carbon exchange amount for the first 30 days of May 2010, shows as the entire island of Sardinia behaved as a carbon sink, capturing a total amount of 4.19 GtC. Analyzing the local distribution of carbon exchange over the island it emerges as source areas coincide with the urban areas, while the remaining part of the territory behaved as carbon sink. The carbon flux per unit area referring to the considered period spans between $-4.2 \cdot 10^2 gCm^{-2}$ of a "grassland" land use zone in the north-east of the island to $1.2 \cdot 10^3 gCm^{-2}$ found in the Cagliari downtown, the main city of the island.

It is possible to recognize four carbon uptake bands relative to the four land use categories which

together cover 80% of the considered territory. The "*Shrubland"* 30-day carbon flux per unit area ranges from $-1.4 \cdot 10^2$ gCm^{-2} to $-8 \cdot 10$ gCm^{-2}. This is the land use category involving the Mediterranean maquis. "*Cropland/Woodland Mosaic"* and "*Grassland"* categories show a carbon exchange range between $-2.1 \cdot 10^2$ gCm^{-2} and $-1.5 \cdot 10^2$ gCm^{-2}, "*Dryland Cropland and Pasture*" and "*Irrigated Cropland and Pasture*", have a monthly carbon uptake rate that spans between $-2.9 \cdot 10^2$ gCm^{-2} and $-2.2 \cdot 10^2$ gCm^{-2} while for "*Evergreen Broadleaf Forest" the* 30-day uptake interval lies between $-2.9 \cdot 10^2$ gCm^{-2} and $-3.3 \cdot 10^2$ gCm^{-2}. This latter category includes the typical Mediterranean forest mainly composed by *Quercus ilex,* which represents the land use type with the highest carbon uptake of the study area.

A further reliability check was performed considering other studies, available in literature, involving the three most diffused vegetation categories covering about 60% of the island: *Evergreen Broadleaf Forest*, *Shrubland Mediterranean maquis* and *Dryland Cropland and Pastures*. It was performed a comparison between the results and

- data coming from studies carried out in sites located outside the island
- studies considering different temporal interval.

Through these comparisons it was possible to verify a complete consistency of simulated data with the reconstructed fluxes. Even if it cannot be considered as a direct validation, it contributes, together with the single point EC analysis, evaluate the robustness of the general structure of the coupled model WRF-ACASA. The methodology tested in this work proved as WRF-ACASA model represents a flexible instrument to provide a cogent simulation of carbon exchange at regional scale. The application of this method to a Mediterranean climate region, results in one of the first studies dealing with carbon exchange at regional scale for territories characterized by this unique climate variety. Therefore it should be emphasized the important contribute of this work to the knowledge of these ecosystem types.

REFERENCES

Allard V., Ourcival J. M., Rambal S., Joffre R., Rocheteau A., 2008. *Seasonal and annual variation of carbon exchange in an evergreen Mediterranean forest in southern France.* Global Change Biology vol 14 issue 4 p. 714-725

Aubinet M., Grelle A., Ibrom A., Rannik U., Moncrieff J., Foken T., Kowalski A.S., Martin P.H., Berbigier P., Bernhofer Ch., Clement R., Elbers J., Granier A., Grunwald T., Morgenstern K., Pilegaard K., Rebmann C., Snijders W., Valentini R., Vesala T., 2000. *Estimates of the annual net carbon and water exchange of European forests: the EUROFLUX methodology*. Adv. Ecol. Res. 30: 113-174

Baldocchi D., Vogel C.A., Hall B., 1997. *Seasonal variations of carbon dioxide exchanges rates above and below a boreal jack pine forest*. Agric. For. Meteor. 83: 147-170.

Barry R.G., Charney R.J., 1983. *Atmosphere, Weather and Climate.* Routledge.

Benzi R., Deidda R., Marrocu M., 1997. *Characterization of temperature and precipitation fields over Sardinia with principal components analysis and singular spectrum analysis*. International journal of climatology, vol. 1231-1262

Blankenship R., 2002. *Molecular Mechanisms of Photosynthesis*. Wiley & Sons

Camarda I. 1993. Montagne di Sardegna. Carlo Delfino editore

Chen F., Dudha J., 2001. *Coupling an Advanced Land Surface–Hydrology Model with the Penn State–NCAR MM5 Modeling System.* Monthly Weather review, American Meteorological Society, April, Vol. 569

Chen F., 2011. *Land Surface Processes and their Modeling in WRF.* Lecture at the 12th WRF Users'x Workshop, Boulder, June20

Chena J.M., Pavlica G., Brown L., Cihlara J., Leblanca S.G., Whitea P., Hallb R.J., Peddlec D.R., Kingd D.J., Trofymowe J.A., Swiftf E., Van der Sandeng J., Pellikkah K.E., 2002. Derivation and validation of Canada-wide coarse-resolution leaf area index maps using high-resolution satellite

imagery and ground measurements. Remote Sensing of Environment Volume 80, Issue 1, Pages 165–184

Ciais P., Wattenbach M., Vuichard N., Smiths P., Diao S.L.,. Don A., Luysaert S., Jansens I.A., Bondeau A., Dechow R., Leip A., Smith P.C., Beer C., Van Der Werf G.R., Gervois.s., Van Hoost K., Tomelleri E.,Freibauer A., Shulze E.D., Carboeurope Syntesis Team, 2010. *The European carbon balance. Part 2: croplands.* Global Change Biology vol 16. pag 1409-1428

Collatz G.J, Ribas-Carbo M, Berry JA 1992. *A coupled photosynthesis - stomatal conductance model for leaves of C4 plants*. Australian Journal of Plant Physiology, **19**, 519-538.

Collatz G.J., Ball, J.T., Grivet C., Berry J.A.,1991. *Physiological and environmental regulation of stomatal conductance, photosynthesis and transpiration: a model that includes a laminar boundary laye*r. Agr. Forest Meteorol., 54, 107–136.

Cox P.M., Huntingford C., Harding R.J., 1998. *A canopy conductance and photosynthesis model for use in a GCM land surface scheme*. Journal of Hydrology, 212-213, 79-94.

Critchfiel, H.J., 1983.*General Climatology.* Prentice-Hall.

Dirac P.A.M., 1932. *Principles of quantum mechanics*, 1981 Oxford University Press.

Draxl C., Hahmann A., Peña A., Nissen J., Giebel G., 2010. *Validation of boundary-layer winds from WRF mesoscale forecasts with applications to wind energy forecasting*. 19th Symposium on Boundary Layers and Turbulence, Paper 1B.1

El Mahgarya Y., Ibrahimb A., Shamab M., Hassanb A., Rifaic M., Selimd M., Gelild A., Korkord H., Higazie A., Amin A., BedewiF., Forsström J., 1994. *Costs of CO2 abatement in Egypt using both bottom-up and top-down approaches.* Energy Policy Vol 22

Falge E., Retha S., Brüggemannb N., Butterbach-Bahlb K., Goldbergc V., Oltchevd A., Schaafe S., Spindlerf G., Stillerg B., Queckc R., Köstnerc B., Bernhoferc C., 2005. *Comparison of surface energy exchange models with eddy flux data in forest and grassland ecosystems of Germany*. Ecological Modelling Vol 188 issue 2-4

Falk M., Pyles R.D., Marras S., Spano D., Snyder R.L., Paw U K.T. 2010. *Coupling of the WRF and ACASA models for urban environments: two case studies*. AMS Conference on Ninth Symposium on the Urban Environment, Keystone, Colorado, USA, August 2-6, 2010.

Farquhar G.D, von Caemmerer S., Berry J.A., 1980. *A biochemical model of photosynthetic CO_2 assimilation in leaves of C3 species*. Planta, 149, 78-90.

Farquhar G.D., von Caemmerer S., 1982. *Modelling of photosynthetic response to environmental conditions, in: Physiological Plant Ecology II, Water Relations and Carbon Assimilation.* Lange, O. L., Nobel, P. S., Osmond, C. B., and Ziegler, H., Encyclopedia of Plant Physiology, 12 B, Springer, Berlin, 549–588.

Garbulskym M., Penuelas J., Papale D., Filella I., 2008. *Remote estimation of carbon dioxide*

uptake by a Mediterranean forest. Global Change Biology Vol 14, 2860–2867

Gasiorowicz S.,2003. *Quantum Physics.* University of Minnesota, Wiley & sons
Gerbig G., Lin G.C., Wofsy S.C., Daube B.C., Andrews A.E., Stephens B.B, Bakwin P.S., Grainger C.A., 2003. *Toward constraining regional-scale fluxes of CO_2 with atmospheric observations over a continent: 2. Analysis of COBRA data using a receptor-oriented framework.* Journal of geophysical research vol. 108, NO. D24, 4757

Gioli B., Miglietta F., 2007. *Stima del bilancio del carbonio a scala regionale*. Forest@ 4 (4): 469-477. [online] URL: http://www.sisef.it/forest@/

Giovannini L., Zardi D., de Franceschi M., 2011. *Analysis of the Urban Thermal Fingerprint of the City of Trento in the Alps.* J. Appl. Meteor. Climatol., 50, 1145–1162

Göckede M., Michalak A.M., Vickers D., Turner D.P., Law B.E., 2010. *Atmospheric inverse modeling to constrain regional-scale CO_2 budgets at high spatial and temporal resolution*. Journal of geophysical research vol. 1125, 50, 1145-1162

Goldberg V., Bernhofer C., 2001. *Quantifying the coupling degree between land surface and the atmospheric boundary layer with the coupled vegetation-atmosphere model HIRVAC*. Annales Geophysicae Vol. 19, 5 581-587

Goldstein H., Poole C., Safko J.L., 2002. *Classical Mechanics*. 3rd ed., Addison-Wesley

Gourdji S.M., Hirsch A.I., Mueller K.L., Yadav V., Andrews A.E., Michalak A.M., 2010. *Regional-scale geostatistical inverse modeling of North American CO2 fluxes: a synthetic data study*. Atmos. Chem. Phys.10, 6151-6167,

Hall W.D., Rasmussen R.M., Thompson G., 2005. *The new Tomson microphysical scheme in WRF*. WRF/MM5 Users' Workshop - June 2005

Holton J.R. 1992. *An introduction of dynamic meteorology*. Academic Press

Holloway S., Vincent C., Bentham M., Kirk K., 2006. *Top-down and bottom-up estimates of CO_2 storage capacity in the United Kingdom sector of the southern North Sea basin.* Environmental Geosciences v. 13

Hsu Y.K., Van Curen V., Park S., Jakober C., Herner J., FitzGibbon M., Blake D.R. Parrish D.D., 2010. *Methane emissions inventory verification in southern California.* Atmospheric Environment, Vol. 44

Jarvis P., 1976. *The interpretation of the variations in leaf water potential and stomatal conductance found in canopies in the field*. Philosophical Transactions of the Royal Society of London Series B, **273**, 593-610.

Kuhnert M., Köstner B. 2009. *Regional modelling of water and CO2-fluxes with a one-dimensional SVAT model.* EGU General Assembly 2009, held 19-24 April, 2009 in Vienna, Austria. http://meetings.copernicus.org/egu2009, p.11113

Kiese R., Li C., Hilbert D., Hans Papen H., Butterbach-Bahl K. 2005. *Regional application of PnET-N-DNDC for estimating the N2O source strength of tropical rainforests in the Wet Tropics of Australia*. Global Change Biology Vol 11 issue 1

Kuyper M.M.M., Pancost R.D., Damste J.S.S., 1999. *A large and abrupt fall in atmospheric CO2 concentration during Cretaceous times*. Nature, Vol. 399: 342-345

Lamarque J., Mahowald N., Niu G.-Y., Qian T., Randerson J., Running S., Sakaguchi K., Slater A., Stockli R., Wang A., YangZ.-L., ZengXi., Zeng Xu., 2010. *Technical Description of version 4.0 of the Community Land Model (CLM). NCAR Technical Note NCAR/TN-478+STR.* National Center for Atmospheric Research, Boulder, CO, 257 pp.

Lawrence D., Oleson K., Flanner M.G., Thornton P.E., Swenson S.C., Peter J., Lawrence P., Zeng X., Yang Z.L., Levis S., Sakaguchi K., Bonan G.B., Andrew G., Slater A.G.. 2011. *Parameterization Improvements and Functional and Structural Advances in Version 4 of the Community Land Model*. J. Adv. Model. Earth Syst., Vol. 3, Art. M03001, 27 pp.

Lax P.D., Richtmyer R. D.,1956. *Survey of the stability of linear finite difference equations*. Comm. Pure Appl. Math. 9, 267-293

Leveque, 1992. *Numerical Methods for Conservation Laws.* Birkh üser.

Leuning, R.1990. *Modelling stomatal behaviour and photosynthesis of Eucalyptus grandis.* Aust. J. Plant Physiol., 17, 159–175,

Livneh B., Xia,Y., Mitchell K., Ek M., Lettenmaier D., 2010. *Noah LSM Snow Model Diagnostics and Enhancements.* American meteorological society, Journal on line, Hydrometeor, 11, 721–738. doi:http://dx.doi.org/10.1175/2009JHM1174.1

Landsberg H., 1988. *World survey of climatology.* Elsevier.

Ma S., Baldocchi D.D., Xu L., Hehn T., 2007. *Inter-annual variability in carbon dioxide exchange of an oak/grass savanna and open grassland in California*. Agricultural and Forest Meteorology 147 157–171

Manning K., Chen F., 2005. *Continued application and development of a High-Resolution Land Data Assimilation System*. WRF/MM5 Users Workshop-June 2005

Marras. S., Spano D., Sirca C., Duce P., Snyder R.L., Pyles R.D, Paw U K.T., 2008. *Advanced-Canopy-Atmosphere-Soil Algorithm (ACASA Model) for estimating mass and energy fluxes*. Italian Journal of Agronomy, Vol. 3, supplement No. 3, 2008. Forum editor.

Marras. S., Spano D., Sirca C., Duce P., Snyder R.L., Pyles R.D, Paw U K.T., 2009a. *Valutazione*

delle performances del modello ACASA *su canopy non compatte*. Italian Journal of Agrometeorology, anno 14 n. 2 giugno 2009.

Marras. S., Spano D., Pyles R.D., Falk M., Sirca C., Maglietta F., Snyder R.L., Paw U K.T., 2009b. "*Energy and mass flux simulations in urban area using the ACASA model". Eos Trans. AGU, 90(52)*, Fall Meet. San Francisco, California (USA), 14-18 December 2009, Suppl., Abstract B33D-0421.

Marras. S., Pyles R.D., Sirca C., Paw U K.T., Snyder R.L., Spano D., Duce P., 2011. "*Evaluation of the Advanced Canopy-Atmosphere-Soil Algorithm (ACASA) model performance over Mediterranean maquis ecosystem".* Agricultural and Forest Meteorology, vol. 151; p. 730-745, ISSN: 0168-1923

Martyn D., 1992. *Climates of the world.* Elsevier.

Meyers T.P. and Paw U K.T., 1986. *Testing of a higher-order closure model for airflow within and above plant canopies.* Bound.-Lay. Meteorol., 37, 297–31

Meyers T.P. and Paw U K.T., 1987. *Modelling the plant canopy micrometeorology with higher-order closure techniques.* Agr. Forest Meteorol., 41, 143–163

Miranda E.E., Di Bella C.M., Ordoyne, C., Kopin, Y., Roy P.S., 2006. *Validation of the global land cover 2000 map*. IEEE Geoscience and Remote Sensing Society, Volume:44, Issue: 7

Mitchell A., Griffiths S., 1980.*The Finite Difference Method in Partial Differential Equations*. Wyley and sons

Mitchell B., Moser L.E., Moore D.D., Redfearn K.J. 1998. *Tiller Demographics and Leaf Area Index of Four Perennial Pasture Grasses*. Agronomy-Faculty Publications. Paper 69. http://digitalcommons.unl.edu/agronomyfacpub/69

Monteith J.L., 1981. *Evaporation and Surface-Temperature.* Quarterly Journal of the Royal Meteorological Society, 107 (451), 1-27

Olchev A., Ibromc A., Rossa T., Falka U., d, Rakkibua G., Radlera K., Grotea S., Kreileina H., Gravenhorsta G., 2008. *A modelling approach for simulation of water and carbon dioxide exchange between multi-species tropical rain forest and the atmosphere.* Ecological Modelling Vol 212 1-2

Oltchev A., Constantin J., Gravenhorst G., IbromA., Heimann J., Schmidt J., Falk M., Morgenstern K., Richter I., Vygodskaya V., 1996. *Application of a six-layer SVAT model for simulation of evapotranspiration and water uptake in a spruce forest*. Physics and Chemistry of the Earth, Volume 21, Issue 3, Pages 195–199

Otkin J., Grenwald T. 2008. "*Comparison of WRF Model-Simulated and MODIS-Derived Cloud Data. Monthly Weather review*", American Meteorological Society, June, Vol. 136

Papale D., Reichstein M., Canfora E., Aubinet M., Bernhofer C., Longdoz B., Kutsch W., Rambal S., Valentini R., Vesala T., And Yakir D., 2006. *Toward a more harmonized processing of eddy*

covariance CO_2 fluxes: algorithms and uncertainty estimation. Biogeosciences Discussions. 3: 961, 992.

Pasini A., Triacca U. Attanasio A. 2012*"Evidence of recent causal decoupling between solar radiation and global temperature",* Environmental Research Letter, Vol.7, 034020

Paw U K.T., Gao W., 1988. *Applications of solutions to non-linear energy budget equations*, Agr. Forest Meteorol., 43, 121–145,

Peixoto, J.P., Oort A.H., 1992. *Physics of climate.* American Institute of Physics.

Pyles R.D., 2000a. *The development and testing of the UCD Advanced Canopy- Atmosphere-Soil Algorithm (ACASA) for use in climate prediction and field studies*. PhD dissertation, Davis, University of California, pp. 190.

Pyle R.D., Weare B.C., Paw U K.T., 2000b. *The UCD Advanced Canopy-Atmosphere-Soil Algorithm: Comparison with observations from different climate and vegetation regimes*. *Q.J.R. Meteorol. Soc.* 126, 2951-2980.

Pyles R.D., Weare B.C., Paw U K.T., Gustafson, W., 2003. *Coupling between the University of California, Davis, Advanced Canopy-Atmosphere-Soil Algorithm (ACASA) and MM5: Preliminary Results for July 1998 for Western –North America*. J Appl. Meteorol. 42, 557-569.

Rambal S., Joffre R.M., Ourcival J.,J. Cavender-Bares J., Rocheteau A., 2004. *The growth respiration component in eddy CO2 flux from a Quercus ilex Mediterranean forest.* Global Change Biology Vol 10,Issue 9, pag1460–1469,

Sala A., Sabat S., Gracia C., Tenhunen J.D., 1994. *Canopy structure within a Quercus ilex forested watershed: variations due to location, phenological development, and water availability*. Structure and function trees, 8:254-261

Sarrat C., Noilhan J., Dolman A.J., Gerbig C., Ahmadov R., Tolk L.F., Meesters A.G.C.A., Hutjes R.W.A, Ter Maat H.W., Perez-Landa G., Donier S., 2007. *Atmospheric CO2 modeling at the regional scale: an intercomparisono of 5 meso-scale atmospheric models*. Biogeosciences, 4, 1115–1126.

Sarrat C., Noilhan J., Lacarrere P., Masson V., Ceschia E., Ciais P., Dolman A., Elbers J., Gerbig C., Jarosz N., 2009. *CO2 budgeting at the regional scale using a Lagrangian and experimental strategy and meso-scale modeling*. Biogeosciences, 6, 113–127, 2009

Skamarock, W. C., Klemp J. B., 2008. *A time-split nonhydrostatic atmospheric model for weather research and forecasting applications*. J. Comput. Phys., 227 (7), 3465–3485.

Schmid H.P., Grimmond C.S.B., Cropley F., Offerle B., Hong-Bing Su., 2000. *Measurements of CO_2 and energy fluxes over a mixed hardwood forest in the mid-western United States*. Agric. For.

Meteor. 103: 357-374.

Singhal G.S., Renger G., Sopory S.K., Irrgang K-D., Govindjee S., 1999. *Concepts in Photobiology: Photosynthesis and Photomorphogenesis*. Narosa Publishers/New Delhi and Kluwer Academic/Dordrech

Smirnova T.G., Brown, J.M., and Benjamin, S.G.,1997. *Performance of Different Soil Model Configurations in Simulating Ground Surface Temperature and Surface Fluxes.* Mon. Weather Rev., 125, 1870–1884.

Smirnova T.G., Brown J.M., Benjamin S.G., Kim D., 2000. *Parameterization of cold-season processes in the MAPS land- surface scheme*. J. Geophys. Res.-Atmos., 105, 4077–4086,

Staudt K., Falge E., Pyles R.D., Paw U K.T., Foken T., 2010. *Sensitivity and predictive uncertainty of the ACASA model at a spruce forest site*. Biogeosciences, 7, 3685–3705, 2010

Staudt M., Joffre R., Rambal S., Kesselmeir J., 2001. *Effect of elevated CO2 on monoterpene emission of young Quercus ilex trees and its relation to structural and ecophysiological parameters*. Tree Physiology 21, 437–445

Stewart J.B., 1988. *Modelling surface conductance of pine forest*. Agricultural and Forest Meteorology,43, 19-35.

Strikwerda J.C. 1989. *Finite Difference Schemes and Partial Differential Equations*. Chapman & Hall

Su H. B., Paw U K. T., and Shaw R. H., 1996. *Development of a coupled leaf and canopy model for the simulation of plant-atmosphere interactions.* J. Appl. Meteorol., 35, 733–48,

Tibaldi S., Buzzi A., Speranza A., 1990. *Orographic Cyclogenesis in Extratropical Cyclones.* AMS, 107-127.

Valentini R., Matteucci G., Dolman A. J., Schulze E.D., Rebmann C., Moors E. J., Granier A., Gross P., Jensen N. O., Pilegaard K., Lindroth A., Grelle A.A, Bernhofer C., Grunwald T., Aubinet M., Ceulemans R., Kowalski A. S., Vesala T., Rannik U., Berbigier P., Loustau D., Gu[eth]mundsson J., Thorgeirsson H., Ibrom A., Morgenstern K., Clement R., Moncrieff J., Montagnani L., Minerbi S., Jarvis P.G., 2000. *Respiration as the main determinant of carbon balance in European forests*. Nature 404,861-865

Vay S.A., Woo J.H., Anderson B.E., Thornhill K.L., Blake D.R., Westberg D.J., Kiley C.M., Avery M.A., Sachse G.W., Streets D.G., Tsutsumi Y., Nolf S.R., 2003. *Influence of regional-scale anthropogenic emissions on CO2 distributions over the western North Pacific*. Journal of geophysical research VOL. 108, 8801, 14 PP.

Vaz M., Maroco J., Ribeiro N., Gazarini L.C., Pereira J.S., Chaves M.M. 2011. *Leaf-level responses to light in two co-occurring Quercus (Quercus ilex and Quercus suber): leaf structure, chemical composition and photosynthesis*. Agroforest Syst 82:173–181

Wallace J., Hobbs P.,1977. *Atmospheric science, an introductory survey*. Academic Press, San Diego, California

Wallace J., Hobbs P.,2005. *Atmospheric science, an introductory survey*. *Second edition.* Academic Press, San Diego, California,

Woodwell G.M., Whittaker R.H., 1968. *Primary production in terrestrial ecosystems*. Am. Zoologist. 8:19–30.

Wuebbles D.J., 1982. *Chlorocarbon emission scenarios: Potential impact on stratospheric ozone*. Journal of geophysical research, VOL. 88, NO. C2, P. 1433, 1983

Xiu A. Pleim J. 2000. *Development of a Land Surface Model. Part I: Application in a Mesoscale Meteorological Model*. Journal of applied meteorology volume 40

Zhao Q., Liu Z., Ye B., Qin Y., Wei Z., Fang S., 2009. *A snowmelt runoff forecasting model coupling WRF and DHSVM*. Hydrology and Earth System Sciences, 13, 1897–1906,

Zhaoa Y., Nielsen C.P., McElroy M.B., 2012. *China's CO2 emissions estimated from the bottom up: Recent trends, spatial distributions, and quantification of uncertainties*. Atmospheric environment, Vol. 59

Zulueta R.C., Oechel W.C., Loescher H.W., Lawrence W.T., Paw U K.T. 2011. *Aircraft-derived regional scale CO2 fluxes from vegetated drained thaw-lake basins and interstitial tundra on the Arctic Coastal Plain of Alaska*. Global Change Biology vol. 17.